**UNIVERSITÀ DEGLI STUDI DI PADOVA**

**DIPARTIMENTO DI SCIENZE CHIMICHE**

**CORSO DI LAUREA MAGISTRALE IN CHIMICA**

**TESI DI LAUREA MAGISTRALE**

# Design and development of lanthanoid-based luminescent solar concentrators

**Relatore: Prof.ssa Lidia Armelao**

**Controrelatore: Prof. Enzo Menna**

**LAUREANDA: Irene Motta**

**ANNO ACCADEMICO 2021/2022**

*A nonno Giorgio*

# Index

# Chapter 1

# Introduction

## 1.1. Luminescent solar concentrators

In a context of increasing environmental concern towards climate change and fossil fuels consumption, researching efficient ways to produce renewable energy is playing a major role in the transition towards a sustainable future. Solar irradiation offers great potential as a green source of energy, theoretically being able to fulfil global energetic needs 10 000 times over[1]. In the last 50 years, the photovoltaic (PV) conversion of solar energy has undergone impressive development with the introduction of semiconductor-based solar modules, among which silicon-based ones are the most widespread on the market[2]. While classic photovoltaics still experience intense research aimed to further improving their conversion efficiency, a parallel increase in scientific interest is directed towards the development of alternative PV technologies, as means to reduce the cost and the environmental impact of the produced PV energy. Among the pursued goals, the implementation of "building-integrated photovoltaics" (BIPV) in the urban environment is of particular appeal, as it would turn architectural elements into active generators of electrical power capillary distributed inside the cities, by integrating innovative photovoltaic systems within their very structure[3–5]. The retrieval of extended urban surfaces, as building façades, for solar power conversion would result particularly advantageous in heavily urbanized areas, where the installation of classic photovoltaic modules is limited mainly to rooftops by the need for direct irradiation and aesthetic factors. Such spaces, especially in the case of tall buildings, are often insufficient to accommodate enough PV units to meet the facility's electrical energy requirements. In this prospect, devices known as luminescent solar concentrators (LSCs) could provide with a versatile auxiliary PV

technology, being deployable as semi or fully transparent glazing systems, elements which often take up significant footage in modern buildings.

In its most conventional form, a luminescent solar concentrator consists of a planar slate of glassy or polymeric material, embedded with luminescent species[6] (Fig. 1.1). When sunlight passes through the concentrator's exposed surface, the luminophore is capable to absorb part of the incident radiation and re-emit it at longer wavelengths. The host medium acts then as a waveguide for the emitted photons, which are redirected towards the concentrator's edges through total internal reflection (TIR), where appositely coupled PV cells collect the incoming radiation and convert it into electrical current.

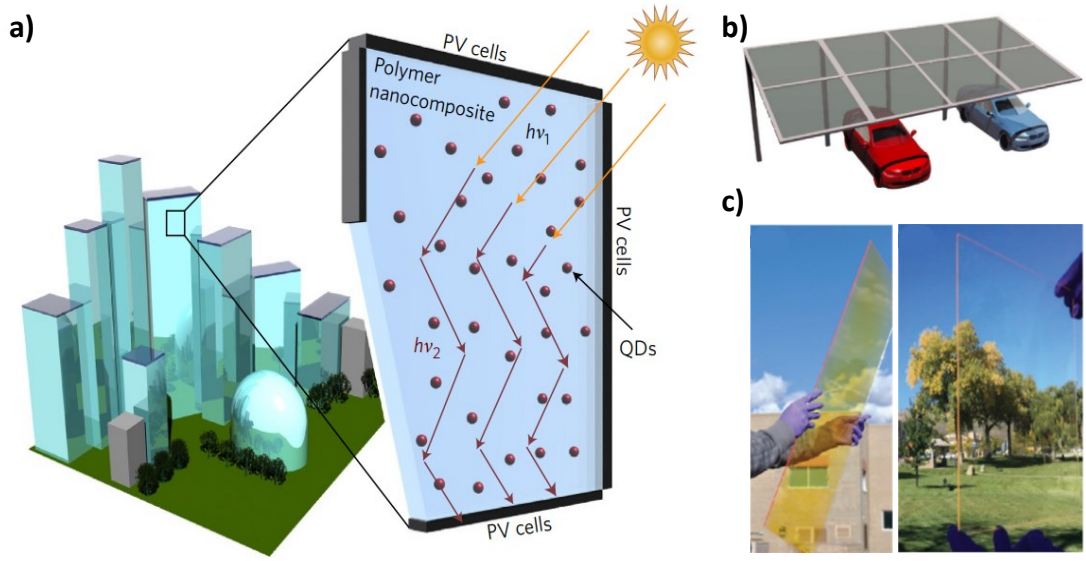


***Figure 1.1*** *a) schematic representation of the working mechanism of an LSC device containing quantum dots (QDs) as luminescent species with potential application as transparent energy-producing windows[7], b) example of an alternative BIPV urban element[5], c) example of large-area LSC containing a visible-emitting luminophore[5].*

Such a design offers a series of advantages with respect to existing PV modules, first and foremost the concentration of light on highly efficient small-sized cells, eliminating the need for external concentration devices and reducing the amount of employed PV material[8,9]. Secondly, LSCs possess a wider acceptance angle for incident radiation, making them able to work even in diffuse light conditions, as can occur with clouded weather. Since the waveguide's perimeter continuously receives indirect illumination, shadowing of the device determines much slighter efficiency losses than in the case of classic bulk photovoltaics, and most importantly it does not hinder the LSC functioning[3]. In addition, considered edge-coupling the waveguide with silicon PV cells, an accurate tailoring of the luminophore absorption and emission

wavelengths can make up for the mismatch between the solar spectrum and Si band gap, allowing to downshift the harvested radiation to a spectral region where the cells are most efficient[9].

First proposed by Lerner et al. in 1973[10] and theorized by Goetzberger and Greubel in 1977[11], the LSC technology has been recently rediscovered due to the renewed interest in green energy sources, and many advances have been made in the field over the last two decades, aimed to improve the LSC devices efficiency, other than their versatility in terms of shape, colour, transparency and flexibility[12]. The current LSC literature presents a multitude of different declinations of the subject, with a wide variety of tested luminophores, host materials and geometries. Some examples of LSC-based architectures have already been realized (Fig. 1.2), aimed to verify the scalability of the devices in view of their possible application as BIPV[13,14].

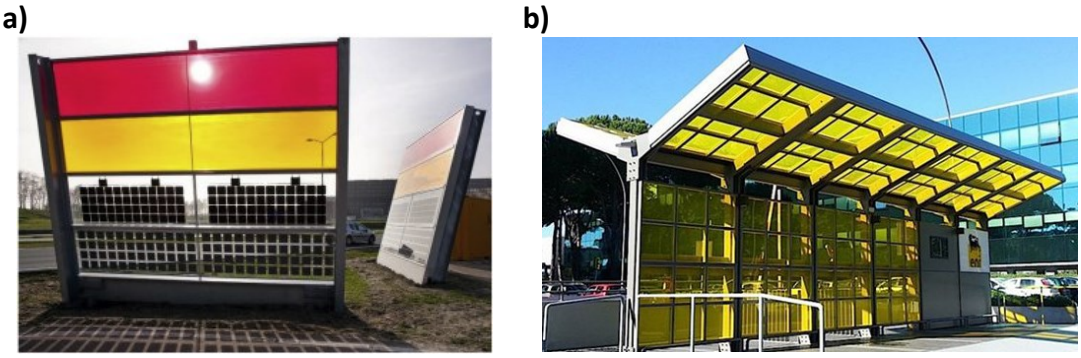


***Figure 1.2*** *a) prototype of a noise-barrier implemented with 1 × 5 m² coloured LSCs, tested at two different angulations with respect to solar light incidence[13], b) LSC-powered electric bicycle charging station realized by ENI in 2018[14].*

Integration into the urban environment as PV building envelopes is not the only practical usage achievable by the LSC technology[15]. Among other potential fields of application, LSC can be employed in horticulture as wavelength-converting greenhouses roofing, or as enhancers for algae growth. Microreactors driven by LSCs have also been devised as efficient tools to catalyse photochemical reactions using sunlight as energy source. The ample range of available materials for the fabrication of the waveguides paves the way for innovative designs, such as self-powered flexible electronic devices, liquid-based LSCs, luminescent fibres for higher light concentration, or smart windows realized with liquid crystal hosts capable of switching between transparent and opaque states. Position sensors, imaging systems and detectors for optical communications all based on LSCs have also been proposed.

Considered the variability in the device shapes and materials, it is important to qualify the features and performance of an LSC in an unequivocal way. According to recent reviews[6,8,9], the characterization of a luminescent solar concentrator must be inclusive of the fundamental parameters listed below. The first and most evident feature of an LSC is its geometric gain (G), defined as the ratio of the exposed area collecting the incident light ($A_{in}$) to the total area of the edges emitting the concentrated radiation ($A_{out}$)[8].

$$G = \frac{A_{in}}{A_{out}} \tag{1.1}$$

The geometric gain determines the theoretical limit of the concentration factor (C), which is defined as the ratio of the flux of emitted photons ($N_{out}$) to the flux of incident photons ($N_{in}$). The concentration factor can be then expressed in function of G by introducing the optical efficiency of the waveguide ($\eta_{opt}$) as a proportionality factor[8].

$$C = \frac{N_{out}}{N_{in}} = \eta_{opt} \cdot G \tag{1.2}$$

The optical efficiency quantifies the performance of an LSC in terms of purely photophysical and optical processes involving the waveguide, which account for absorption, downshift, transport and concentration of light. Since $\eta_{opt}$ is a measure of the non-ideality of the system, it can be described as the product of several partial efficiencies, related to all processes liable to radiation losses[9].

$$\eta_{opt} = (1 - R)\eta_{abs}\eta_{SA}\eta_{yield}\eta_{Stokes}\eta_{trap}\eta_{tr} \tag{1.3}$$

In the first term, R is the Fresnel reflection coefficient for normal incidence, and accounts for the fraction of the incident solar light reflected by the waveguide surface and therefore lost without effectively entering the LSC. The coefficient depends on the refractive index of the host material (n) as $R = (1 - n)^2 / (1 + n)^2$, so higher refractive indexes determine higher fractions of reflected light. While only normal incidence is considered here for simplicity, in real working conditions reflection for all incidence angles should be considered[8].

$\eta_{abs}$ is the absorption efficiency of the luminescent layer, indicating the fraction of absorbed photons with respect to the total number of photons incident on the LSC exposed surface; $\eta_{abs}$ therefore depends on the absorbance (A) of the luminophore.

$\eta_{SA}$ is the self-absorption efficiency, indicating the emitted radiation lost due to its re-absorption from other molecules of the same luminophore. Depending on the spectral overlap between the absorption and emission bands of the luminophore, $\eta_{SA}$ reaches the unit value when said overlap is null, as for example for $Ln^{3+}$ emitting centres.

$\eta_{yield}$ corresponds to the photoluminescence quantum yield (PLQY) of the emitter.

$\eta_{Stokes}$ accounts for the energy thermally dissipated during the luminescence process and is calculated as the ratio of the energy of the emitted photons, taken at the wavelength at which falls the emission band maximum ($\lambda_p$), to the energy of the incident photons. In terms of wavelengths, $\eta_{Stokes} = \lambda_p / \lambda_i$.

The last two terms in Eq. 1.3 quantify the waveguiding properties of the host medium with respect to the emitted radiation. The major loss factor for most LSC devices (40 - 55% of all absorbed energy)[12] is caused by the fraction of emitted light that exits the waveguide from the upper and lower surfaces through an "escape cone", also "exit cone" (Fig. 1.3), rather than from the edges. Photons emitted inside the aperture angle of the escape cone, the value of which depends on the refractive index of the material, will be lost by the waveguide and will not reach the PV cells on the sides. The trapping efficiency of the host is quantified as $\eta_{trap} = (1 - 1/n^2)^{1/2}$, which translates to a value of 74% for a material with n = 1.5, a figure representative of the refractive index for many polymeric matrices. As can be deduced, higher refractive indexes are favourable to reduce escape cone losses.

Lastly, $\eta_{tr}$ indicates the transport efficiency of the waveguide and is estimated taking into consideration the losses caused by matrix absorption and scattering effects arising from imperfections in the matrix, both superficial and in the bulk.

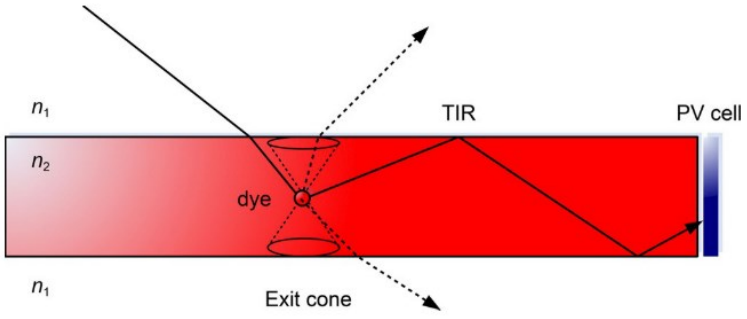


***Figure 1.3*** *Depiction of the working principle of an LSC, evidencing the possibility of exit cone losses of the photons emitted by the luminophore*[16].

Although impractical for the calculation of $\eta_{opt}$, estimating the above listed contributes for a given luminophore or host material can be useful to evaluate their eligibility for the LSC application. It should be also noted that the optical efficiency is dependent on

the excitation wavelength[9], as n, A and PLQY are all functions of $\lambda_i$, so an accurate calculation of $\eta_{opt}$ is made by integrating the several contributes of Eq. 1.3 over the whole solar spectrum. Experimentally, the optical efficiency can be derived through simpler means by functional characterization of the device. The ratio of the short-circuit current of the PV cells edge-coupled to the illuminated LSC slab ($I_{LSC}$) to that of the same cells under direct illumination from the same source with perpendicular incidence ($I_{SC}$), normalized for the geometrical gain, yields the optical efficiency of the waveguide[6].

$$\eta_{opt} = \frac{I_{LSC}}{I_{SC} \cdot G} \tag{1.4}$$

Accordingly to the standard parameters defined for photovoltaic devices[17], a power conversion efficiency (PCE) can be derived also for an LSC, expressed as the ratio of the electrical power generated by the collecting PV cells ($P_{out}$) to the incident power from the light source ($P_{in}$). Experimentally, the output power can be calculated as the product between the short-circuit current density ($J_{LSC}$), the open-circuit voltage ($V_{OC}$) and the fill factor (FF)[6].

$$PCE = \frac{P_{out}}{P_{in}} = \frac{J_{LSC} \cdot V_{OC} \cdot FF}{P_{in}} \tag{1.5}$$

The working principle and the mentioned electrical parameters for a photovoltaic cell are defined in Appendix A.

## 1.2. Luminophores

The emitting centres of a luminescent solar concentrator are its key components, enabling its operation and playing a crucial role in the optical efficiency of the waveguide. An ideal luminophore should possess all the following characteristics[12]: a broad spectral absorption, with high molar absorptivity over the whole absorption spectrum, low or no overlap between the absorption and emission bands (large Stokes shift) so to avoid reabsorption losses, high PLQY, good solubility in the host medium, prolonged photostability and emission wavelengths tuned to the maximum responsivity of the employed PV material. In order to meet such requirements, a great variety of emitters has been extensively studied, that can be categorized in three main classes: organic dyes, quantum dots and rare earth ions.

Organic dyes were among the first luminescent species to be considered for LSCs[12,18], because of their ready availability, optimal solubility in many organic solvents and matrices, generally high PLQY values and large absorption coefficients. Classes of organic molecules widely employed as LSC luminophores include rhodamines, coumarins and perylene derivatives[9]. The relatively narrow spectral absorption of most dyes poses a limitation to the harvesting efficiency over the whole solar spectrum. Multi-dye LSC plates, consisting in a single waveguide doped with several organic chromophores, have been proposed as an effective solution to absorb a wider fraction of the spectrum[19]. An added feature of such configuration is the occurrence of cascade emissions, where the radiation emitted by a first dye is re-absorbed by a second one and further downshifted through emission of the latter. Reiteration of the process throughout the series of dyes can efficiently convert short-wavelength absorbed photons into long-wavelength emitted radiation well-matched with the bandgap of the employed PV material, provided that all embedded dyes possess high PLQY values. Stacked-plates designs have also been investigated with the aim to combine different organic emitters in a cascade process, and at the same time to reduce escape cone losses, which account for the major drop in the optical efficiency of planar LSCs[20–22]. In a stack configuration, one collector can be tailored to re-absorb the photons lost by another, enhancing the amount of emitted light trapped in the device and successfully transported to the edge-coupled PV cells (Fig. 1.4). However, organic dyes still present significant drawbacks in view of LSC applications, as small Stokes shifts (< 30 nm)[23], which cause considerable self-absorption losses. Besides, the generally scarce photostability of organic emitters is the main reason hindering the development of large area and durable LSCs, due to the incompatibility between dye photobleaching timeframes and required lifetimes for the device[22].

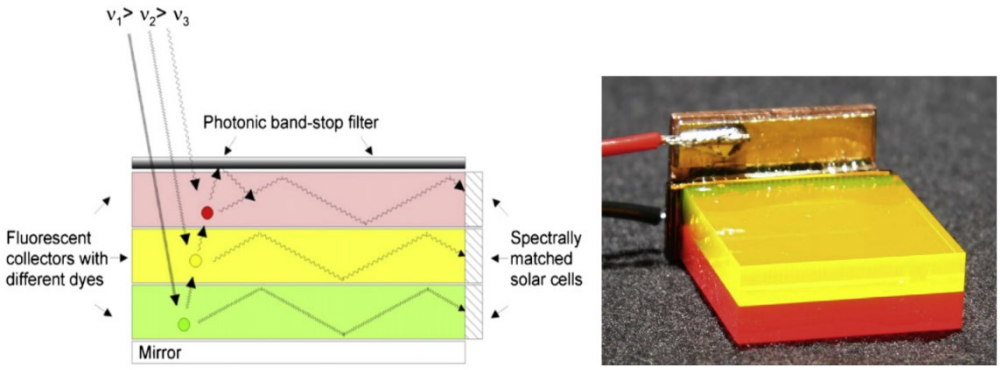


***Figure 1.4*** *Schematics of three LSC plates in a stacked configuration (left) and practical example of a two-dye stacked system (right)*[20].

Another class of emitting centres includes colloidal semiconductor nanocrystals, also referred to as quantum dots (QDs). Luminescent solar concentrators realized with such luminophores have been extensively reviewed[24–26], and count some of the most efficient large-area devices realized to date[27,28]. The most commonly employed materials for quantum dots are chalcogens and perovskites of zinc, cadmium and lead, thanks to their excellent optical properties, although ternary alloys of I-III-VI semiconductors ($CuInS_2$, $CuInSe_2$) and indirect bandgap semiconductors (Si, Ge) have also been proposed and are currently studied as more ecological alternatives[6]. In addition to large absorption coefficients over a broad spectral coverage and high PLQY values, QDs possess the peculiarity of size-dependent emissions, with increasing bandgap as the dimensions of the nanocrystals decrease (Fig. 1.5).

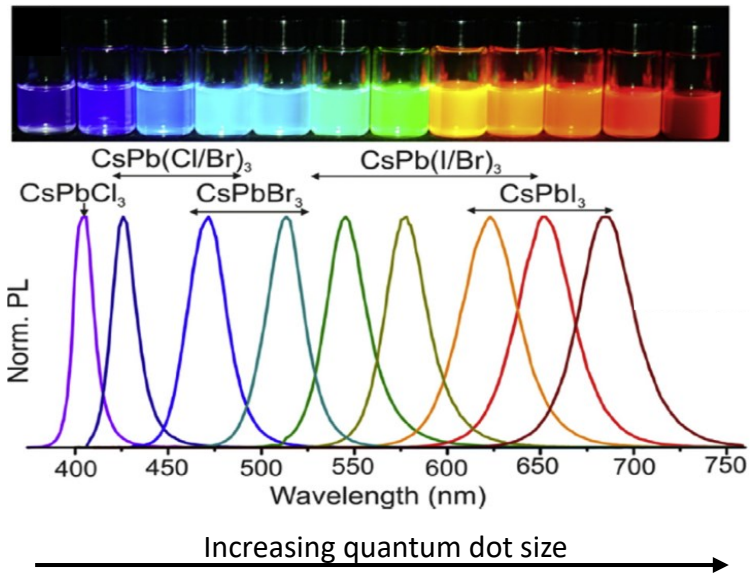


***Figure 1.5*** *Series of colloidal Pb-based perovskites with relative size-tunable emissions*[29].

In comparison to organic dyes, quantum dots display excellent photostability, although presenting similar self-absorption issues due to limited Stokes shifts. Hence, second generation QDs have been devised according to a "Stokes-shift engineering" approach, exhibiting reduced overlap between the absorption and emission bands thanks to appositely designed heterostructures. The most renowned examples are core-shell architectures, in which the absorption and emission processes are separated between different structural components, respectively an outer shell and an inner core made of different semiconductors[25]. Depending on whether one of the bandgaps of the two materials is larger or smaller than the other, different types of quantum dots can be obtained, which differ for the specific photophysical properties[30]. Potential downsides

in the use of quantum dots as LSC active components arise from their susceptibility to atmospheric oxygen, which can lead to surface oxidation during processing operations, resulting in the alteration of the QDs absorption and emission features[12]. It has also been observed that the incorporation into a solid medium can have detrimental effects on the quantum yield of the emitters, which can undergo luminescence quenching due to surface degradation[25]. Research into QD-based LSCs aims to address and improve such aspects, for example by designing core-shell structures with thicker outer layers that can suppress luminescence quenching caused by their chemical environment by better isolating the emissive core.

Rare earth ions, mainly $Eu^{3+}$, $Tb^{3+}$ and $Yb^{3+}$, are also being investigated as LSC emitters because of their large Stokes shifts (> 200 nm) and good quantum yields[9], although the poor absorption cross-section of $f \rightarrow f$ transitions, paired with narrow absorption bands, greatly affects the $\eta_{abs}$ contribute in the optical efficiency balance. Lanthanide luminescence can still be exploited by designing $Ln^{3+}$ complexes with organic ligands capable of enhancing the absorption properties of the emitter. This particular topic will be covered in detail later in Chapter 2.

Fig. 1.6 offers a summary of the spectral coverages and Stokes shifts for comparison between examples of the discussed luminophores.

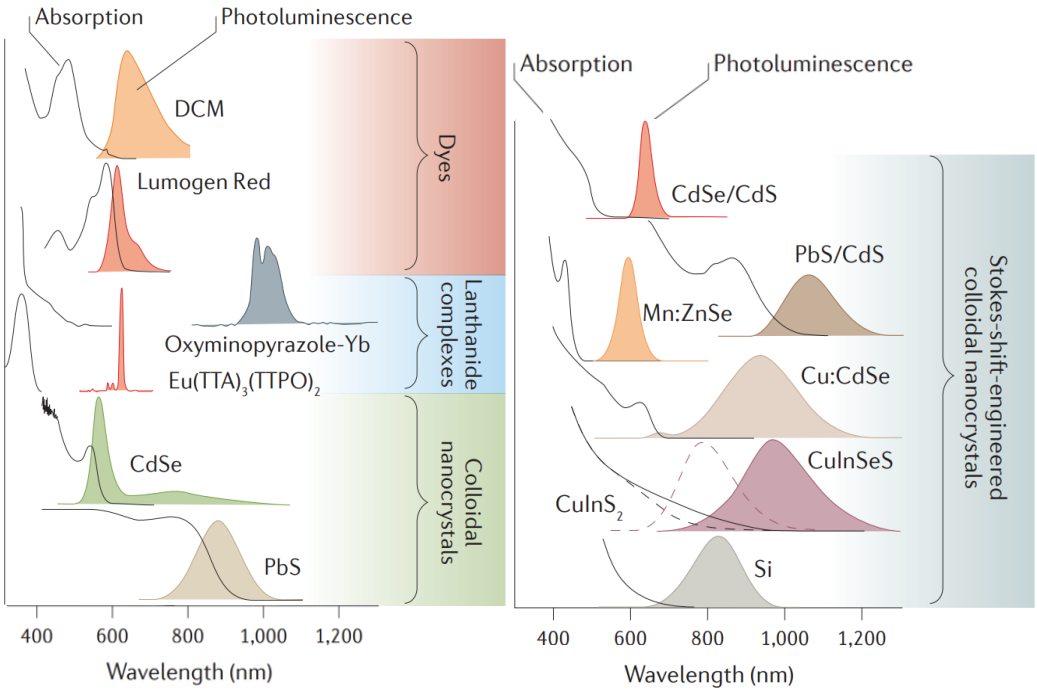


***Figure 1.6*** *Optical absorption and photoluminescence spectra of typical luminophores used in LSCs (adapted from ref. 3).*

## 1.3. Host matrix materials

The role of the host material in an LSC is far from neglectable, since the matrix should ideally be inconsequential to the absorption and re-emission process of the luminescent species. Desirable features for LSC host materials therefore include high refractive indexes, high transmittance in the visible and NIR spectral range, good solubility for the emitters, thermodynamic stability compatible with the processing conditions and with the final application, which in the case of BIPV implies prolonged durability in outdoor contexts[31].

Glass was initially appraised as the obvious choice for LSC waveguides, due to the appreciable transparency and the superior chemical and photophysical stability. Although being generally considered highly transmitting, soda-lime glass actually presents notable absorption features in the 800-1000 nm window (absorption cross section $\alpha \sim 0.5$ cm$^{-1}$), which is a relevant spectral region for LSCs coupled with silicon PV cells[3]. This and other unfavourable factors, such as the high temperatures required to fabricate conventional glass plates[31] and the limited doping concentrations accessible to most luminescent centres[8], have reduced the use of glass matrices. Nonetheless, glass is still widely employed as a transparent substrate for thin-films LSCs and, with the development of the sol-gel technique, its manufacturing for LSC applications could become more approachable.

On the other hand, polymeric matrices are currently the preferred option in LSCs, thanks to their high optical transparency and easy processability[32]. Polysiloxanes, polyacrylates and polycarbonates are among the commodity polymers that find the most widespread use in the field. Polidymethylsiloxane (PDMS) is the primary material under the polysiloxanes category. PDMS is a rubbery, flexible organic-inorganic matrix largely found in LSCs literature as a transparent encapsulant for luminophores (Fig. 1.7), due to ease of fabrication, high transmittance of light over a broad spectral region and mechanical and thermal stability[32]. PDMS is available as a liquid prepolymer that, upon blending with a curing agent, solidifies over time through a cross-linking process; the final obtained waveguide retains high flexibility, which is becoming a sought-after feature in view of realizing curved BIPV elements[33]. Compatibility with a wide range of luminophores, although limited by generally low solubility, makes PDMS a useful material for easy fabrication and functional testing of LSC waveguides.

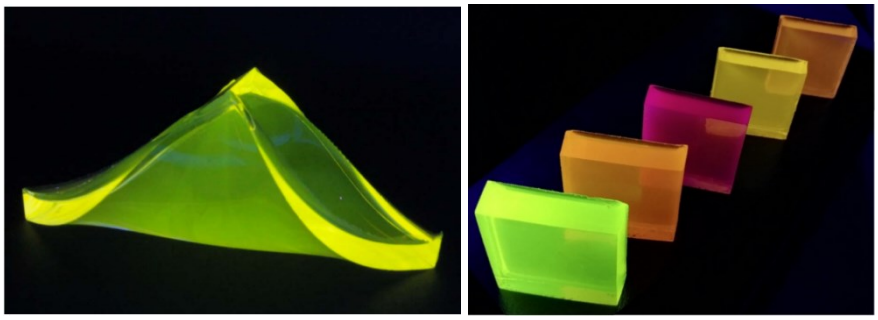

***Figure 1.7*** *Examples of flexible PDMS waveguides doped with organic chromophores, under UV light*[34,35].

Regarding polyacrylates, polymethylmethacrylate (PMMA) is undoubtedly the most employed, thanks to its excellent transparency to visible photons, high refractive index and fairly good photostability[31]. First signs of matrix absorption are observed beyond 800 nm due to the vibrational overtones of C-H bonds, which determine performance drops in the case of NIR-emitting luminophores. The absorption coefficient of PMMA in said spectral region ($\alpha = 3 \cdot 10^{-2}$ $cm^{-1}$) can be further reduced by fluorination of the C-H bonds, resulting in enhanced transparency to NIR photons ($\alpha = 2 \cdot 10^{-4}$ $cm^{-1}$ for the fluorinated polymer)[3]. In terms of thermal properties, PMMA possesses lower thermal conductivity with respect to glass, meaning smaller and slower temperature increases of the material with variations of ambient conditions. Although being brittle, PMMA shows some advantageous mechanical properties for LSC application, like high scratch resistance, greater impact strength than glass, and resistance to shattering upon breakage[32]. Bulk-doped waveguides in PMMA (Fig. 1.8) can be fabricated by polymerization of methyl methacrylate previously mixed with the luminophore, and subsequent cutting of the obtained slab in the desired shape.

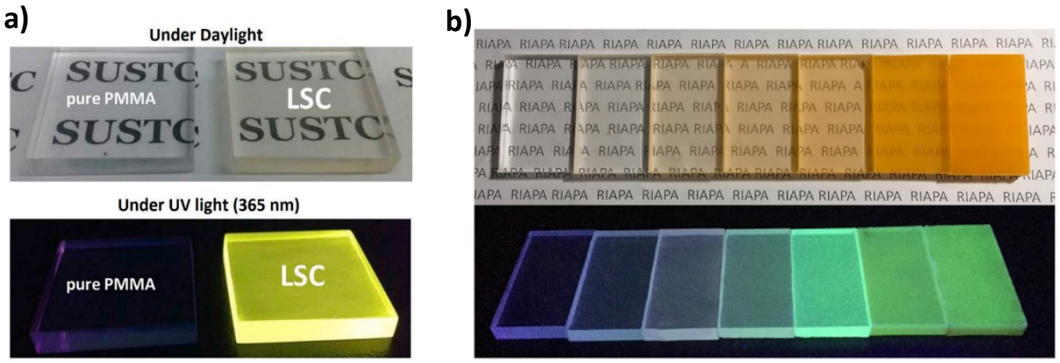


***Figure 1.8*** *Bulk-doped PMMA waveguides having a) full*[33] *or b) different degrees*[36] *of transparency, photographed under ambient lighting and under UV light.*

Thin films can also be realized by dissolving PMMA powder and the luminophore in a suitable solvent, casting of the solution through a coating method (i.e., spin-coating, doctor blading, etc…) and drying of the materials. A variant of PMMA often used in

QD-based LSCs for compatibility reasons and to minimize luminescence quenching is polylaurylmethacrylate (PLMA), usually co-polymerized with a crosslinker to achieve higher mechanical stability[32]. Polycarbonates (PC) are thermoplastics mainly used in thin film LSCs, due to the difficulties in synthetizing bulk PC tiles with standard laboratory equipment. Presenting high refraction indexes, polycarbonates show optimal light trapping properties, with a subsequent higher $\eta_{trap}$ for PC-based waveguides[16]. Other polymeric matrices found in LSC literature, not necessarily restricted to BIPV applications, include polystyrene, parylenes, polyamides, polyvinylpyrrolidone and environmentally-friendly materials like polylactic acid[31]. Although to a lesser extent with respect to solid hosts, liquid matrices have also been reported in the realization of LSCs[37–39]. Liquid systems offer the advantages of easy modification and adaptation of the device geometry to the desired shape, ample variability in luminophore concentrations, and the possibility of renewing the active layer after photo-degradation by replacing the emitter solution without touching the other LSC components[8]. Aqueous solution would be the more ecological choice, in order to avoid the use of large amounts of organic solvents. The limited compatibility between many luminophores and water is however an important drawback which current research aims to resolve; among the proposed alternatives microemulsions have been found to improve solubility of the emitters while maintaining the desired transparency[38] (Fig. 1.9).


***Figure 1.9*** *Cuvettes filled with a O/W microemulsion and a toluene solution of a completely water-insoluble organic dye, displaying unaltered optical transparency*[38].

## 1.4. Research work structure and goals

The goal of this thesis is to develop and characterize luminescent solar concentrators based on $Eu^{3+}$ antenna complexes embedded in polymeric hosts. The first employed luminophore is [Eu(tta)$_3$phen], a $Eu^{3+}$ β-diketone often found in LSC literature and here taken as a benchmark compound with respect to the second studied molecule, which is a newly synthetized di-nuclear lanthanide organic cage (LOC) of stoichiometry $[Eu_2(AFF)_4](NEt_4)_2$, where AFF is a bis-β-diketone ligand.

The first part of the work (Chapter 2) describes the two luminophores and deals with their synthesis and characterization. Successful formation of the complexes has been assessed through ESI mass spectrometry. The assembly of the LOC has been followed through NMR spectroscopy at each synthetic stage, and its hydrodynamic radius has been derived through DOSY spectroscopy. UV/Vis absorption and photoluminescence spectroscopies have been used to gain information on the photophysical properties of the emitters in solution.

The second part of the study (Chapter 3) deals with the preparation of polymeric LSC waveguides. A first report on the methods used to process the host materials will be provided, describing the optimization of the experimental procedures aimed at attaining the desired shape and optical quality for the final material. The developed methods have then been applied to the fabrication of luminescent LSC waveguides; the description of this step will address the incorporation of the luminescent species in the polymeric matrices and the further optimization of the experimental procedures needed to achieve good compatibility between the various components of the system. Insights on the waveguides composition and the effects that processing had on the materials have been obtained through powder XRD, TGA and DSC measurements. Photophysical characterization of the luminophores in the solid matrices has been carried out through UV/Vis absorption and photoluminescence spectroscopies.

In the last part of the thesis (Chapter 4), the performance of the fabricated LSCs has been assessed through functional characterizations. The used experimental setup has been devised for the first time in the scope of this work, hence a description of the validation and the refinement of measurements will be included. The measurements consisted in recording the I-V and P-V curves for a series of Si PV cells edge-coupled to the perimeter of the waveguides, under simulation of solar irradiation. Finally, the

main figures of merit discussed in the present introduction are provided for characterized LSCs.

Conclusions and perspectives are reported in Chapter 5, followed by the experimental part (Chapter 6).

## 1.5. References


1. *Solar generation 6: solar photovoltaic electricity empowering the world*. *European Photovoltaic Industry Association - EPIA* (2011).
2. Goetzberger, A., Hebling, C. & Schock, H.-W. Photovoltaic materials, history, status and outlook. *Mater. Sci. Eng. R Reports* **40**, 1–46 (2003).
3. Meinardi, F., Bruni, F. & Brovelli, S. Luminescent solar concentrators for building-integrated photovoltaics. *Nat. Rev. Mater.* **2**, 1–9 (2017).
4. Traverse, C. J., Pandey, R., Barr, M. C. & Lunt, R. R. Emergence of highly transparent photovoltaics for distributed applications. *Nat. Energy* **2**, 849–860 (2017).
5. Ferreira, R. A. S., Correia, S. F. H., Monguzzi, A., Liu, X. & Meinardi, F. Spectral converters for photovoltaics – What's ahead. *Materials Today* **33**, 105–121 (2020).
6. Mazzaro, R. & Vomiero, A. The Renaissance of Luminescent Solar Concentrators: The Role of Inorganic Nanomaterials. *Advanced Energy Materials* **8**, 1801903 (2018).
7. Meinardi, F. *et al.* Highly efficient luminescent solar concentrators based on earth-Abundant indirect-bandgap silicon quantum dots. *Nat. Photonics* **11**, 177–185 (2017).
8. Roncali, J. Luminescent Solar Collectors: Quo Vadis? *Advanced Energy Materials* **10**, 2001907 (2020).
9. Correia, S. F. H. *et al.* Luminescent solar concentrators: Challenges for lanthanide-based organic-inorganic hybrid materials. *J. Mater. Chem. A* **2**, 5580–5596 (2014).
10. Batchelder, J. S., Zewail, A. H. & Cole, T. Luminescent solar concentrators. 1: Theory of operation and techniques for performance evaluation. *Appl. Opt.* **18**, 3090–3110 (1979).

11. Goetzberger, A. & Greube, W. Solar energy conversion with fluorescent collectors. *Appl. Phys.* **14**, 123–139 (1977).
12. Debije, M. G. & Verbunt, P. P. C. Thirty years of luminescent solar concentrator research: Solar energy for the built environment. *Adv. Energy Mater.* **2**, 12–35 (2012).
13. Kanellis, M., de Jong, M. M., Slooff, L. & Debije, M. G. The solar noise barrier project: 1. Effect of incident light orientation on the performance of a large-scale luminescent solar concentrator noise barrier. *Renew. Energy* **103**, 647–652 (2017).
14. https://www.eni.com/en-IT/operations/concentrators-solar-luminescent.html (last acessed: July 2022).
15. Papakonstantinou, I., Portnoi, M. & Debije, M. G. The Hidden Potential of Luminescent Solar Concentrators. *Advanced Energy Materials* **11**, 2002883 (2021).
16. Zettl, M., Mayer, O., Klampaftis, E. & Richards, B. S. Investigation of Host Polymers for Luminescent Solar Concentrators. *Energy Technol.* **5**, 1037–1044 (2017).
17. Altermatt, P. P. *Silicon solar cells*. *Optoelectronic Devices: Advanced Simulation and Analysis* (The Royal Society of Chemistry, 2005). doi:10.1007/0-387-27256-9_11.
18. Batchelder, J. S., Zewail, A. H. & Cole, T. Luminescent solar concentrators 2: Experimental and theoretical analysis of their possible efficiencies. *Appl. Opt.* **20**, 3733 (1981).
19. Rowan, B. C., Wilson, L. R. & Richards, B. S. Advanced material concepts for luminescent solar concentrators. *IEEE J. Sel. Top. Quantum Electron.* **14**, 1312–1322 (2008).
20. Goldschmidt, J. C. *et al.* Increasing the efficiency of fluorescent concentrator systems. *Sol. Energy Mater. Sol. Cells* **93**, 176–182 (2009).
21. Richards, B. S. & McIntosh, K. R. Ray-tracing simulations of luminecent solar concentrators containing multiple luminescent species. in *21st European Photovoltaic Solar Energy Conference* 185–188 (2006).
22. Hermann, A. M. Luminescent solar concentrators-A review. *Sol. Energy* **29**, 323–329 (1982).
23. Yang, C. *et al.* Impact of Stokes Shift on the Performance of Near-Infrared

Harvesting Transparent Luminescent Solar Concentrators. *Sci. Rep.* **8**, 1–10 (2018).

24. Purcell-Milton, F. & Gun'ko, Y. K. Quantum dots for Luminescent Solar Concentrators. *J. Mater. Chem.* **22**, 16687–16697 (2012).
25. Pietryga, J. M. *et al.* Spectroscopic and device aspects of nanocrystal quantum dots. *Chem. Rev.* **116**, 10513–10622 (2016).
26. Moraitis, P., Schropp, R. E. I. & van Sark, W. G. J. H. M. Nanoparticles for Luminescent Solar Concentrators - A review. *Opt. Mater. (Amst).* **84**, 636–645 (2018).
27. Sadeghi, S. *et al.* High-Performance, Large-Area, and Ecofriendly Luminescent Solar Concentrators Using Copper-Doped InP Quantum Dots. *iScience* **23**, 101272 (2020).
28. Li, H., Wu, K., Lim, J., Song, H. J. & Klimov, V. I. Doctor-blade deposition of quantum dots onto standard window glass for low-loss large-area luminescent solar concentrators. *Nat. Energy* **1**, 1-9 (2016).
29. Zhao, H. & Rosei, F. Colloidal Quantum Dots for Solar Technologies. *Chem* **3**, 229–258 (2017).
30. Vasudevan, D., Gaddam, R. R., Trinchi, A. & Cole, I. Core-shell quantum dots: Properties and applications. *J. Alloys Compd.* **636**, 395–404 (2015).
31. Griffini, G. Host matrix materials for luminescent solar concentrators: Recent achievements and forthcoming challenges. *Front. Mater.* **6**, 1–8 (2019).
32. Li, Y., Zhang, X., Zhang, Y., Dong, R. & Luscombe, C. K. Review on the Role of Polymers in Luminescent Solar Concentrators. *J. Polym. Sci. Part A Polym. Chem.* **57**, 201–215 (2019).
33. Rafiee, M., Chandra, S., Ahmed, H. & McCormack, S. J. An overview of various configurations of Luminescent Solar Concentrators for photovoltaic applications. *Opt. Mater. (Amst).* **91**, 212–227 (2019).
34. Tummeltshammer, C., Taylor, A., Kenyon, A. J. & Papakonstantinou, I. Flexible and fluorophore-doped luminescent solar concentrators based on polydimethylsiloxane. *Opt. Lett.* **41**, 713−716 (2016).
35. Gao, S. *et al.* Highly Efficient Luminescent Solar Concentrators Based on Benzoheterodiazole Dyes with Large Stokes Shifts. *Chem. – A Eur. J.* **26**, 11013–11023 (2020).
36. Bagherzadeh-Khajehmarjan, E., Nikniazi, A., Olyaeefar, B., Ahmadi-Kandjani,

S. & Nunzi, J. M. Bulk luminescent solar concentrators based on organic-inorganic CH3NH3PbBr3 perovskite fluorophores. *Sol. Energy Mater. Sol. Cells* **192**, 44–51 (2019).

37. Frias, A. R. *et al.* Sustainable Liquid Luminescent Solar Concentrators. *Adv. Sustain. Syst.* **3**, 1800134 (2019).
38. Congiu, A. *et al.* Microemulsions for luminescent solar concentrator application. *Sol. Energy* **216**, 338–350 (2021).
39. Liu, X. *et al.* Eco-friendly quantum dots for liquid luminescent solar concentrators. *J. Mater. Chem. A* **8**, 1787–1798 (2020).

# Chapter 2

# Luminophore studies

This Chapter will address the photophysical process that leads to the luminescence of lanthanide antenna complexes, as well as the design and synthesis of the luminescent systems employed in the present study. NMR spectroscopy and ESI mass spectrometry have been used to confirm successful luminophores formation, while optical characterizations have been performed through UV/Vis absorption and photoluminescence spectroscopies.

## 2.1. $Ln^{3+}$ antenna complexes

The distinct optical properties of lanthanide elements have sparked great scientific interest over the years, making them the object of study in several luminescence-related fields, ranging from laser physics to biomedical sensing and imaging[1]. As we are concerned with exploiting lanthanide luminescence in materials for light-conversion purposes, an understanding of the photophysical processes at play and how they may vary with the surrounding environment is of utmost importance.

"Lanthanides", or "lanthanoids", are identified as the elements spanning from lanthanum (atomic number 57) to lutetium (atomic number 71), and are characterized by the gradual filling of 4*f* orbitals[2]. They present a general electronic configuration $[Xe]4f^n6s^2$ (n = 1-14), except for La, which does not possess any *f* electrons. Irregularities in the occupation of 4*f* orbitals are also found for Ce, Gd and Lu, which achieve a more stable configuration by half-filling an additional 5*d* orbital.

Lanthanide ions are most stable in the oxidation state +3, with $Ln^{3+}$ ions showing

similar reactivity and chemical properties, as well as a regular decrease in ionic radius along the series. Such behaviour can be ascribed to the core-like character of the 4*f* subshell: having a smaller radial expansion than the 5d and 6s subshells, its orbitals are little affected by the molecular environment, and do not contribute significantly to bonding with ligands. This same feature also determines the peculiar and most interesting emission phenomena of lanthanide complexes. In fact, among the energy contributions determining the electronic structure of lanthanide ions, the perturbation arising from spin-orbit coupling is significantly stronger than that originated by eventual ligands (Fig. 2.1)[3].

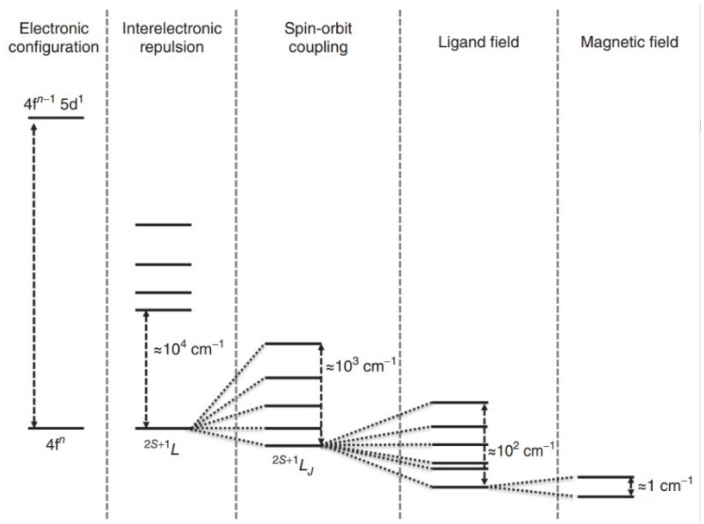


***Figure 2.1*** *General energetic structure for a lanthanide ion in the presence of different perturbations, evidencing their relative orders of magnitude.*

This implies that the energy levels splitting patterns for 4*f* electrons in the free ion do not undergo any substantial change even in the presence of a crystal field of given symmetry; consequently, the photoluminescence spectra of lanthanide complexes share great similarity with those of the corresponding free ions[4]. The bands observed in such spectra, arising from electronic transitions confined within the 4*f* subshell, present sharp and narrow shapes, resembling those of atomic emission lines (Fig. 2.2).

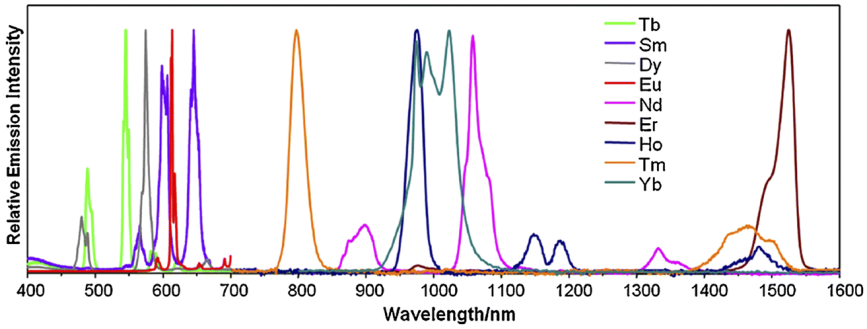


***Figure 2.2*** *Normalized photoluminescence spectra of lanthanide complexes emitting in the visible and NIR*[5].

Intraconfigurational electric dipole transitions, such as $f \rightarrow f$ transitions, are parity-forbidden due to the Laporte selection rule, but can become partly allowed by vibronic coupling or configuration mixing thanks to the effects of a ligand field[6]. The degree of relaxation of Laporte rule remains limited, and molar absorption coefficients in lanthanide spectra rarely exceed $10^{-1}$ $M^{-1}$ $cm^{-1}$ as order of magnitude.

Nonetheless, the problem of low $f \rightarrow f$ absorption cross-sections can be overcome by indirect population of the emissive excited state through the so-called "antenna effect"[7]. This effect is achieved by coordinating the lanthanoid ion of interest with suitable organic chromophores, characterized by large molar absorption coefficients in the UV/Vis region. The antenna efficiently absorbs the incident light, undergoing an allowed electronic transition from singlet ground state $S_0$ to singlet excited state $S_1$. Next, an intersystem crossing process populates the ligand-centered triplet state $T_1$. At this point, an intramolecular energy transfer takes place towards $Ln^{3+}$ excited states, which radiatively decay to the ground state. The overall mechanism of the $Ln^{3+}$ sensitized emission is resumed in the following diagram (Fig. 2.3).

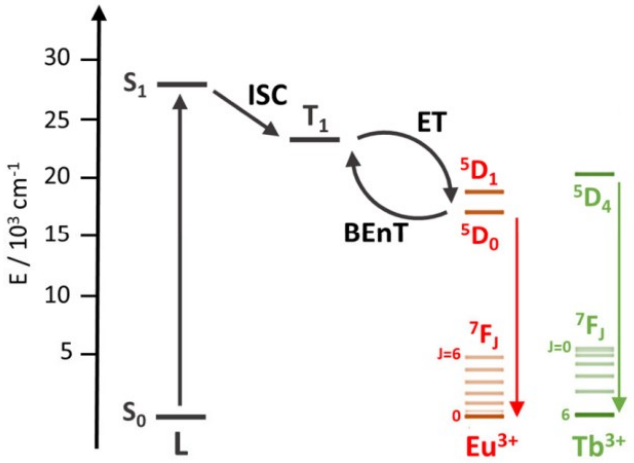


***Figure 2.3*** *Schematization of the antenna effect for red emitter $Eu^{3+}$ and green emitter $Tb^{3+}$, where ISC = intersystem crossing, ET = energy transfer, BEnT = back energy transfer.*

The total sensitization efficiency can be defined as follows:

$$\Phi_{SE} = \Phi_{ISC}\Phi_{ET}\Phi_{Ln} \qquad (2.1)$$

where the three distinct contributions are the intersystem crossing efficiency ($\Phi_{ISC}$), the energy transfer efficiency ($\Phi_{ET}$) and the photoluminescence quantum yield of the lanthanoid ion ($\Phi_{Ln}$). Since the seminal work of Weissmann in 1942[8], who was the first to observe the luminescence enhancement of $Eu^{3+}$ ions when complexed with organic ligands, many studies have been conducted to gain insights into what governs

the sensitization efficiency and how it might be improved by chromophore design[9–11]. During the whole photophysical process, the system may access several deactivation pathways, resulting in the quenching of metal-centered luminescence. For example, the excited states of the antenna could decay radiatively before performing energy transfer, resulting in fluorescence or phosphorescence of the ligand only. Also, the probability of a back energy transfer from metal to ligand could not be negligible. These phenomena can be controlled by tailoring the energy difference between the $T_1$ state of the antenna and the emissive excited state of the ion: for an efficient energy transfer, the donor level should be higher in energy than the acceptor level by at least 1850 $cm^{-1}$ [12].

Luminescence quenching by vibrations of the molecular environment is a further possible deactivation pathway for the antenna effect. High energy oscillators like O-H and N-H stretching modes, especially when directly coordinated to the $Ln^{3+}$ ion, have pronounced detrimental effects on the sensitization efficiency[13]. One way to reduce vibronic quenching is to design a rigid molecular scaffold around the metal centre, free of said high energy vibrations in its vicinity and shielding from solvent interactions, as they too cause vibronic deactivation, although of minor entity.

Lastly, a suitable antenna should confer thermodynamic and kinetic stability to the desired. Given the lability of lanthanide ions and their tendency to reach high coordination numbers, it is favourable to employ polydentate and chelating ligands, especially O− and N− donors. Macrocyclic polyaminocarboxylates as DOTA and derivatives have been reported to form some of the most stable $Ln^{3+}$ complexes, coordinating the ion through a polyaza-ring and additional carboxylate binding sites[13]. Other efficiently chelating ligands often used for $Ln^{3+}$ coordination are β-diketonates, acyclic Schiff base derivatives and aromatic chromophores such as phenanthroline and bipyridine[14].

## 2.2. Choice of the ligand: β-diketones

A class of ligands widely employed in coordination chemistry is that of 1,3-dicarbonyls, or β-diketones. They readily undergo keto-enol tautomerization, with preference for the enolic form. Their corresponding conjugated base, obtainable upon α-deprotonation, serves as an anionic chelating ligand for many *d*-block and *f*-block metal centres.

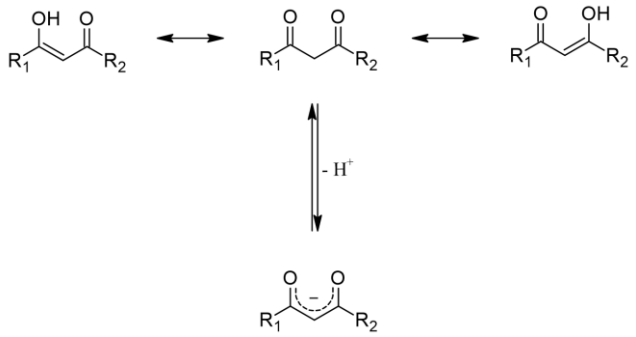


***Figure 2.4*** *Resonance formulas for the keto-enol tautomerization of a generic β-diketone, in equilibrium with formation of the associated β-diketonate.*

The photophysical properties of β-diketones, and consequently their eligibility to sensitize lanthanide ions, depend on the nature of substituents: better sensitization is usually observed for complexes containing aromatic β-diketonates with respect to aliphatic ones; also, the presence of fluorinated moieties helps to suppress non-radiative deactivation processes[15]. Increasing the hydrophobicity of the complex by inserting large hydrophobic groups into the β-diketone's structure further reduces the occurrence of vibrational relaxation conveyed by solvent molecules. To fully prevent solvent interactions with the metal ion, it is important to saturate its coordination sphere. Strong Lewis bases, such as the aforementioned 2,2'-bipyridine (bpy) and 1,10-phenanthroline (phen), are often used as auxiliary ligands in lanthanide β-diketonates and are known to further increase the luminescence quantum yield. It is also possible to design 1,3-dicarbonyls containing more than one binding site, allowing the formation of polynuclear complexes by coordination of multiple metal ions. Photophysical investigations on binuclear[16] and trinuclear[17] $Eu^{3+}$ β-diketonates report large increments in sensitized luminescence when compared to the corresponding mononuclear complexes.

A family of polydentate bis-β-diketones has already been designed and extensively studied as sensitizers by the thesis research group in previous works[18,19]. These ligands have a structure consisting of two benzoyltrifluoroacetone (btfa) moieties linked by a

series of three different central spacers (Fig. 2.5 and 2.6). The btfa group is well known to be a good sensitizer for specific $Ln^{3+}$ such as $Eu^{3+}$ [20].

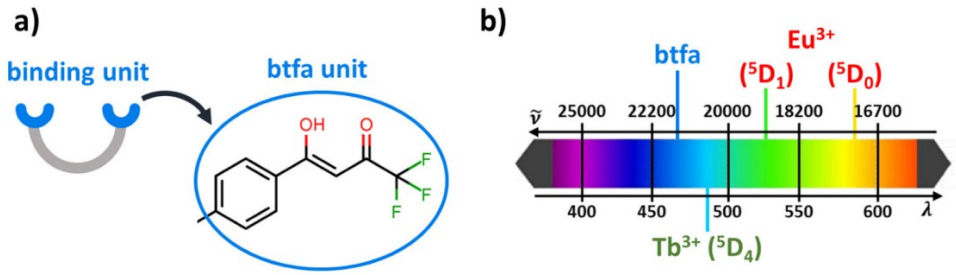


***Figure 2.5*** *Depiction of a) the generic structure of developed bis-β-diketones, and b) the relative positions of the energy levels involved in the sensitization of $Tb^{3+}$ and $Eu^{3+}$ ions by btfa.*

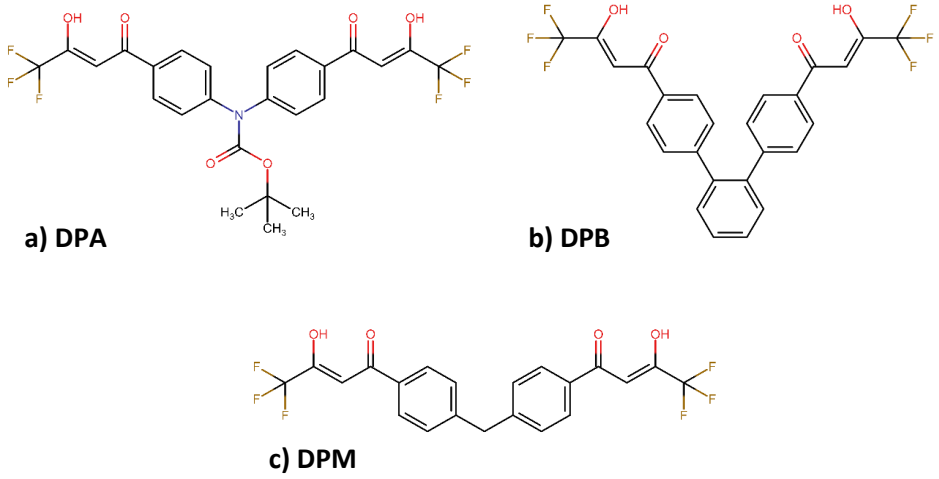


***Figure 2.6*** *Structure formulas for the developed bis-β-diketones and assigned labels according to different central scaffolds: a) carbamate group, b) phenyl group, c) methylene group.*

Complexation of lanthanide ions with such ligands leads to formation of supramolecular lanthanide organic cages (LOCs) of stoichiometry $[Ln_2(diketonate)_4]^{2-}$ and lantern-like structure as shown in Fig. 2.7. The cation formed by the base employed to deprotonate the ligand serves as a counterion for the anionic cage. Detailed studies of LOCs' luminescence and supramolecular host-guest properties, besides investigation into their application as chiro-optic sensors, have been recently reported[18,19].

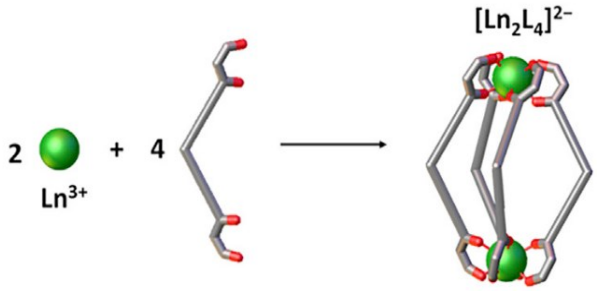


***Figure 2.7*** *General formation scheme of supramolecular LOCs of formula $[Ln_2L_4]^{2-}$.*

## 2.3. LOCs as luminophores for LSC applications

Among the requirements and desired features that define a good luminophore for LSC applications, LOCs possess large Stokes shifts (~ 250 nm), high absorption coefficients in the UV/Vis spectral region, optimized luminescence efficiencies and emission energies well-matched with the responsivity maximum of Si-based photovoltaic cells. Moreover, $Eu^{3+}$ cages based on the bis-β-diketone ligands above discussed show particularly high brightness values (~ 50000 $M^{-1}$ $cm^{-1}$) that, under sunlight exposure, result in luminescence detectable even to the naked eye. Brightness is a useful parameter for describing the emission efficiency of a luminescent species, in that is defined as the product between its molar absorption coefficient ($\varepsilon_{max}$) and photoluminescence quantum yield (PLQY).

While aiming to lay the first steps towards LOCs implementation in LSC devices, the complexity of such systems calls for preliminary studies on a simpler luminophore, already well known and characterized in literature. Europium(III) β-diketonate [$Eu(tta)_3phen$], where tta = thenoyltrifluoroacetone, was adopted as benchmark compound with respect to LOCs during all stages of sample development. Several studies indicate that the characteristic red emission of $Eu^{3+}$ shown by this complex is retained upon embedding in various polymeric matrixes[21–23]. Appreciable solubility in a wide range of organic solvents allows an easy and versatile handling of the luminophore during waveguide fabrication operations.

Moving on to LOCs, $[Eu_2(DPA)_4](NEt_4)_2$ was chosen for preliminary tests among the series described before, where DPA is the bis-β-diketone bearing a tert-butyl carbamate spacer and the tetraethylammonium counterion derives from protonation of the employed base, tetraethylammonium hydroxide. Due to solubility issues, a small modification of the DPA ligand was introduced, as the fluorinated terminal chains were extended by an additional $-CF_2-$ unit (Fig. 2.8). This new version of the ligand was synthetized and employed to obtain the cage $[Eu_2(AFF)_4](NEt_4)_2$, which showed increased solubility in employed solvents. Compatibility studies between luminophores, solvents and host materials, as well as sample fabrication, are covered in detail later in Chapter 3 of the thesis.

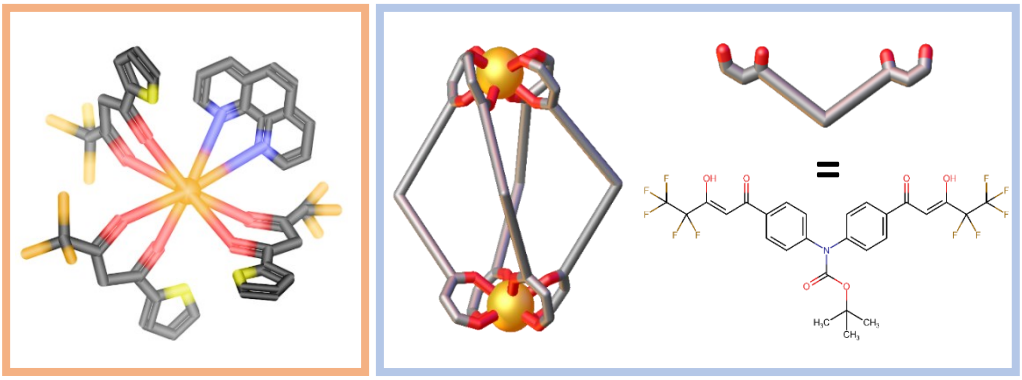

***Figure 2.8*** *Structure depictions for [Eu(tta)₃phen] complex (left) and newly synthetized cage [Eu₂(AFF)₄](NEt₄)₂ with relative ligand (right).*

## 2.4. Synthesis and characterization of luminophores

**– [Eu(tta)₃phen]**

A simple synthetic route for rare earth β-diketonates was first provided in 1964 by Bauer et al., when they assessed the formation of crystalline compounds of composition $[Ln(\beta\text{-diketonate})_4]^-(counterion)^+$ and $[Ln(\beta\text{-diketonate})_3L']$, where L' is a neutral ancillary chelating ligand, from a considerable variety of β-diketones and organic bases[24]. The here adapted procedure for [Eu(tta)₃phen] synthesis comprised a first deprotonation of thenoyltrifluoroacetone in ethanol with NaOH, followed by addition of phenanthroline. Next, addition of an ethanolic solution of europium(III) chloride to the ligand mixture caused immediate formation of a white fine solid, which was isolated through filtration and purified by recrystallization from THF.

The reagents were employed in a Eu/tta/NaOH/phen molar ratio of 1:3:3:1. Being already commercially available, the β-diketone was purchased and used as received.

**– [Eu₂(AFF)₄](NEt₄)₂**

The AFF ligand was obtained following a two-step procedure (Fig. 2.9). First, a Cu(I)-catalysed amino coupling was performed between *para*-bromoacetophenone and *tert*-butyl carbamate. The formation of 1,3-diketone moieties was then achieved by Claisen condensation between the obtained precursor and ethyl pentafluoropropionate. The final product was purified by $SiO_2$ column chromatography and recrystallization from an acetonitrile/water 1:4 mixture.

Formation of the $[Eu_2(AFF)_4](NEt_4)_2$ cage is straightforward: the bis-β-diketone ligand was initially dissolved in ethanol and deprotonated using a ~ 1.5 M methanolic solution of tetraethylammonium hydroxide (TEAOH), then a solution of europium(III) chloride in ethanol was added to the ligand mixture. A suspension of fine white solid promptly formed upon lanthanide salt addition, which was separated by centrifugation. The reagents were employed in a Eu/AFF/TEAOH molar ratio of 1:2.5:5. The excess of base assured a quantitative deprotonation of the ligand, in order to obtain the tetrakis-chelated LOC as main reaction product with respect to under-coordinated stoichiometries.

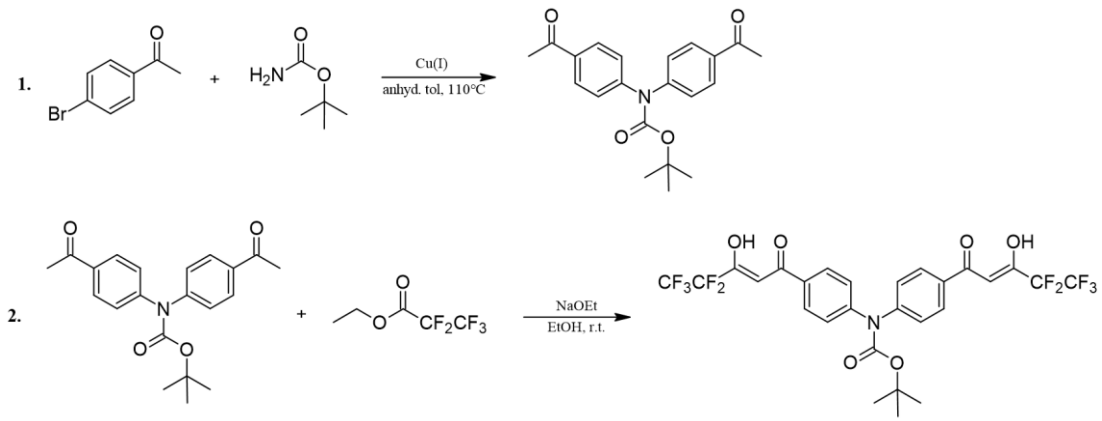


***Figure 2.9*** *Reaction sequence adopted for the synthesis of the AFF ligand.*

## 2.4.1. Mass spectrometry

An ESI-MS spectrum was collected for the new AFF ligand and is provided in Fig. 2.10, where the molecular peak is identified at 644.28 m/z. Fragmentation of the main peak is elucidated in the corresponding MS/MS spectra and comprises first loss of the tert-butyl formate group, with following loss of one β-diketonate moiety.

Formation of $[Eu(tta)_3phen]$ and $[Eu_2(AFF)_4](NEt_4)_2$ has been confirmed through mass spectrometry. The collected ESI-MS spectrum of $[Eu(tta)_3phen]$ shows a single signal at 1037.11 m/z in negative mode, relative to the molecular ion associated with an acetonitrile solvent molecule (Fig. 2.11a). The mass spectrum of $[Eu_2(AFF)_4](NEt_4)_2$ shows only one signal as well, at 1439.34 m/z (negative mode), identified as the doubly negatively charged species $[Eu_2(AFF)_4]^{2-}$ (Fig. 2.11b). The monocharged ion signal is not present in the spectrum, due to its *m/z* value exceeding the instrumental detection range. The associated experimental isotopic patterns for both species agree with the calculated ones (insets of Fig. 2.11).

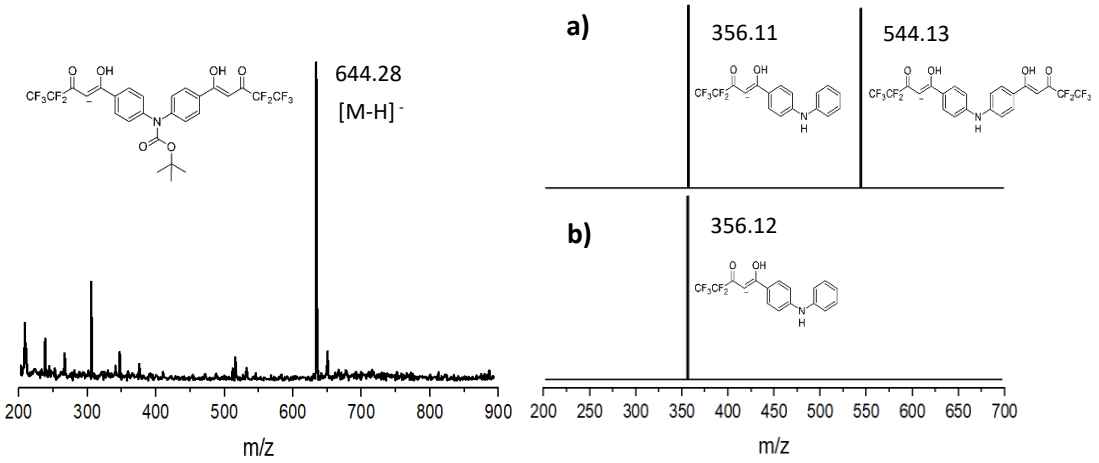


***Figure 2.10*** *ESI mass spectrum of the AFF ligand (left), with MS/MS fragmentations relative to a) 644.28 m/z and b) 544.13 m/z signals (right).*

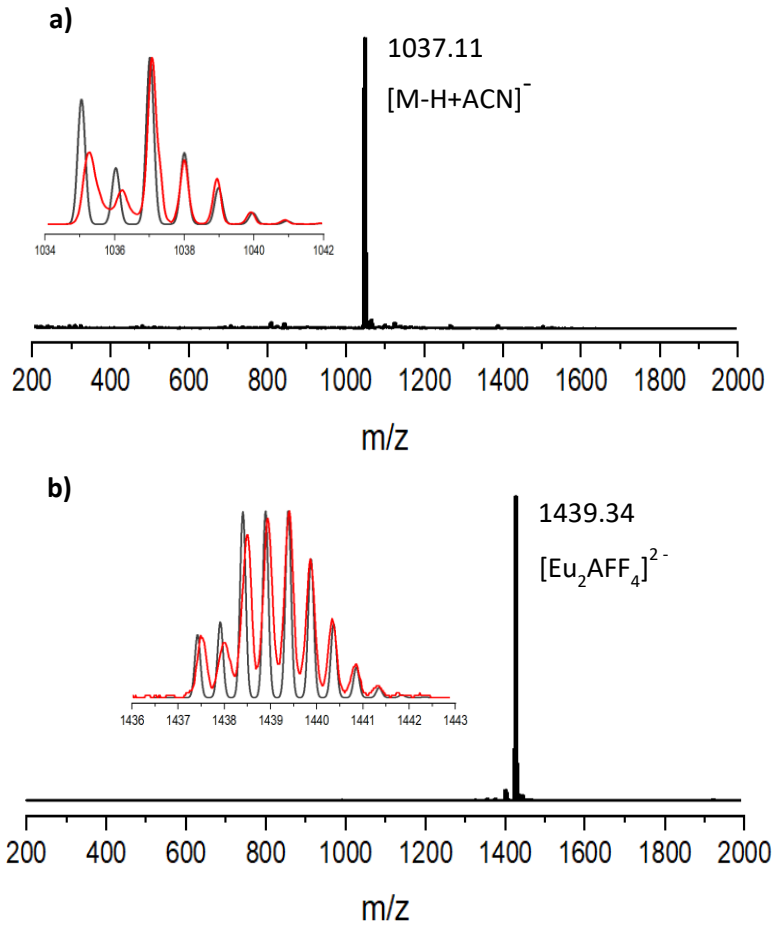


***Figure 2.11*** *ESI mass spectra of a) [Eu(tta)₃phen] and b) [Eu₂(AFF)₄](NEt₄)₂. Insets: experimental (red line) and simulated (black line) isotopic patterns.*

## 2.4.2. NMR spectroscopy

Successful obtainment of the ligand precursor (Fig. 2.9, step 1) was verified by $^{1}$H-NMR spectroscopy; the collected spectrum is provided in Fig. 2.12, along with peak assignations. The formation of LOCs can too be assessed and monitored via $^{1}$H-NMR. Coordination of $Eu^{3+}$ significantly complicates interpretation of the spectrum, due to the nucleus paramagnetic nature, so the $^{1}$H-NMR analysis was performed on an analogous cage prepared with diamagnetic $La^{3+}$ ions. Fig. 2.13 shows a sequence of spectra collected for $[La_2(AFF)_4](NEt_4)_2$, comprising those of the ligand in its protonated and deprotonated form (AFF, $AFF^{2-}$) and that of the final assembled cage $[La_2AFF_4]^{2-}$. Upon deprotonation, all the ligand signals undergo upfield shifting. The strongest effect is observed for the proton H1, in α position of the β-diketonate moiety, shifting from *ca.* 7.2 to *ca.* 5.8 ppm while the tert-butyl protons (H4) are barely perturbated. After $La^{3+}$ coordination, the cage shows only a single set of signals with a total of four resonances in agreement with the ligand $C_2$ symmetry and the mean $C_4$ symmetry of the quadruple-stranded $[La_2L_4]^{2-}$ architecture. H1, the H atom closer to the metal center, is downfield shifted to *ca.* 6.3 ppm.

$^{19}$F-NMR spectroscopy was also used to characterize the $[La_2(AFF)_4](NEt_4)_2$ cage, an analogous series of spectra is shown in Fig. 2.14. Deprotonation of the ligand causes downfield shifting of both signals, with a more pronounced effect for the F2 fluorine atoms. As in the case of $^{1}$H-NMR spectra, coordination of $La^{3+}$ produces only a single set of signals, in accordance with the $C_4$ symmetry of the $[La_2AFF_4]^{2-}$ cage.

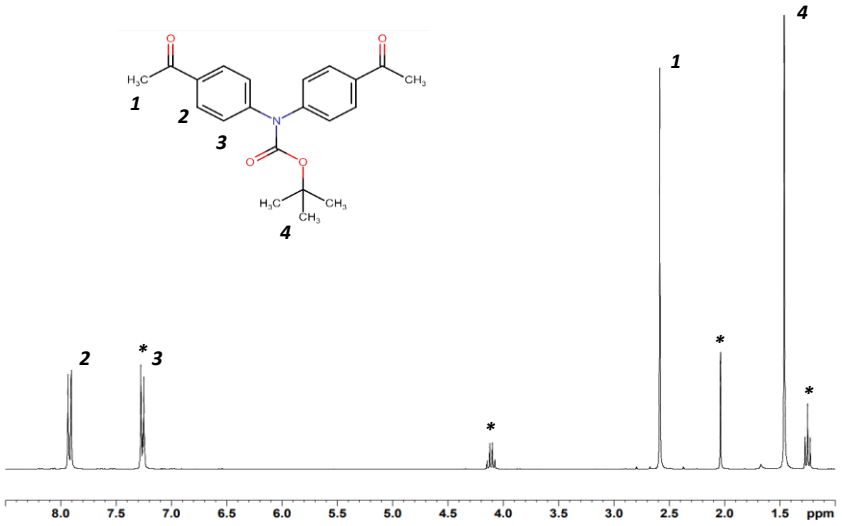


***Figure 2.12*** *$^{1}$H-NMR spectra (25 °C, 300 MHZ, $CDCl_3$) of the AFF ligand precursor. Solvent signals are marked with an asterisk.*

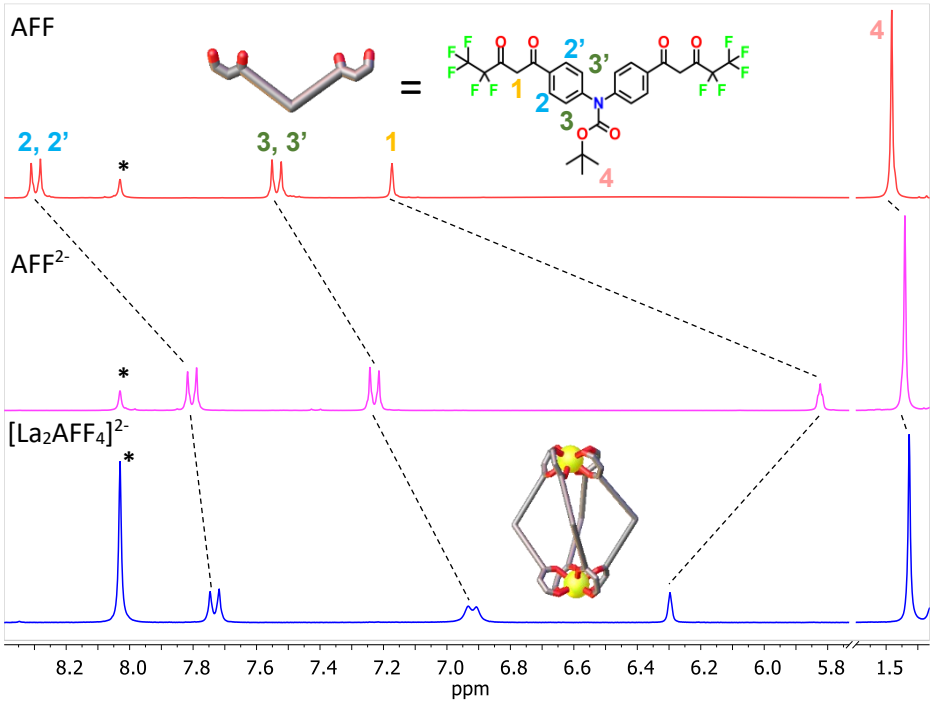


***Figure 2.13*** *$^{1}$H-NMR spectra (25 °C, 300 MHz, DMF-d) of ligand AFF, deprotonated ligand $AFF^{2-}$ and cage $[La_2AFF_4]^{2-}$. Solvent signals are marked with an asterisk.*

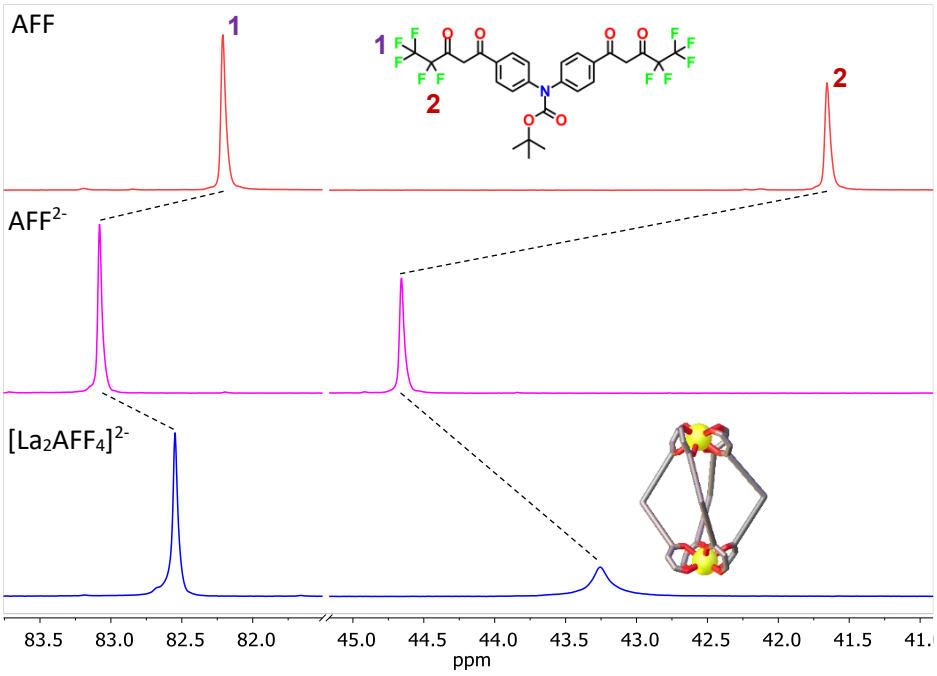


***Figure 2.14*** *$^{19}$F-NMR spectra (25 °C, 200 MHz, DMF-d) of ligand AFF, deprotonated ligand $AFF^{2-}$ and cage $[La_2AFF_4]^{2-}$.*

Diffusion-ordered NMR spectroscopy (DOSY) was performed to provide dimensional information (Fig. 2.15). Two distinct bands were observed and ascribed to the cage and to the $NEt_4^+$ cation. The calculated hydrodynamic diameter for $[La_2AFF_4]^{2-}$ is 22.18 Å. This value well-agrees with the hydrodynamic diameter calculated from DOSY experiments and with the values deduce by single crystal X-ray structure for $[La_2DPA_4]^{2-}$ and $[Eu_2DPA_4]^{2-}$ cages, respectively, as recently reported[18].

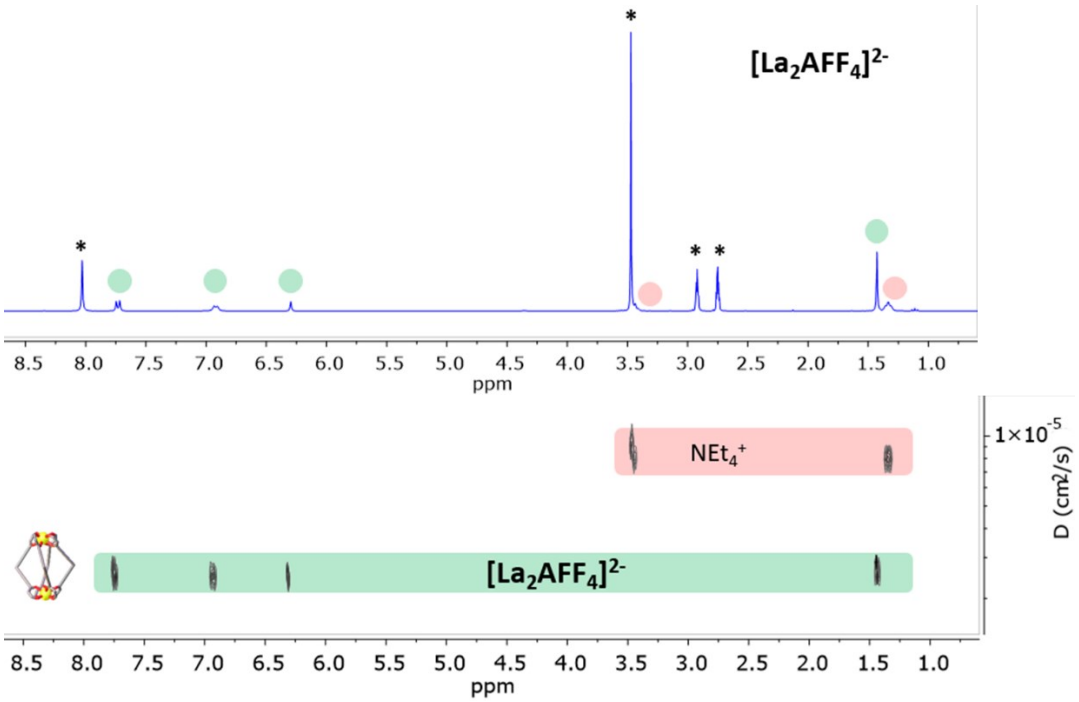


***Figure 2.15*** *DOSY spectrum (30 °C, 400 MHz, DMF-d) of cage $[La_2AFF_4]^{2-}$. Signals grouped in the same DOSY band are indicated in the $^1$H-NMR spectrum with a dot of the same colour. Solvent signals (DMF and MeOH) are marked with an asterisk.*

## 2.4.3. Photophysical characterizations

Both $[Eu(tta)_3phen]$ and $[Eu_2(AFF)_4](NEt_4)_2$ were characterized with UV-Vis absorption and photoluminescence (PL) spectroscopies.

Absorption spectra of both complexes present a broadened absorption band with the maximum falling close to 340 nm (Fig. 2.16a). Such absorption profiles confirm a ligand-centered excitation for both complexes, es expected based on literature data for $[Eu(tta)_3phen]$[25] and on previous LOCs characterizations for $[Eu_2(AFF)_4](NEt_4)_2$[19]. While sharing a similar band shape, the absorption exhibited by the cage has a molar extinction coefficient almost five times larger with respect to that of $[Eu(tta)_3phen]$ (see Table 2.1).

The progression of $^5D_0 \rightarrow {}^7F_J$ transitions for the $Eu^{3+}$ ion is well recognizable in the PL spectra of both species, with the highest intensity registered for the $^5D_0 \rightarrow {}^7F_2$ transition (612 nm), which is about one order of magnitude above those of the other transitions (J = 0, 1, 3 and 4). The spectrum collected for [Eu(tta)$_3$phen] well agrees with the reference from literature[25], analogously, the emission profile of [Eu$_2$(AFF)$_4$](NEt$_4$)$_2$ resembles that of previously characterized $Eu^{3+}$-based LOCs[19]. In particular, the fairly intense band corresponding to the $^5D_0 \rightarrow {}^7F_4$ transition suggests a square antiprismatic coordination geometry around the metal ion, in accordance with earlier structural characterizations carried out for other LOCs[19].

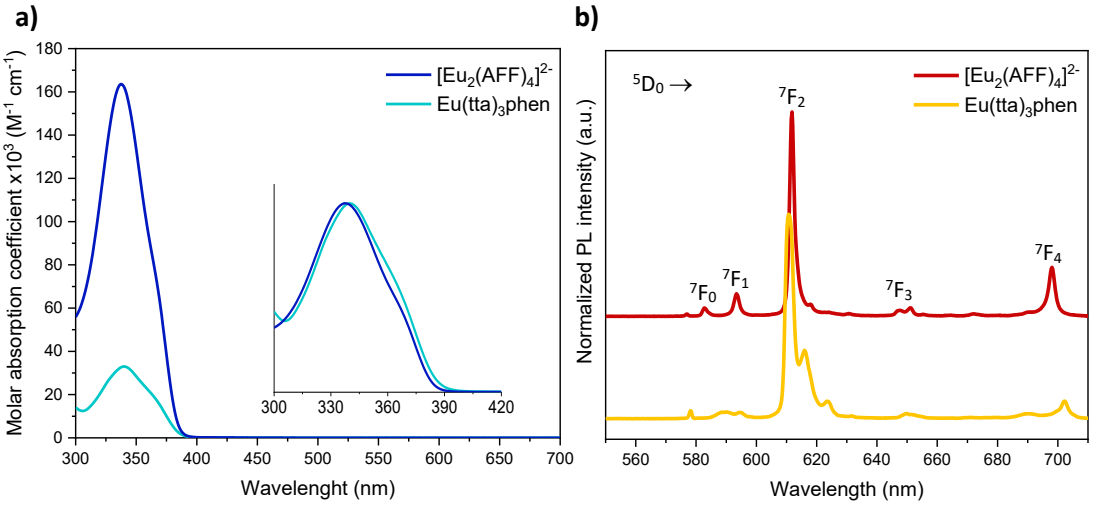


***Figure 2.16*** *a) UV/Vis absorption spectra (inset: normalized absorbance) and b) photoluminescence emission spectra (excitation wavelength $\lambda_{exc}$=340 nm) for [Eu(tta)$_3$phen] in $CHCl_3$ solution and for [Eu$_2$(AFF)$_4$](NEt$_4$)$_2$ in $CHCl_3$/THF 1:1 solution.*

Excited state $^5D_0$ lifetimes and photoluminescence quantum yields were also measured for both luminophores, obtained experimental values are summarized in Table 2.1, along with calculated brightness values. Comparing this last parameter between the two luminophores, the [Eu$_2$(AFF)$_4$](NEt$_4$)$_2$ cage shows greatly enhanced values with respect to the benchmark, which can be mainly ascribed to its larger molar absorptivity since the little difference in the respective PLQYs. Having assessed this preliminary relationship between the photophysical properties of the two luminophores will prove useful to determine if the same are retained in moving from a diluted solution to a solid medium environment, as would be desirable for obtaining highly luminescent waveguides containing the synthetized LOC.

Regarding ligands' triplet state energies, their evaluation was not carried out for the specific antenna systems here employed since already reported in other studies. Estimated values based on already existing data are reported in Table 2.1. In the case

of [Eu(tta)$_3$phen], literature assessments on the triplet state energy of thenoyltrifluoracetate slightly differ from one another, so an interval of plausible values is provided[26,27]. Concerning [Eu$_2$(AFF)$_4$](NEt$_4$)$_2$, the $T_1$ energy determined for DPA in previous studies[28] can be considered valid with good approximation also for AFF, because of the very limited change in the ligand structure. That said, for both complexes the energy gap between the ligand $T_1$ state and europium(III) $^5D_0$ emitting state (17227 cm$^{-1}$) is wide enough (> 1850 cm$^{-1}$) to ensure an efficient sensitization of the lanthanide.

***Table 2.1*** *Excited state lifetime (τ), PLQY, molar absorptivity ($\varepsilon_{max}$), brightness (B) and triplet energy state ($E_{T1}$) values for studied luminophores. All solutions for photophysical characterizations were employed with a molar concentration of $10^{-5}$.*

| ***Compound*** | *τ (ms)* | *PLQY (%)* | *$\varepsilon_{max} \cdot 10^5$ ($M^{-1}$ $cm^{-1}$)* | *B ($M^{-1}$ $cm^{-1}$)* | *$E_{T1}$ ($cm^{-1}$)* |
|---|---|---|---|---|---|
| **[Eu$_2$(AFF)$_4$](NEt$_4$)$_2$** | 1.00 | 66 | 1.63 | 107580 | 20900 |
| **[Eu(tta)$_3$phen]** | 0.64 | 60 | 0.33 | 19800 | 19300 – 21300 |

## 2.5. References


1. Werts, M. H. V. Making sense of lanthanide luminescence. *Sci. Prog.* **88**, 101–131 (2005).
2. Cotton, S. *Lanthanide and Actinide Chemistry*. (John Wiley & Sons, Ltd, 2006).
3. Sorace, L. & Gatteschi, D. Electronic Structure and Magnetic Properties of Lanthanide Molecular Complexes. in *Lanthanides and Actinides in Molecular Magnetism* **2,** 1–26 (Wiley-VCH Verlag GmbH & Co. KGaA, 2015).
4. Kettle, S. F. A. *Physical Inorganic Chemistry A Coordination Chemistry Approach*. **59** (Springer-Verlag Berlin Heidelberg GmbH, 1996).
5. Wang, R. & Zhang, F. *Infrared Nanomaterials for Bioimaging*. *Near Infrared Nanomaterials: Preparation, Bioimaging and Therapy Applications* (The Royal Society of Chemistry, 2016).

6. Gorller-Walrand, C. & Binnemans, K. Spectral intensities of f-f transitions. in *Handbook on the Physics and Chemistry of Rare Earths* **25**, 101–264 (Elsevier Science B.V, 1998).
7. Binnemans, K. Interpretation of europium(III) spectra. *Coord. Chem. Rev.* **295**, 1–45 (2015).
8. Weissman, S. I. Intramolecular energy transfer. The fluorescence of complexes of Europium. *J. Chem. Phys.* **10**, 214–217 (1942).
9. Crosby, G. A., Whan, R. E. & Alire, R. M. Intramolecular energy transfer in rare earth chelates. Role of the triplet state. *J. Chem. Phys.* **34**, 743–748 (1961).
10. De Mello Donegá, C., Ribeiro, S. J. L., Gonçalves, R. R. & Blasse, G. Luminescence and non-radiative processes in lanthanide squarate hydrates. *J. Phys. Chem. Solids* **57**, 1727–1734 (1996).
11. G.F. de Sà. O.L. Malta, C. de Mello Donegà, A.M. Simas, R.L. Longo, P.A. Santa-Cruz, E. F. da S. J. Spectroscopic properties and design of highly luminescent lanthanide coordination complexes. *Coord. Chem. Rev.* **196**, 165–195 (2000).
12. Latva, M. *et al.* Correlation between the lowest triplet state energy level of the ligand and lanthanide(III) luminescence quantum yield. *J. Lumin.* **75**, 149–169 (1997).
13. Armelao, L. *et al.* Design of luminescent lanthanide complexes: From molecules to highly efficient photo-emitting materials. *Coord. Chem. Rev.* **254**, 487–505 (2010).
14. Bünzli, J. C. G. & Piguet, C. Taking advantage of luminescent lanthanide ions. *Chem. Soc. Rev.* **34**, 1048–1077 (2005).
15. Nehra, K., Dalal, A., Hooda, A., Bhagwan, S. & Kumar, R. Lanthanides β-diketonate complexes as energy-efficient emissive materials: A review. *J. Mol. Struct.* **1249**, 1–24 (2022).
16. Li, H. F., Li, G. M., Chen, P., Sun, W. Bin & Yan, P. F. Highly luminescent lanthanide complexes with novel bis-β-diketone ligand: Synthesis, characterization and photoluminescent properties. *Spectrochim. Acta - Part A Mol. Biomol. Spectrosc.* **97**, 197–201 (2012).
17. Yang, C. *et al.* The effect of two additional Eu3+ lumophors in two novel trinuclear europium complexes on their photoluminescent properties. *Photochem. Photobiol. Sci.* **12**, 330–338 (2013).

18. Rancan, M. *et al.* Dynamic lanthanides exchange between quadruple-stranded cages: effect of ionic radius differences on kinetics and thermodynamics. *Inorg. Chem. Front.* (2022) Advance article.
19. Rancan, M. *et al.* Adaptive helicity and chiral recognition in bright europium quadruple-stranded helicates induced by host-guest interaction. *Cell Reports Phys. Sci.* **3**, 100692 (2022).
20. Lima, P. P. *et al.* Spectroscopic study of a UV-photostable organic-inorganic hybrids incorporating an Eu3+ β-diketonate complex. *ChemPhysChem* **7**, 735–746 (2006).
21. Zhao, S., Zhang, L., Li, W. & Li, L. Preparation and fluorescent property of Eu(TTA)3phen incorporated in polycarbonate resin. *Polym. J.* **38**, 523–526 (2006).
22. Tonezzer, M. *et al.* Luminescent solar concentrators employing new Eu (TTA)3phen-containing parylene film. *Prog. Photovoltaics Res. Appl.* **20**, 6–11 (2015).
23. Shahi, P. K., Singh, A. K., Singh, S. K., Rai, S. B. & Ullrich, B. Revelation of the Technological Versatility of the Eu(TTA)3Phen Complex by Demonstrating Energy Harvesting, Ultraviolet Light Detection, Temperature Sensing, and Laser Applications. *ACS Appl. Mater. Interfaces* **7**, 18231–18239 (2015).
24. Bauer, H., Blanc, J. & Ross, D. L. Octacoordinate Chelates of Lanthanides. Two Series of Compounds. *J. Am. Chem. Soc.* **86**, 5125–5131 (1964).
25. Freund, C. *et al.* Thiophene based europium β-diketonate complexes: Effect of the ligand structure on the emission quantum yield. *Inorg. Chem.* **50**, 5417–5429 (2011).
26. Malta, O. L. *et al.* Spectroscopic properties of a new light-converting device Eu(thenoyltrifluoroacetonate)3 2(dibenzyl sulfoxide). A theoretical analysis based on structural data obtained from a sparkle model. *J. Lumin.* **75**, 255–268 (1997).
27. Varaksina, E. A. *et al.* Tuning the luminescence efficiency by perfluorination of side chains in Eu3+complexes with β-diketones of the thiophene series. *Phys. Chem. Chem. Phys.* **23**, 25748–25760 (2021).
28. Carlotto, A. Tesi di Dottorato. (Università degli Studi di Padova, 2021).

# Chapter 3

# Preparation of LSC waveguides

In this Chapter, the methods adopted for the realization of polymeric LSC waveguides will be described, focusing on the progress in their fabrication. A first account on the processing of matrices will be provided, followed by the study of luminophores incorporation and its optimization. Structural (powder XRD) and thermal (TGA, DSC) analyses were carried out to gain insights into the effects that processing operations have on the materials. The absorption/emission properties of the obtained materials were assessed through UV/Vis absorption and photoluminescence spectroscopies, and then compared to those of the luminophores in solution.

## 3.1. Design of waveguide: shapes and materials

Among the various possible conformations for an LSC device, the classic embodiment sees the luminophore homogeneously dispersed inside the whole volume of the host medium, which is moulded in the form of a slab and acts as a waveguide. Another widely studied configuration consists in shaping the active material into a coating deposited onto an appropriate substrate, capable to waveguide the radiation emitted inside the supported active layer.

Both kinds of samples were realized in our study, using different polymers: polydimethylsiloxane (PDMS) was employed to cast bulk-doped tiles, while polymethylmethacrylate (PMMA) and polystyrene (PS) were used for casting films, both free-standing and supported on glass.

Polymer properties that are relevant to our study are listed in Table 3.1.

***Table 3.1*** *Average molecular weight (MW), glass-transition temperature ($T_g$), refraction index (n) and UV/Vis optical cut-off ($\lambda_{off}$) values for employed polymers. Unless otherwise cited, data are reported as declared by suppliers.*

| ***Compound*** | *MW (g/mol)* | *$T_g$ (°C)* | *n* | *$\lambda_{off}$ (nm)* |
|---|---|---|---|---|
| **PDMS** | n/a | $< -100$ [1] | 1.41 | 240 [2] |
| **PMMA** | 350 000 | 105 | 1.49 [1] | 330 [3] |
| **PS** | 280 000 | 100 | 1.59 [1] | 320 [4] |

Transmission profiles for mentioned materials are summarized in Fig. 3.1. It can be immediately noted that all matrices possess good transparency (T > 90%) in the visible region of the spectrum and for a further portion of the UV range. This factor assumes particular importance within the absorption wavelengths of the employed luminophores (300 – 380 nm, shaded area in Fig. 3.1), since absorption by the host medium in this interval should be as small as possible to ensure that the incident radiation is mainly harvested by the luminescent species. Considering mean transmittance values of 95% for PDMS and of 85% for PMMA and PS in the region of interest, all of the three materials should prove as good choices for realizing LSC waveguides embedded with [Eu(tta)$_3$phen] and [Eu$_2$(AFF)$_4$](NEt$_4$)$_2$.

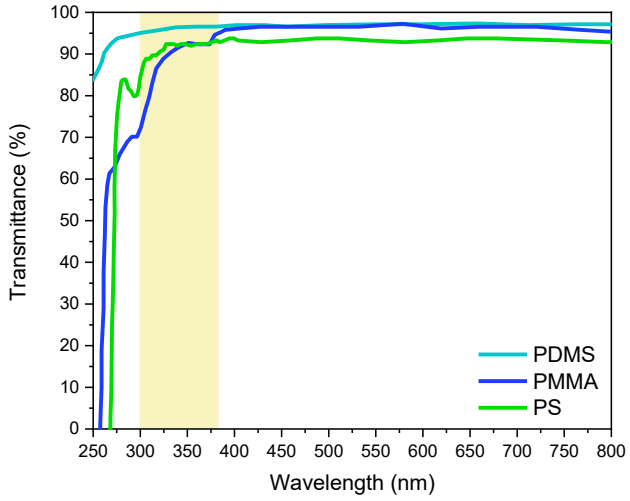


***Figure 3.1*** *Transmission curves for PDMS, PMMA and PS, with highlight of the employed luminophores absorption wavelengths (adapted from ref. 2-4).*

## 3.2. Description of fabrication methods

Before dealing with luminophore incorporation, it is crucial to learn how to efficiently process the host materials, and model them into the desired shape with high repeatability. Used casting procedures were initially adapted from reference ones[5] and successively optimized according to desired sample features.

**– PDMS tiles**

The most common casting protocol for PDMS involves the cross-linking of a siloxane elastomer (part A) by treatment with a curing agent (part B). Technical data and curing times provided in standard procedures usually refer to a mixing ratio A/B of 10:1, which was also used for our samples. Thorough blending of the two parts causes incorporation of air bubbles into the mixture, that needs degassing. This can be achieved by brief vacuum cycles or, as in this case, by centrifugation at low speeds (2000 – 3000 rpm) or by ultrasound sonication. The degassed mixture is then poured into a mould and left to cure until complete solidification, preferably in a dust-free environment to avoid incorporation of dirt into the polymer. Holed aluminium foil was employed to cover the casting moulds, protecting the samples from dust.

Curing can be conducted either at room or higher temperature, and curing times shorten accordingly. Samples left to cure in ambient conditions have been observed to solidify after 48 – 60 hours, while samples placed in oven at 60 °C took roughly half the time. No significant difference in the stiffness and surface texture was observed between samples cured at different temperatures.

Regarding employed tools, first castings were carried out using already available glassware that could be easily adapted as moulds, like Petri dishes. The obtained circular-shaped tiles were then cut in squared ones, but this resulted in highly irregular side surfaces due to the low precision in using a cutting knife on a rubbery material like PDMS (Fig. 3.2a). Hence, disposable moulds were built by craft means in a square shape, and yielded samples with smooth, scatter-free surfaces after careful disassembling of the frame (Fig. 3.2b). However, leaking of unsolidified elastomer from such moulds even prolongedly after casting presented a considerable issue in terms of control on the thickness of the final tile. Due to the extremely low shrinkage (< 2%) of the PDMS casting blend upon curing[6], in fact, thickness can be easily regulated just by varying the quantity of elastomer to employ, provided no leakage of the blend happens.

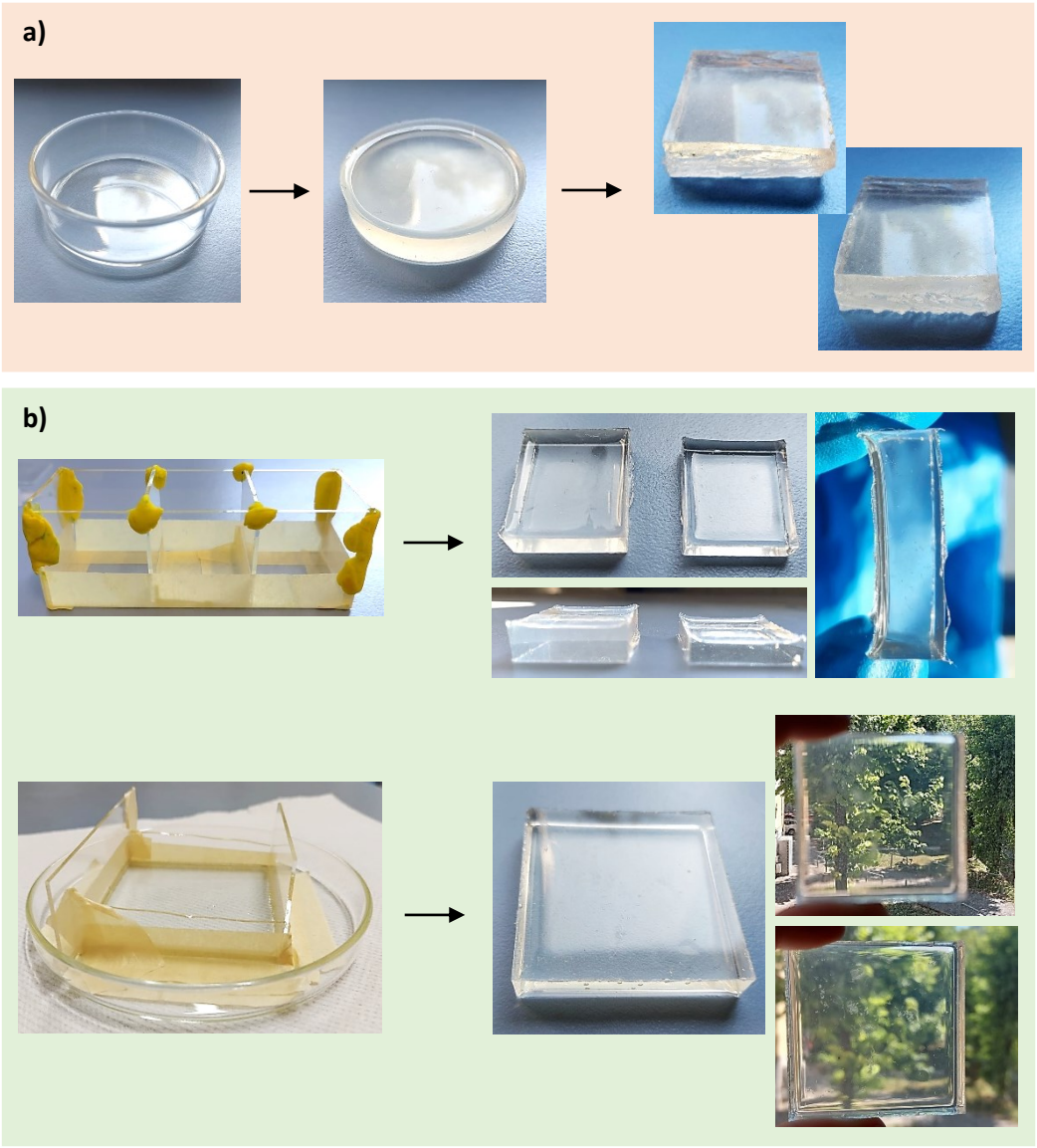


***Figure 3.2*** *Examples of moulds for PDMS tiles casting and corresponding samples: a) Petri dish, b) disposable square moulds built with microscope slides, tape and plasticine.*

A further mould, of 5.0 x 5.0 $cm^2$ internal area, was then appositely designed and built from polyether ether ketone (PEEK), a high-performing thermoplastic having optimal resistance to a wide range of solvents[7] (Fig. 3.3). Screwable joints assured tightness of the structure, while allowing easy extraction of the sample by detaching the side walls from the mould base. Using this mould, last realized samples showed optimal surface smoothness and transparency, comparable to that obtained with previous craft moulds. Absence of leakage offered the advantage of a higher control on sample thickness, down to the millimetre. Definition of the edges was also superior, resulting in tiles with neatly cut borders. Another important factor influencing the procedure outcome was the inclination of the surface where the mould was placed. Accurate levelling of

the mould prior to casting resulted in tiles with homogeneous height throughout the whole sample.

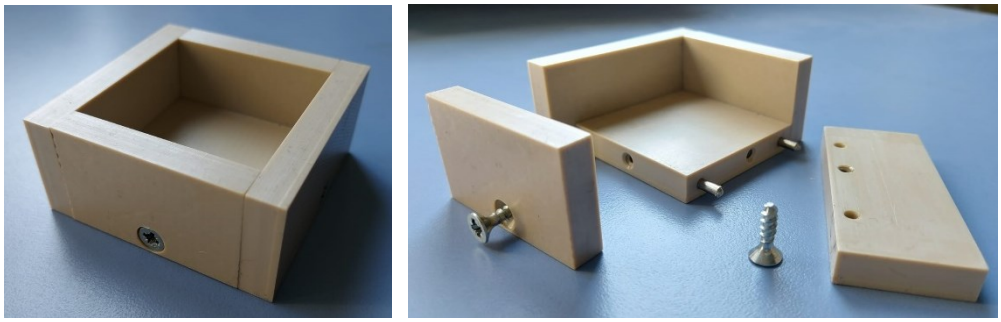

***Figure 3.3*** *PEEK casting mould with demountable side walls.*

**– PMMA and PS films**

Polymer films can be prepared by a wide variety of methods, among them, a solution casting technique was adopted to manufacture our PMMA and PS samples[8].

The general procedure consists in dissolving the polymer in an appropriate solvent, pouring the obtained solution onto a substrate of suitable shape, and letting the solvent evaporate to yield a solid polymeric layer which, depending on several adjustable parameters, can remain adhered to the underlying material or come off of it as a free-standing film. To our purpose, glass plates of 5.0 x 5.0 $cm^2$ top area and 0.3 cm thickness were employed as substrates.

The first object of study was the density to be employed for the casting solutions, because it determines how well the mixture spreads on the substrate and how easily it can be handled during casting operations. A series of solutions at different weight concentrations in PMMA and in PS was then tested to assess the best polymer to solvent ratio to employ. Chloroform and toluene were chosen as solvents, due to their optimal compatibility with PMMA and PS, respectively. Dissolution of the polymers required heating under constant stirring: exercised temperatures were kept in the range of 60 – 70 °C, in order to work well below the glass-transition temperatures of the polymers. Weight concentrations of 25% of PMMA in chloroform and 32% of PS in toluene were reached before observing formation of polymer clumps adhered to the bottom and walls of the vessel. Such solutions were too viscous to homogenously spread on the substrate, producing polymeric patches with limited extension and irregular thickness, which also retained trapped air bubbles (Fig 3.4).

***Figure 3.4*** *PMMA (left) and PS (right) castings from highly concentrated solutions on 5.0 x 5.0 cm$^2$ glass slides.*

The tested concentrations were then lowered, until a good compromise between solution viscosity and volume needed to cover the whole glass surface was reached. Viable mass to volume concentrations ranged from 125 to 250 mg/mL, meaning weight concentrations of 7% – 14% for solutions in chloroform, and of 13% – 22% for those in toluene. Thus, the amount of polymer to employ for each casting was fixed at the value of 0.500 g, to reduce the number of variables at play and focus on the optimization of other parameters.

First castings were carried out using crafted moulds similar to those employed for PDMS, made with a 5.0 x 5.0 cm$^2$ glass plate as base and a surrounding glass frame. The solution was poured from the vessel directly onto the plate, starting from the centre and gradually covering the external regions, until a homogeneous liquid layer was obtained. Produced films presented jagged edges that caused loss of adherence to the substrate, and eventually led to complete detachment from the glass surface. This was probably due to the fact that the solution formed a concave meniscus with the walls of the mould, which caused part of the polymer to stick to the frame upon evaporation of the solvent, producing raised borders. Films of regular shape could still be obtained by cutting away the edges, however, it would be preferable to avoid this additional step by achieving already well-defined boundaries. Besides, leakage issues of the moulds were encountered once more, so further procedure improvement was studied to limit material waste and to increase casting repeatability.

Hence, the frame element of the moulds was removed, and new castings were carried out on the sole glass plates, paying particular attention not to spill the solution off the slab's edges. Levelling of the glass surface was even more crucial for this kind of procedure with respect to PDMS casting, since inclinations of less than one degree were enough for the solution to flow towards the lower region of the substrate and

eventually spill over it. Slips of paper were sufficient to compensate for the little unevenness of the countertops (Fig. 3.5).

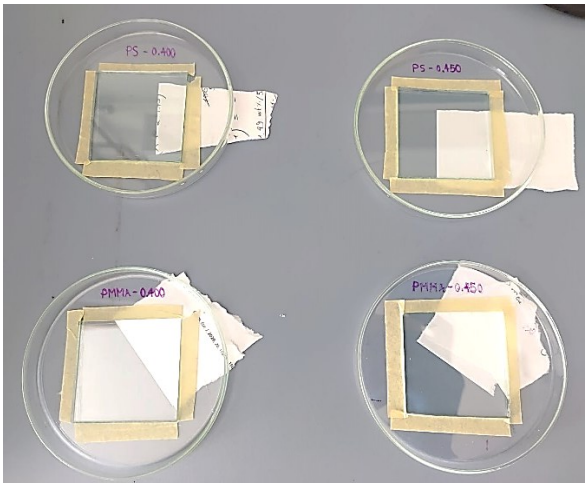


***Figure 3.5*** *Glass plates set for film casting, levelled with slips of paper.*

Drying conditions were progressively adjusted to obtain smooth, flat films: a general indication for achieving high surface homogeneity through solution casting is to slow down evaporation of the solvent. It has been observed that letting casted samples dry under the fume hood caused the solvent to leave the solution too fast and in a non-uniform way, resulting in pronounced bending of the film and corrugation of its surface. Films dried at ambient conditions, covered with holed aluminium foil to avoid dust deposition, presented instead the desired surface homogeneity. Estimated drying times ranged from 12 to 15 hours.

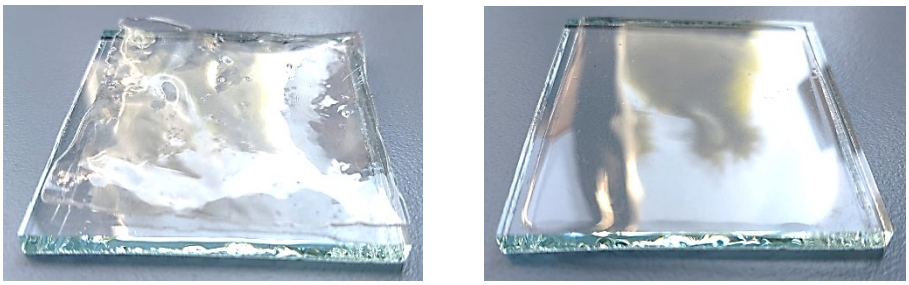

***Figure 3.6*** *5.0 x 5.0 cm$^2$ PMMA films dried under the fume hood (left) and at ambient conditions (right).*

However, several PS castings from toluene showed condensed solvent droplets on the aluminium coverage, which eventually fell back onto the half-solidified film producing slightly corrugated surfaces. One way to avoid this from happening was to periodically monitor the state of the sample and remove any observed condensate, but this expedient resulted often impractical, due to the drying process being mainly conducted overnight. Chloroform was then tested as a casting solvent also for PS,

showing good compatibility with the polymer and resolving the issue of solvent condensation, probably due to its higher vapour pressure with respect to toluene. For an optimal handling of the solution, its viscosity had to be adjusted by decreasing the volume of employed solvent (see Table 3.2).

Although being solid, all the realized films retained great flexibility, which is mainly ascribable to the presence of a significant residual solvent fraction trapped inside the final product (see paragraph 3.4, "Thermal analyses").

The described method is suitable to realize self-supporting films of considerable thickness, on the order of few hundreds of micrometres. After several optimization steps, the amounts of casting materials listed in Table 3.2 were found effective to achieve a film thickness of 200 μm with optimal repeatability between samples (standard deviation = 7.5 μm). Measurements were taken with a calibre along several sections of the films surface, and thickness values are given as a mean on such samplings. For films realized with the optimized procedure, inhomogeneity in the thickness throughout the same sample has been determined to be 5% at most. On the other hand, no dimensional control comparable to that on PDMS tiles thickness was achieved for PMMA and PS films, due to the substantially higher complexity of the studied system.

***Table 3.2*** *Optimized quantities for achieving homogeneous 5.0 x 5.0 cm$^2$ films of 200 μm average thickness.*

| ***Polymer/solvent*** | *m (g)* | *V (mL)* | *w/w (%)* |
|---|---|---|---|
| **PMMA/$CHCl_3$** | 0.500 | 3.5 – 4.0 | 8.7 – 7.7 |
| **PS/$CHCl_3$** | 0.500 | 3.0 | 16.1 |
| **PS/toluene** | 0.500 | 3.5 | 14.1 |

Having designed a viable method to obtain free-standing polymeric films, this was further developed within the goal of obtaining glass supported films. In order to avoid detachment from the substrate, the glass plates were pre-treated with a ~ 6 M aqueous hydrochloric acid solution[9]. The difference with respect to the untreated slabs was already apparent during casting operations, as the solution droplets deposited on the substrate possessed lower contact angle and less mobility on the glass surface, making the casting itself more manageable. The majority of this batch of samples was obtained

with 200 μm thickness, as desired, while a small number of castings suffered from accidental errors that produced thinner films (100 to 150 μm). Optimal adhesion between polymeric films and glass was observed at first, but after three to four weeks from casting partial detachment was observed for the 200 μm samples, which was probably caused by a gradual release in time of the trapped solvent (Fig. 3.7). Furthermore, the loss of adherence was noticed to happen sooner for the PS samples than for the PMMA ones. Thinner films instead showed no significant changes during the same timeframe, retaining the initial appearance (Fig. 3.8).

Since there has been no chance of investigating more deeply this last aspect during the project, further development of research will surely have to address the dependence of detachment on the film thickness, as well as the kinetics of solvent evaporation, possibly in variable temperature conditions.

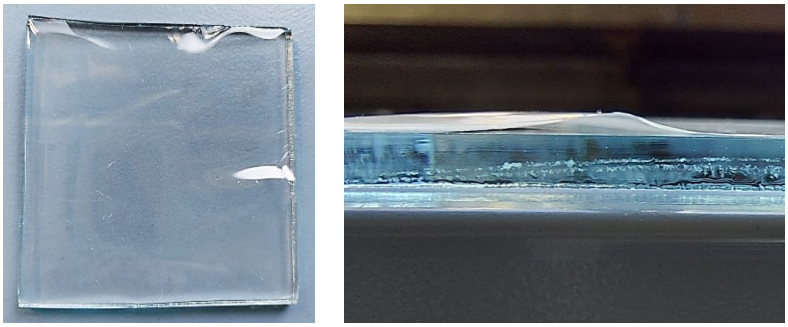

***Figure 3.7*** *PMMA film of ~ 200 μm thickness, casted onto treated 5.0 x 5.0 $cm^2$ glass slides and showing first signs of adherence loss around the perimeter, with close-up of a detached portion.*

***Figure 3.8*** *PMMA film of ~ 130 μm thickness, casted onto a 5.0 x 5.0 $cm^2$ treated glass slide and retaining initial adherence.*

## 3.3. Luminophore embedding

Using the developed casting methods, luminescent polymeric waveguides were realized embedding [Eu(tta)$_3$phen] and [Eu$_2$(AFF)$_4$](NEt$_4$)$_2$ as active components. The study of luminophores incorporation focused on their compatibility with casting solutions and on their solubility into the host materials.

The choice of a suitable solvent for both the complex and the matrix was of paramount importance to maintain the homogeneity of the casting solution. Solubility of the luminophores into chloroform and toluene was tested, due to their use as solvents for PMMA and PS castings. Tetrahydrofuran was also found to be a valid solvent for luminophores solutions, while possessing acceptable compatibility with PMMA (up to 120 mg/mL) and PS (up to 140 mg/mL). All three solvent can also swell the PDMS two-parts mixture without altering its properties[10]. Maximum concentrations reached for luminophores solutions into mentioned solvents are listed in Table 3.3.

***Table 3.3*** *Maximum solubility assessed for the two $Eu^{3+}$ complexes in employed solvents, expressed in mg/mL.*

| ***Compound*** | *$CHCl_3$* | *toluene* | *THF* |
|---|---|---|---|
| **[Eu(tta)$_3$phen]** | 6 | 8 | 4 |
| **[Eu$_2$(AFF)$_4$](NEt$_4$)$_2$** | 1 | < 1 | 4 |

In adding [Eu(tta)$_3$phen] to PDMS, the minimum quantity of solvent necessary to dissolve the complex was used in order to not affect the curing process. Curing times stayed virtually the same as for undoped samples, yet the adopted thermal treatment was seen to affect the final surfaces texture. Samples cured at 60 °C for 24 hours presented dry surfaces, while those left at ambient conditions remained damp to the touch, probably due to residual solvent traces, and had to be post-cured at 60 °C to complete evaporation. PDMS luminescent samples containing [Eu(tta)$_3$phen] in concentration of 0.03% with respect to the mass of employed polymer were initially prepared. Despite complete dissolution of the complex in the mediating solvent, the final tiles showed luminophore segregation inside the polymer matrix. Optimized dopant concentrations yielding homogeneous, transparent samples were later assessed to be in the range of 0.003% to 0.008% (Fig. 3.9).

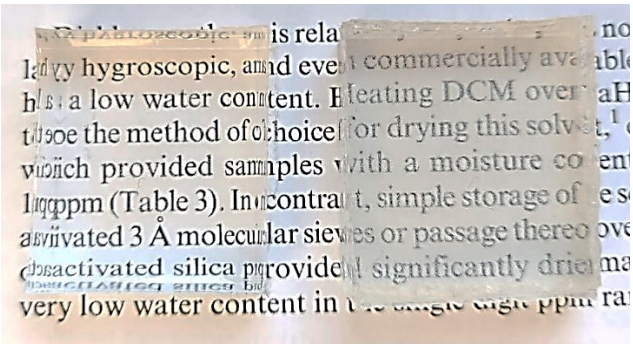

***Figure 3.9*** *2.5 x 2.5 x 1.0 cm³ PDMS tiles containing [Eu(tta)₃phen] at the 0.003% (left) and at the 0.03% (right) by weight, exhibiting different degrees of transparency.*

Regarding PMMA and PS solutions, incorporation of [Eu(tta)$_3$phen] was straightforward, thanks to its appreciable solubility in toluene and chloroform. To add the luminophore, it was sufficient to introduce it into a polymer solution prepared as described in the previous Paragraph, without adding extra solvent. Although dissolving the complex in this way is not immediate, it was anyway preferable to add the luminophore to the polymer solution, and not the other way around, to avoid eventual precipitation of the complex due to a considerable addition of polymer. The 200 μm thick films have been observed to tolerate [Eu(tta)$_3$phen] weight concentrations up to 1% before showing segregation of the complex, with consequent loss of surface smoothness and structural integrity (Fig 3.10).

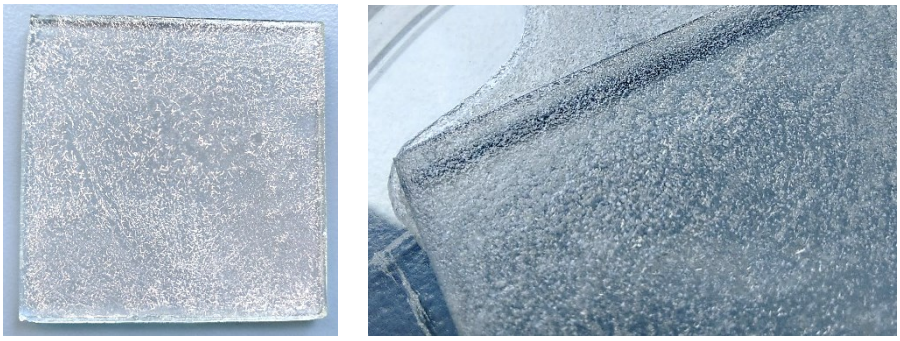

***Figure 3.10*** *Full image (left) and close-up (right) of a 5.0 x 5.0 cm² PMMA film containing [Eu(tta)₃phen] at the 4.0% by weight.*

Incorporation of [Eu$_2$(AFF)$_4$](NEt$_4$)$_2$ into PMMA was also achieved, realizing samples at 0.9% in weight. This concentration corresponds to a Eu(III) molar content equal to that of films at 0.5% in weight of [Eu(tta)$_3$phen], and was purposedly adopted to compare the two luminophores during characterizations. Because of the lower solubility of the cage in chloroform, the employed solvent for the casting solution was a chloroform/tetrahydrofuran 1:1 mixture. Drying after casting was observed to happen faster for this solution with respect to those previously tested (pure toluene and

pure chloroform), presenting again surface corrugation issues. Evaporation was then further slowed down by placing a more sealing cover above the coated glass slab; simple pieces of glassware, such as a flipped Petri dish or funnel, sufficed to this purpose. Embedding of the cage in PS was attempted, but it did not produce samples with acceptable optical quality, due to partial luminophore segregation and solvent evaporation, which still caused bending of the film.

All samples containing [Eu(tta)$_3$phen], both tiles and films, showed the characteristic red emission of europium(III) under UV illumination at 365 nm, while the PMMA film containing [Eu$_2$(AFF)$_4$](NEt$_4$)$_2$ appeared pink (Fig. 3.11 and 3.12). Appreciable luminescence of the [Eu(tta)$_3$phen]-doped films was observed also in natural light conditions (Fig. 3.13).

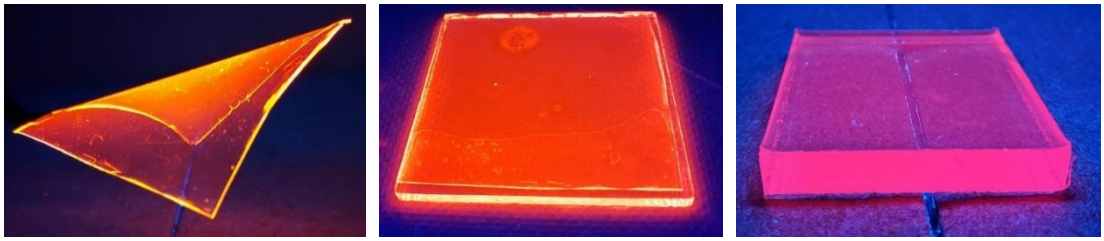

***Figure 3.11*** *Collection of samples containing [Eu(tta)$_3$phen] under UV illumination at 365 nm: 5.0 x 5.0 cm$^2$ films in PMMA doped at the 0.4% (left and centre) and 5.0 x 5.0 x 0.8 cm$^3$ PDMS tile doped at the 0.008% (right).*

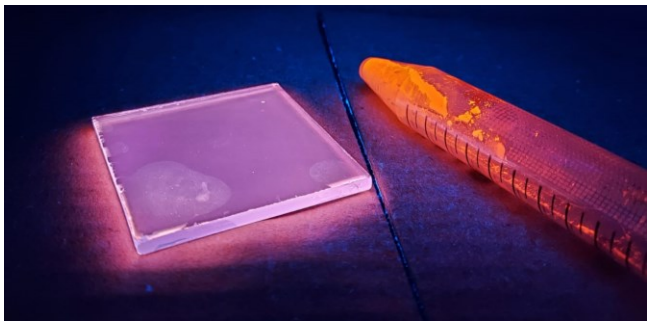

***Figure 3.12*** *5.0 x 5.0 cm$^2$ PMMA film containing [Eu$_2$(AFF)$_4$](NEt$_4$)$_2$ at the 0.9% by weight, showing anomalous pink emission under UV illumination at 365 nm (left), and red-emitting solid state sample of the same complex (right).*

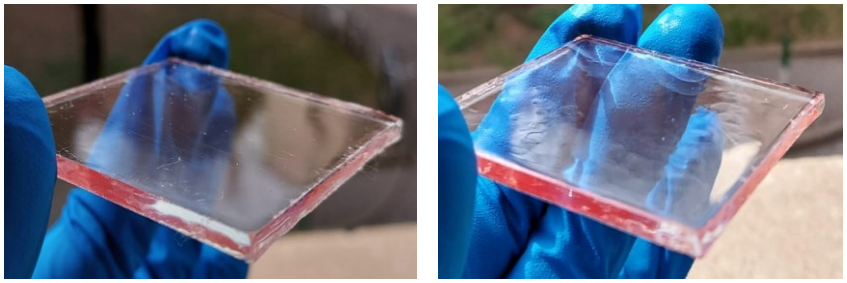

***Figure 3.13*** *5.0 x 5.0 cm$^2$ PMMA (left) and PS (right) films containing [Eu(tta)$_3$phen] at the 0.4% by weight under sunlight.*

## 3.4. Characterization of PMMA and PS waveguides

Characterized polymeric film samples containing the luminophores will be labelled according with a XX.YY.EuL nomenclature, where:

XX is an abbreviation for the polymeric matrix (PM = polymethylmethacrylate, PS = polystyrene);

YY is a two-digit abbreviation for the weight concentration of the luminophore inside the matrix (example: 10 = 1.0%, 05 = 0.5%);

EuL indicates the embedded complex, with L being the acronym for the specific β-diketone ligand (EuTTA = $[Eu(tta)_3phen]$, EuAFF = $[Eu_2(AFF)_4](NEt_4)_2$ ).

### 3.4.1. Powder X-ray diffraction

Films casted from pure PMMA and PS solutions were characterized with powder X-ray diffraction to assess if processing of the polymers affected in any way their structure. The diffraction patterns of amorphous materials such as the employed polymers are expected to exhibit broadened bands, covering several diffraction angles, rather than narrow peaks. The eventual presence of the latter would mean that partial crystallization of the matrix happened at some point during the casting procedure.

Fig. 3.14 shows the XRD patterns collected for pure PMMA and PS films, along with those of samples doped with $[Eu(tta)_3phen]$ at different concentrations. Diffractograms for the pure matrices show no sign of crystalline regions, and their shape well agrees with literature data[11,12]. The incorporation of the luminophore does not produce significant effects on the diffractograms. The absence of sharp signals in the patterns relative to the 4.0%-doped samples confirms that the loss of optical quality of such films is ascribable to the precipitation of the complex inside the polymeric matrix, and not to crystallization of the latter.

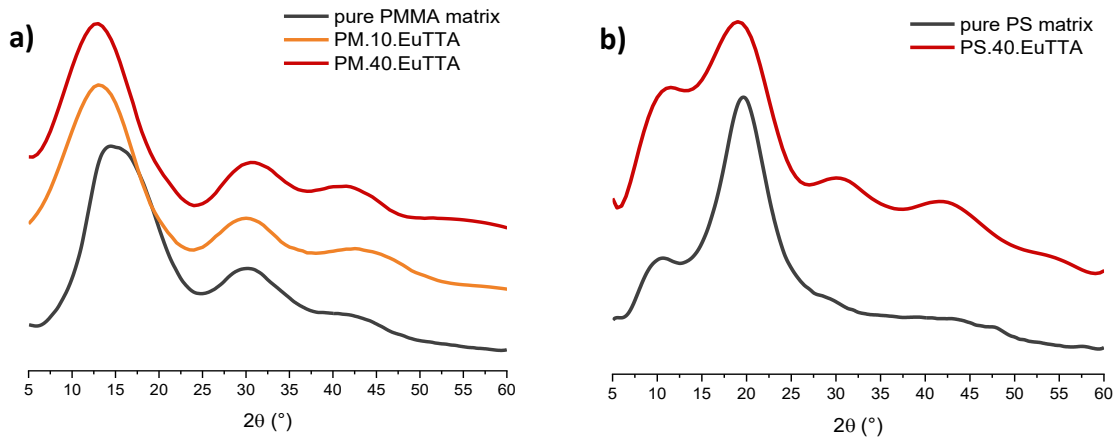


***Figure 3.14*** *Powder XRD diffractograms for pure matrices and samples with embedded [Eu(tta)₃phen] realized in a) PMMA and b) PS.*

## 3.4.2. Thermal analyses

Thermogravimetric analysis (TGA) and differential scanning calorimetry (DSC) were used to determine the percentage composition and the glass-transition temperature ($T_g$), respectively, for a series of PMMA and PS films casted from chloroform solutions. Analysed samples consisted in:

- pristine polymer, prior to any processing;
- casted matrix in the absence of luminophore;
- casted matrix containing [Eu(tta)$_3$phen] at 1.0% by weight;
- casted matrix containing [Eu(tta)$_3$phen] at 4.0% by weight.

From the TGA plots (Fig. 3.15a and 3.15c) it can be clearly seen that the films retain large fractions of solvent, which completely leaves the matrix at around 150°C for PMMA samples and at 140°C for PS ones. The percentage by weight of residual solvent ($CHCl_3$) is slightly different for the two polymers: it reaches 15% in the case of PMMA, and 10% for PS films. These two points of discrepancy suggest that the two matrices have different specific interactions with the solvent and that PMMA establishes more favourable ones, which determine a more delayed release of chloroform with the rising temperature and a more moderate evaporation of it after casting. All samples were analysed one month after fabrication, except for PS.10.EuTTA, which was made two weeks later than the others and thus analysed after a shorter time interval. Consequently, among PS samples PS.10.EuTTA shows the highest residual solvent amount, comparable to that of PMMA samples. This finding

provides a general indication on the time scale of the evaporation process, and may serve as a starting point for further investigations into such aspect. Complete degradation of the materials falls at temperatures far higher than those of solvent expulsion, therefore it is little affected by the starting composition of the film and, within each set of samples, it does not undergo significant variations. Calculated first derivatives of the TGA plots are reported in Fig. 3.15b and 3.15d and show two distinct peaks for processed samples, corresponding to the temperatures of solvent release (first peak, $T_{solv}$) and material degradation (second peak, $T_{mat}$); specific temperature values are given within the plots.

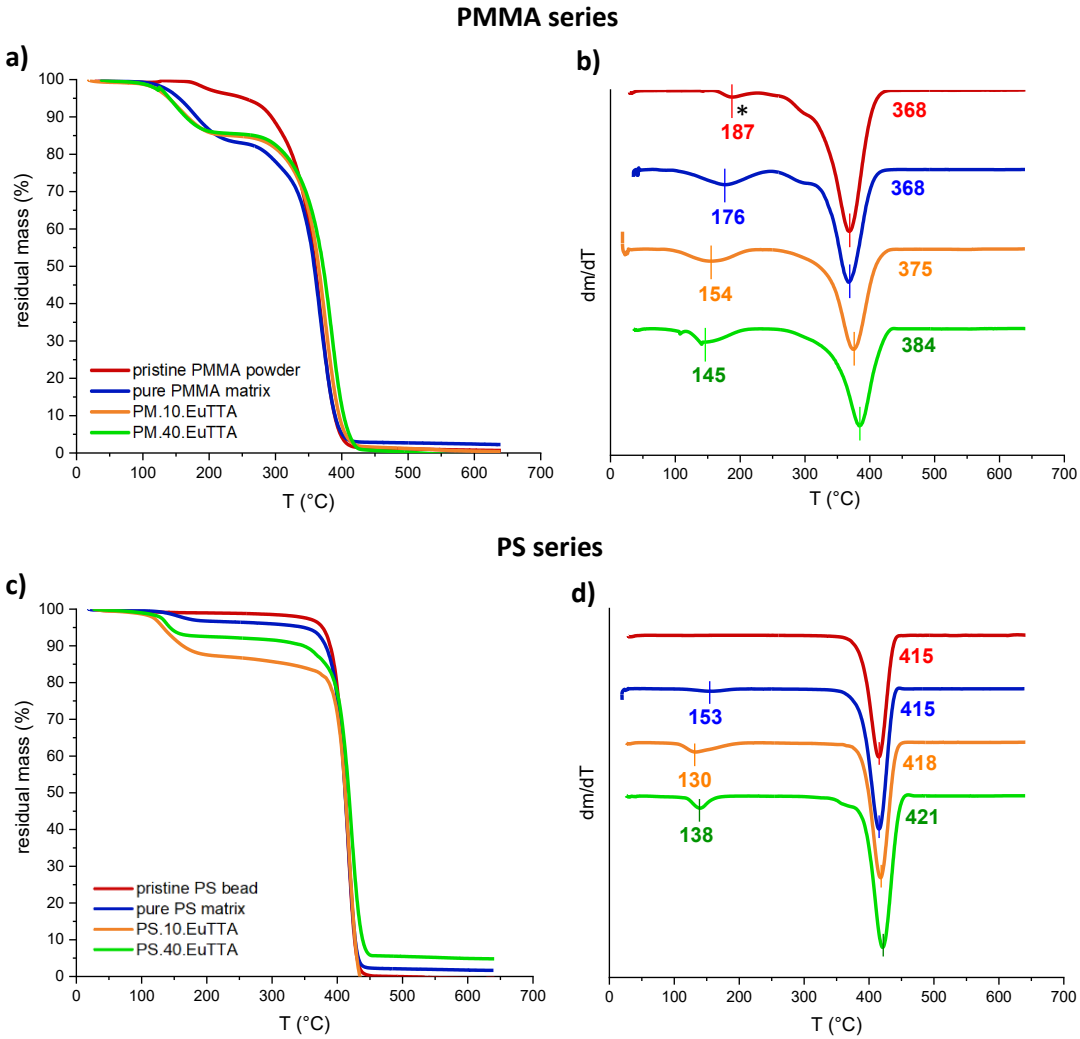


***Figure 3.15*** *TGA plots and calculated first derivatives for two analogous series of samples realized in PMMA (up) and in PS (down). Indicated $T_{solv}$ and $T_{mat}$ values are expressed in °C. *Peak ascribable to release of absorbed humidity by the PMMA powder.*

Moving on to DSC analyses, plots reported in Fig. 3.16 show significant decreases in the glass-transition temperatures of processed samples with respect to the pristine material, with variations on the order of 50°C. Such results can be interpreted on the

basis of TGA analyses: the solvent trapped inside the matrix can be seen as a plastic additive which lowers the material's $T_g$. Higher fractions of residual solvent determine higher glass-transition temperature variations, as is observed in the case of PS.10.EuTTA.

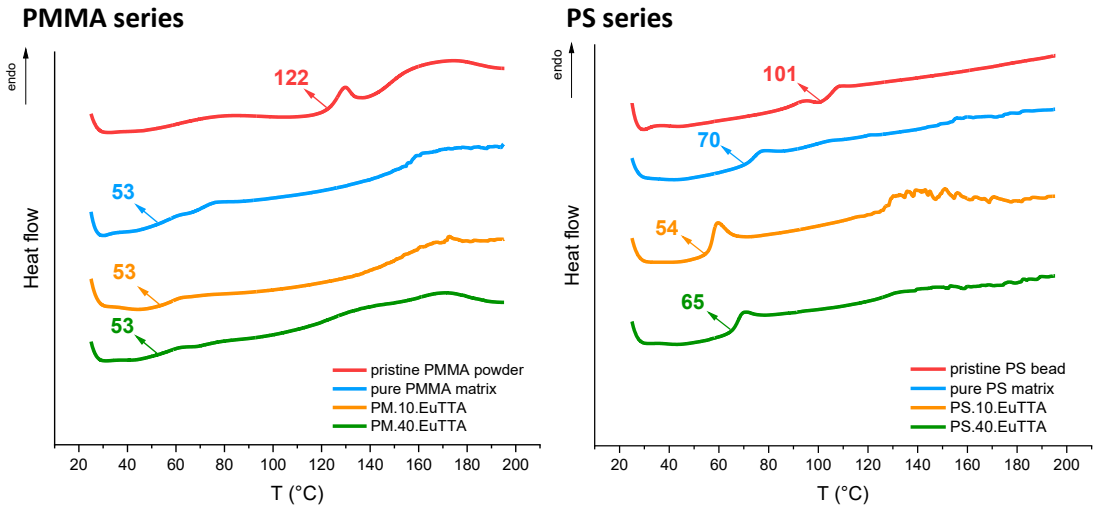


***Figure 3.16*** *DSC plots for two analogous series of samples realized in PMMA (left) and in PS (right). Indicated $T_g$ values are expressed in °C.*

## 3.4.3. Photophysical characterizations

Among realized samples, selected supported films (see Table 3.4) were characterized by UV/Vis absorption and photoluminescence spectroscopies.

***Table 3.4*** *Luminophore weight concentrations (w/w), $Eu^{3+}$ molar content ($n_{Eu}$) and film thickness (d) for characterized samples.*

| ***Sample name*** | *w/w (%)* | $n_{Eu}$ *(mol · $10^{-6}$)* | *d (μm)* |
|---|---|---|---|
| **PM.05.EuTTA** | 0.5 | 0.26 | 201 |
| **PM.10.EuTTA** | 1.0 | 4.9 | 202 |
| **PS.05.EuTTA** | 0.5 | 0.25 | 208 |
| **PS.10.EuTTA** | 1.0 | 5.0 | 125 |
| **PM.09.EuAFF** | 0.9 | 0.27 | 193 |

A first analysis of the absorption spectra related to [Eu(tta)$_3$phen] can be made by comparing samples fabricated with the same matrix but containing the luminophore at different concentrations (Fig. 3.17). The whole absorption profile could be detected for least concentrated samples, while the signals from the most concentrated ones gave instrument saturation. Absorption spectra of pure PMMA and PS films are also reported and exhibit optimal transparency of the matrices down to 300 nm. This confirms that, in the spectral region of interest, the absorption properties of the system are attributable to the luminophore only, without interference of the host materials.

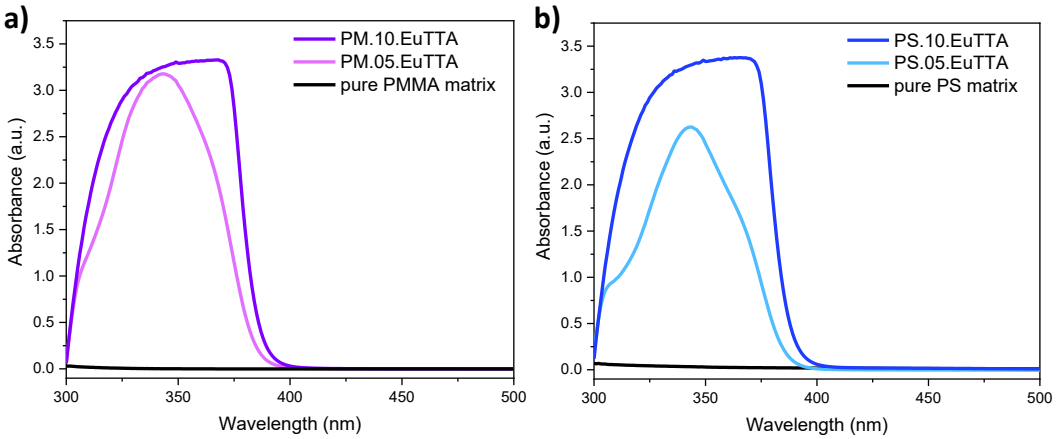


***Figure 3.17*** *UV/Vis absorption spectra recorded for two analogous series of film samples realized in a) PMMA and in b) PS.*

Fig. 3.18 shows the normalized absorption spectra in the UV region of 0.5%-doped samples and of [Eu(tta)$_3$phen] in solution. No remarkable differences can be observed between the spectra: band onsets and absorption maxima fall at the same wavelengths (or very close) both for the luminescent films and the solution, confirming that embedment and materials processing do not affect the absorption properties of [Eu(tta)$_3$phen].

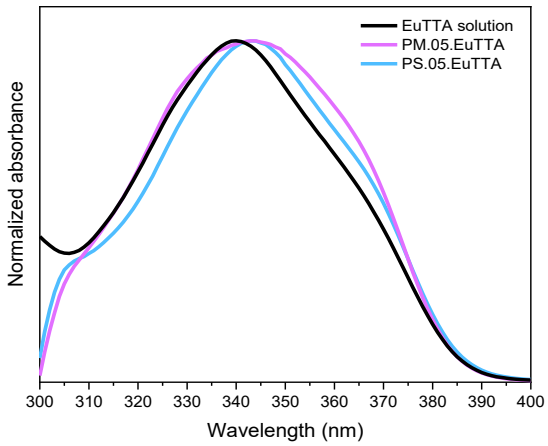


***Figure 3.18*** *Normalized absorbance overlay for samples of both polymeric matrices containing [Eu(tta)$_3$phen]at the same concentration, and for the same luminophore in solution.*

The absorption spectrum for PM.09.EuAFF was also collected and compared to that of PM.05.EuTTA, which possessed an equal $Eu^{3+}$ molar concentration (Fig. 3.19a). Based on the previously assessed relationship between the two luminophores' absorption properties in solution, the signal produced by the film containing the cage was expected to be far more intense than that of the $[Eu(tta)_3phen]$ reference, eventually exhibiting a saturated absorption profile. The absorbance recorded for such sample resulted instead very close to that of $[Eu(tta)_3phen]$, if not even lower. This marked discrepancy between $[Eu_2(AFF)_4](NEt_4)_2$ absorption in solution and in the polymer matrix is further confirmed by the comparison between the respective spectra (Fig. 3.19b). A significant red-shift is observed for the whole absorption band of the PMMA sample with respect to that of the cage in solution, suggesting that the luminophore does not retain the same absorption properties in passing from one chemical environment to the other.

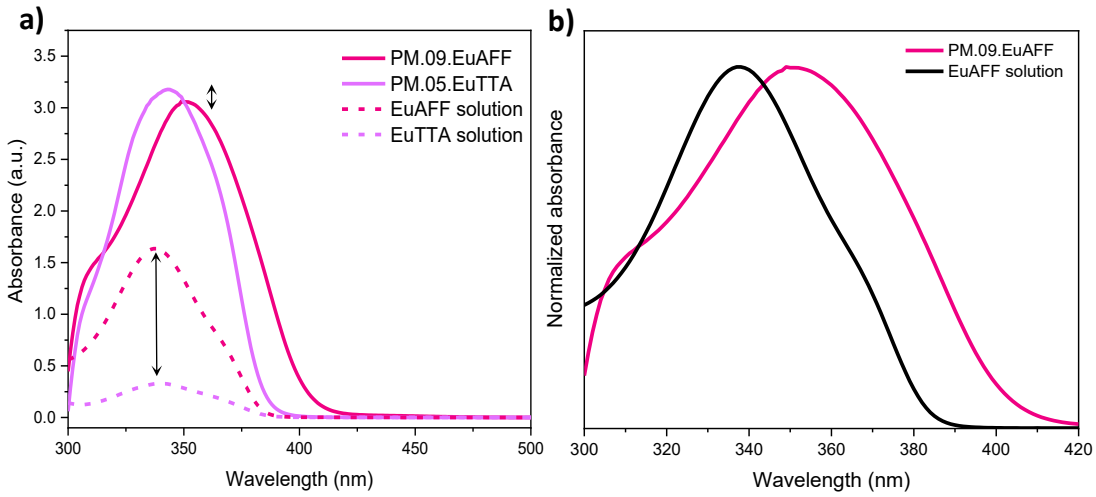


***Figure 3.19*** *a) UV/Vis absorption spectra of PM.09.EuAFF and the corresponding benchmark sample (solid lines), compared to those of the same luminophores in solution (dashed lines); b) normalized absorbance overlay for* $[Eu_2(AFF)_4](NEt_4)_2$ *in solution and in PMMA.*

Since variations of such entity were not observed in the case of $[Eu(tta)_3phen]$, it is fair to assume that the embedding process is not irrelevant from the point of view of $[Eu_2(AFF)_4](NEt_4)_2$, and that it affects the cage to a considerably greater extent than it does for the benchmark compound.

Further insight on this aspect can be gained from the photoluminescence spectra of the two species when incorporated in the polymeric host. The $Eu^{3+}$ ion can indeed act as a spectroscopic probe for investigating the structure of its immediate chemical surroundings[13]. It is often observed that different europium(III) complexes give rise to differently shaped emission spectra, depending on the geometry of the coordination

site binding the ion. Interpreting such variations is also facilitated in the case of $Eu^{3+}$ with respect to other lanthanoids, because of the relatively simpler electronic structure generated by the spin-orbit coupling. Both the ground state $^7F_0$ and the most important emitting excited state $^5D_0$ are in fact non-degenerate, meaning that they do not undergo splitting by the crystal-field effect. Furthermore, the most relevant transitions in europium(III) complexes luminescence spectra are those arising from the $^5D_0$ excited state towards the $^7F_J$ levels with low J values (J = 0, 1, 2), which also simplifies spectra interpretation due to the small number of accessible crystal-field states. To our purpose, the detection of variations in the relative intensities and shape of the $^5D_0 \rightarrow {}^7F_J$ (J = 0, 1, 2, 3, 4) multiplets between the spectrum of a luminophore in solution and in the host medium, indicates variations in the $Eu^{3+}$ coordination sphere. This would confirm that the embedment process induced a structural modification in the luminescent species, and specifically in the lanthanide coordination site.

We consider first the photoluminescence spectra of $[Eu(tta)_3phen]$ doped films (Fig. 3.20). The emission profiles of all four samples are superimposable to one another, and match with that collected for the luminophore in solution, meaning that the structure of the complex remains unchanged also upon embedding. At a closer examination, slight relative intensity variations can be detected between the emission spectra of the samples realized in PMMA and of those realized in PS, especially for the $^5D_0 \rightarrow {}^7F_2$ and the $^5D_0 \rightarrow {}^7F_4$ crystal-field progressions (Fig. 3.21). This suggests again that the two polymers establish different specific interactions with the luminescent species, which do not affect its structural integrity.

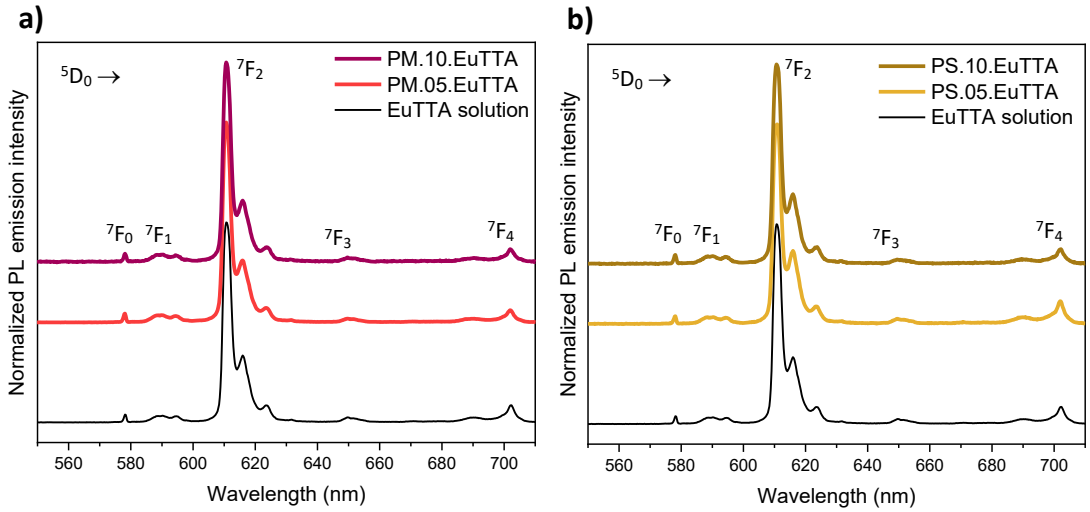


***Figure 3.20*** *Photoluminescence emission spectra (excitation wavelength $\lambda_{exc}$=340 nm) for films containing $[Eu(tta)_3phen]$ realized in a) PMMA and in b) PS, along with the luminophore emission profile in solution.*

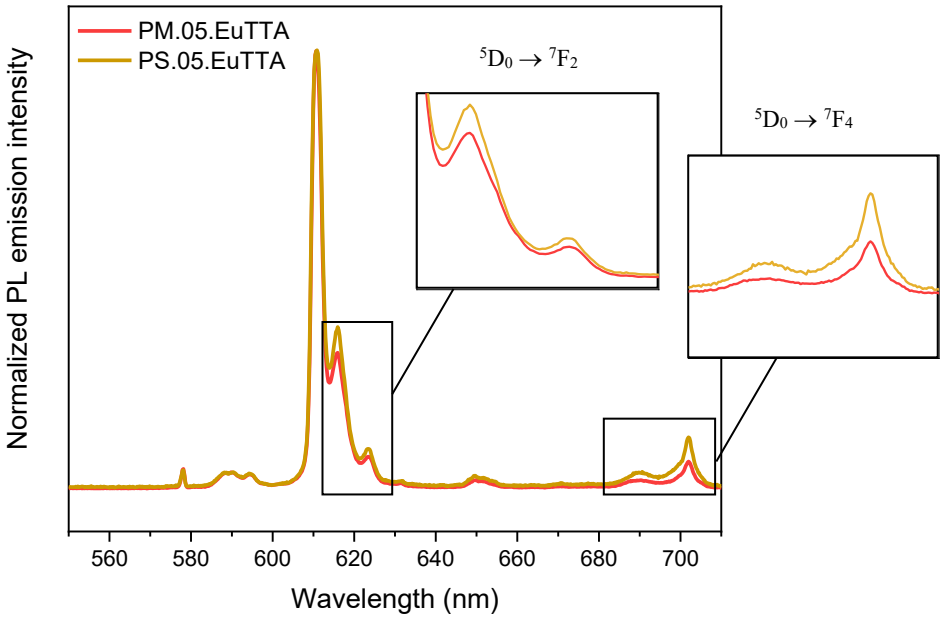


***Figure 3.21*** *Normalized PL emission overlay for samples of both polymeric matrices containing [Eu(tta)$_3$phen]. Insets: enlargements of the indicated crystal-field progressions.*

A totally different situation is found instead for $[Eu_2(AFF)_4](NEt_4)_2$. First of all, the evident colour change in the luminophore emission from red (powder and solution) to pink (PMMA film) already presumed some effect of the polymeric matrix or materials processing on the luminophore. Secondly, the shape of the emission spectrum recorded for the PMMA sample exhibits major variations with respect to that of the solution (Fig. 3.22). All transitions appear to have undergone band broadening effects, with the $^5D_0 \rightarrow {}^7F_2$ transition showing a substantial deformation. This is a clear indication that the coordination site for europium(III) has been modified to a considerable extent by the embedment in PMMA, with consequent alterations in the luminescence properties of the cage. The exact nature of such modification cannot be inferred at this stage, as it would require further structural characterization not yet carried out. Nevertheless, based on previous studies on triple- and quadruple- stranded LOCs[14–16], such variation in the shape of the PL spectrum for $[Eu_2(AFF)_4](NEt_4)_2$ in PMMA could be related to the loss of one AFF ligand. The resulting free-coordination sites could then be saturated by other species present in the matrix, such as residual solvent molecules, or also water deriving from absorbed humidity. Such hypothesis will however need verification in future studies.

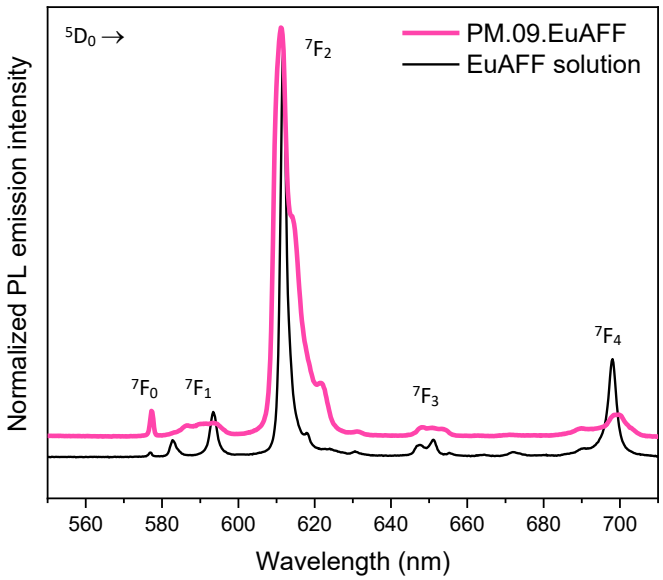


***Figure 3.22*** *Photoluminescence emission spectra (excitation wavelength $\lambda_{exc}$=340 nm) for $[Eu_2(AFF)_4](NEt_4)_2$ in solution and embedded in PMMA.*

Lastly, excited state $^5D_0$ decays were measured, and derived lifetimes are listed in Table 3.5. Data collected for $[Eu(tta)_3phen]$ show that excited state lifetimes for the PMMA samples are not significantly perturbed in passing from the diluted solution to the polymeric matrix, while lifetime values for the PS samples reduce by the 12.5%. A drastic change is instead observed for PM.09.EuAFF lifetime that, with a 60% decrease with respect to the corresponding solution value, would further avail the hypothesis of a modification in the luminophore structure.

***Table 3.5*** *Excited state lifetimes (τ) for luminophores solutions and characterized luminescent films.*

| ***Sample*** | *τ (ms)* |
|---|---|
| **EuTTA solution** | 0.64 |
| **PM.05.EuTTA** | 0.63 |
| **PM.10.EuTTA** | 0.62 |
| **PS.05.EuTTA** | 0.56 |
| **PS.10.EuTTA** | 0.56 |
| **EuAFF solution** | 1.00 |
| **PM.09.EuAFF** | 0.39 |

## 3.5. References


1. Crow Polymer database. http://www.polymerdatabase.com/polymerindex/hom (last accessed: July 2022).
2. Prajzler, V., Neruda, M. & Nekvindová, P. Flexible multimode polydimethyl-diphenylsiloxane optical planar waveguides. *J. Mater. Sci. Mater. Electron.* **29**, 5878–5884 (2018).
3. El-Kalla, E. H., Sayyah, S. M., Afifi, H. H. & Saeed, A. F. Ultraviolet-visible spectroscopic studies of poly(methyl methacrylate) doped with some luminescent materials. *Acta Polym.* **40**, 349–351 (1989).
4. Li, T., Zhou, C. & Jiang, M. UV absorption spectra of polystyrene. *Polym. Bull.* **25**, 211–216 (1991).
5. Gao, S. *et al.* Highly Efficient Luminescent Solar Concentrators Based on Benzoheterodiazole Dyes with Large Stokes Shifts. *Chem. – A Eur. J.* **26**, 11013–11023 (2020).
6. Madsen, M. H., Feidenhans'l, N. A., Hansen, P. E., Garnæs, J. & Dirscherl, K. Accounting for PDMS shrinkage when replicating structures. *J. Micromechanics Microengineering* **24**, 2–12 (2014).
7. PEEK compatibility chart. https://www.zeusinc.com/wp-content/uploads/2022/03/PEEK-Chemical-Compatibility-Chart-V1R1.pdf (last accessed: July 2022).
8. Mano, E. B. & Durao, L. A. Review of laboratory methods for the preparation of polymer films. *J. Chem. Educ.* **50**, 228–232 (1973).
9. Ostos, F. J., Iasilli, G., Carlotti, M. & Pucci, A. High-Performance Luminescent Solar Concentrators. *Polymers (Basel).* **12**, 2898 (2020).
10. Lee, J. N., Park, C. & Whitesides, G. M. Solvent Compatibility of Poly(dimethylsiloxane)-Based Microfluidic Devices. *Anal. Chem.* **75**, 6544–6554 (2003).
11. Sannakki, B. & Anita, A. Dielectric properties of PMMA and its composites with ZrO2. *Phys. Procedia* **49**, 15–26 (2013).
12. Fang, J., Xuan, Y. & Li, Q. Preparation of polystyrene spheres in different particle sizes and assembly of the PS colloidal crystals. *Sci. China Technol. Sci.* **53**, 3088–3093 (2010).
13. Binnemans, K. Interpretation of europium(III) spectra. *Coord. Chem. Rev.* **295**, 1–45 (2015).

14. Brock, A. J., Etchells, I. M., Moore, E. G. & Clegg, J. K. Dinuclear triple stranded phenyl-spaced 1,3-bis-ß-diketonato lanthanide(iii) complexes: synthesis, structures and spectroscopy. *Dalt. Trans.* **50**, 4874–4879 (2021).
15. Bassett, A. P. *et al.* Highly luminescent, triple- and quadruple-stranded, dinuclear Eu, Nd, and Sm(III) lanthanide complexes based on bis-diketonate ligands. *J. Am. Chem. Soc.* **126**, 9413–9424 (2004).
16. Rancan, M. *et al.* Adaptive helicity and chiral recognition in bright europium quadruple-stranded helicates induced by host-guest interaction. *Cell Reports Phys. Sci.* **3**, 100692 (2022).

# Chapter 4

# Functional properties

This Chapter will cover the functional characterizations conducted on fabricated luminescent waveguides in LSC configuration, *i.e.*, coupled with silicon photovoltaic cells along the edges and under simulation of solar irradiation. The topics outlined in the following Paragraphs will regard the assembly of an experimental setup, a first verification of its validity through preliminary measurements, modifications of the same aimed to improve its reliability, and finally proper assessment of samples performance.

## 4.1. Building an experimental setup

Functional characterization of the luminescent solar concentrators was performed by studying the current-to-voltage (I-V) and power-to-voltage (P-V) characteristic curves of the photovoltaic cells edge-coupled to the realized waveguides. The essential components of the measurement setup consist of:

- a source of incident radiation covering the desired wavelengths;
- a source of voltage to apply to the cells circuit ends;
- an output current reader;
- a sample holder ensuring high repeatability of measurements.

The employed setup had been arranged for the first time within the scope of this thesis, assembling all the necessary units listed above.

An ozone-free Xe arc lamp was used as light source and was connected to an optical fibre that allowed to illuminate the sample perpendicularly to its surface. With the available optics, it was possible to generate a circular light spot of 2.0 cm in diameter

irradiated homogeneously with ~ 100 mW/cm$^2$ of incident power (~ 1 sun). The light source could be moved over the sample surface through a 5 axes stage (3 rigid translations x,y,z and 2 rotational angles $\vartheta$,$\phi$) to easily set its position. Through adjustment of the source height, it was possible to extend the illuminated area over 25 cm$^2$, although at the loss of illumination homogeneity. In this second configuration, the incident power reached a maximum of 80 mW/cm$^2$ in a central area of 3.0 cm in diameter, while its value decreased to 40 mW/cm$^2$ moving towards the edges of a 5.0 × 5.0 cm$^2$ substrate.

Regarding the electronic part of the instrumentation, a source meter unit (SMU) and a high precision digital multimer, both computer-controlled, were used in voltage sourcing and current reading mode, respectively. The two sets of data acquired by the instruments were then combined and plotted to yield the complete I-V curves.

A first sample holder was built in a square shape with internal area of 6.0 × 6.0 cm$^2$, and tightly clamped to the 5 axes stage. A thin monocrystalline silicon cell with nominal active area of 2.2 × 0.7 cm$^2$ was cabled and fixed to the holder, rather than attached directly to the samples, to allow an easy interchange between the tested waveguides. Fig. 4.1 shows the initially assembled experimental setup.

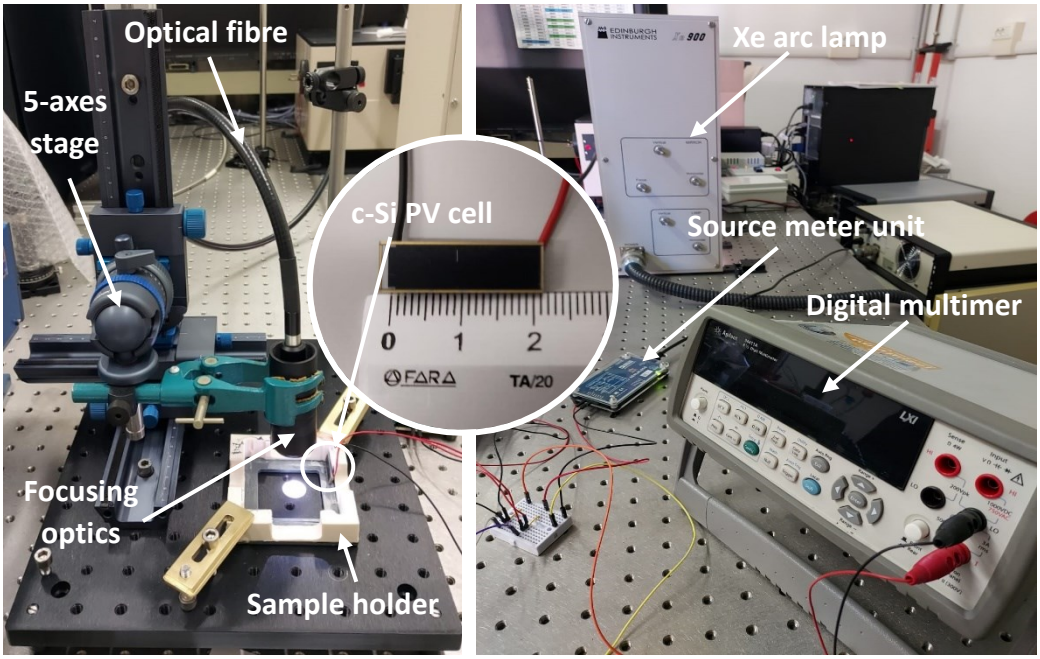


***Figure 4.1*** *Pictures of the arranged experimental setup with indication of the several components. Inset: close-up of the photovoltaic cell on a reference scale.*

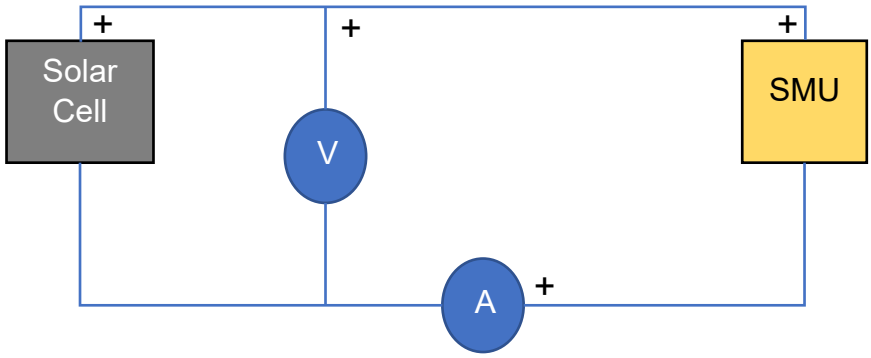


***Figure 4.2*** *Schematics of the employed electronic circuit, where SMU = source meter unit, and A, V = multimer for measuring the current (A) or the voltage (V).*

## 4.2. Validation of measurements and setup optimization

Prior to any LSC measurement, the current-to-voltage curve of the bare photovoltaic cell was collected, setting the light source perpendicular to the cell's surface and at ~ 1 sun incident power. Room lighting was turned off during this acquisition and all the following, so to minimize secondary light sources. The resulting I-V and P-V characteristics are reported in Fig. 4.3, along with typical electrical parameters: short-circuit current ($I_{SC}$), open-circuit voltage ($V_{OC}$), maximum peak power ($P_{max}$) and fill factor (FF).

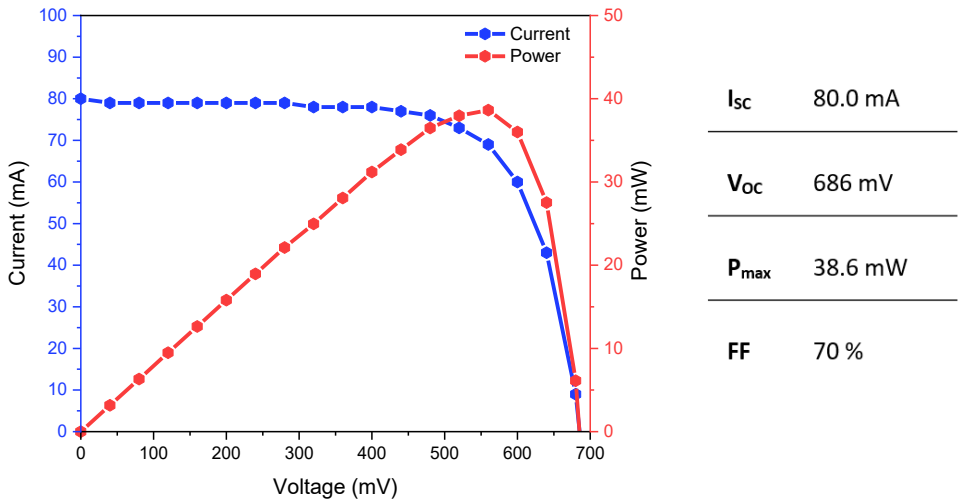


***Figure 4.3*** *Characteristics for the employed photovoltaic cells harvested under simulation of solar irradiation, with derived values for electrical parameters.*

First functional tests were performed using only one photovoltaic cell, so to assess the validity of the assembled setup and the measurement procedure with a simpler initial system. The PV cell was attached in a vertical position on one wall of the sample holder, near one of its corners, and maintained in this position during all experiments. The light source was set in the first mentioned configuration, as a spot of 2.0 cm in diameter and reaching ~ 100 mW/cm$^2$ (~ 1 sun) of incident power.

A 2.5 × 2.5 × 0.8 cm$^3$ PDMS tile containing [Eu(tta)$_3$phen] at the 0.007% by weight was then tested. The PV cell well adhered to one side of the waveguide just by exercising light pressure between the two parts. The collected P-V curves for the doped material and for an equivalent undoped sample are reported in Fig. 4.4. It is of note how the electrical power output of the undoped sample accounts for the 75% of that of the sample containing [Eu(tta)$_3$phen], meaning that the main contribute to the generated current comes from waveguiding of the incident light towards the collector rather than from luminophore emission. The luminescence exhibited by the doped tile under the employed illumination also appeared much more dimmed than that observed on the same sample with UV illumination at 365 nm. This could be primarily ascribed to the use of a different light source and to the limited concentration of luminophore inside the matrix, of which the fainter luminescence could be easily outweighed by the large component of white light entering the tile and re-emerging as such.

The I-V curves relative to these measurements and all the following are reported in Appendix B.

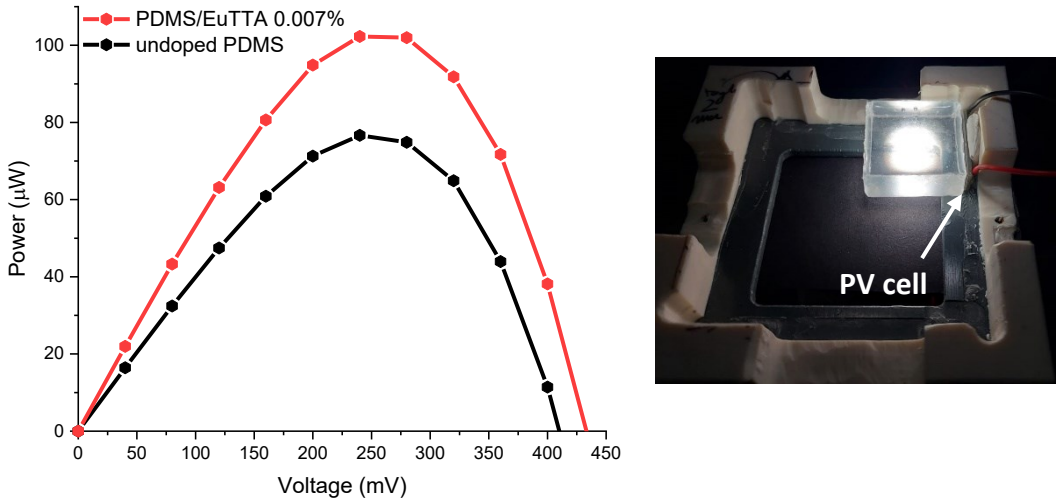


***Figure 4.4*** *Collected P-V characteristics (left) for a 2.5 × 2.5 × 0.8 cm$^3$ PDMS tile containing [Eu(tta)$_3$phen] at the 0.007% by weight and an analogous blank sample. Picture of the doped sample edge-coupled with the PV cell and under the employed white light illumination (right).*

Next, a series of 5.0 × 5.0 $cm^2$ PMMA films on glass containing [Eu(tta)$_3$phen] was examined (see Table 4.1), along with an equivalent blank sample. All the films were casted onto pre-treated glass slabs and characterized shortly after preparation, so they retained adherence to the substrate throughout the measurements.

***Table 4.1*** *Luminophore weight concentrations (w/w), $Eu^{3+}$ molar content ($n_{Eu}$) and film thickness (d) for characterized samples.*

| ***Sample name*** | *w/w (%)* | $n_{Eu}$ *(mol · $10^{-6}$)* | *d (μm)* |
|---|---|---|---|
| **PM.04.EuTTA** | 0.4 | 2.1 | 180 |
| **PM.10.EuTTA.a** | 1.0 | 5.0 | 88 |
| **PM.10.EuTTA.b** | 1.0 | 5.2 | 101 |

The light source was kept as a 2.0 cm spot and used to probe three different portions of the sample surface (Fig. 4.5): the corner opposite to the PV cell (spot 1), the centre (spot 2), and the corner near to the PV cell (spot 3). Since the cell was not entirely covered by the sample in height, its exposed area was screened from the light coming directly from the source by placing a black frame onto the film surface. A careful shielding of the cell from direct illumination is an essential requirement to perform reliable measurements, since all light reaching the cell other than that incoming from the waveguide emissive edges can lead to substantial overestimation of the measured current[1].

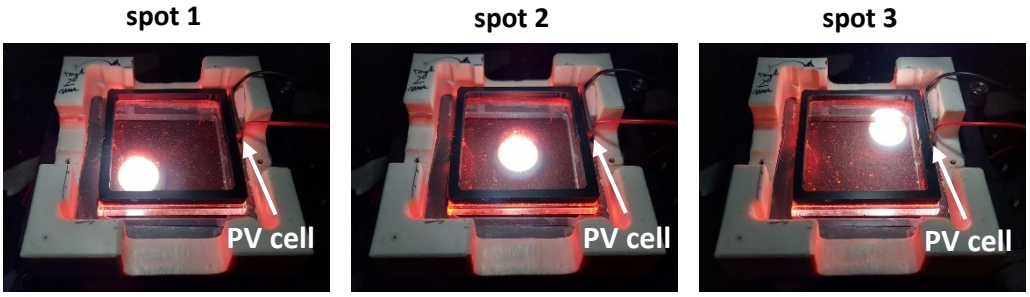


***Figure 4.5*** *Different probed positions on the 5.0 × 5.0 $cm^2$ films with a circular white light spot of 2.0 cm in diameter. The edge-coupled PV cell (up-right corner of the sample holder) is shielded from direct illumination with a square black frame.*

We consider first the P-V curves relative to spot 1 and 2 (Fig. 4.6). As expected, the further the light source is from the cell, the lower the electrical output is, because the emitted radiation has to travel longer distances inside the waveguide to reach the

collector and is therefore subjected to more events that cause optical losses (*i.e.,* a greater number of internal reflections with non-unitary efficiency)[2]. Both sets of data show the same trend between the outputs generated by different samples: higher concentrations of luminophore produce higher currents and, when at the same concentration, the thicker film has the highest output. These findings suggest that, for concentrations and thicknesses up to those investigated, an increase in the amount of embedded luminophore determines an overall improvement in the LSC performance. At variance with what observed for the PDMS tile, all tested films exhibited the red luminescence proper of $Eu^{3+}$. Moreover, the contribution to the total electrical power output of doped films originating just by waveguiding of the incident white light covers smaller fractions than in the case of the PDMS tile. Its value ranges from 15% to 35% in going from the most to the less concentrated films, as estimated by the characteristics collected for the blank sample.

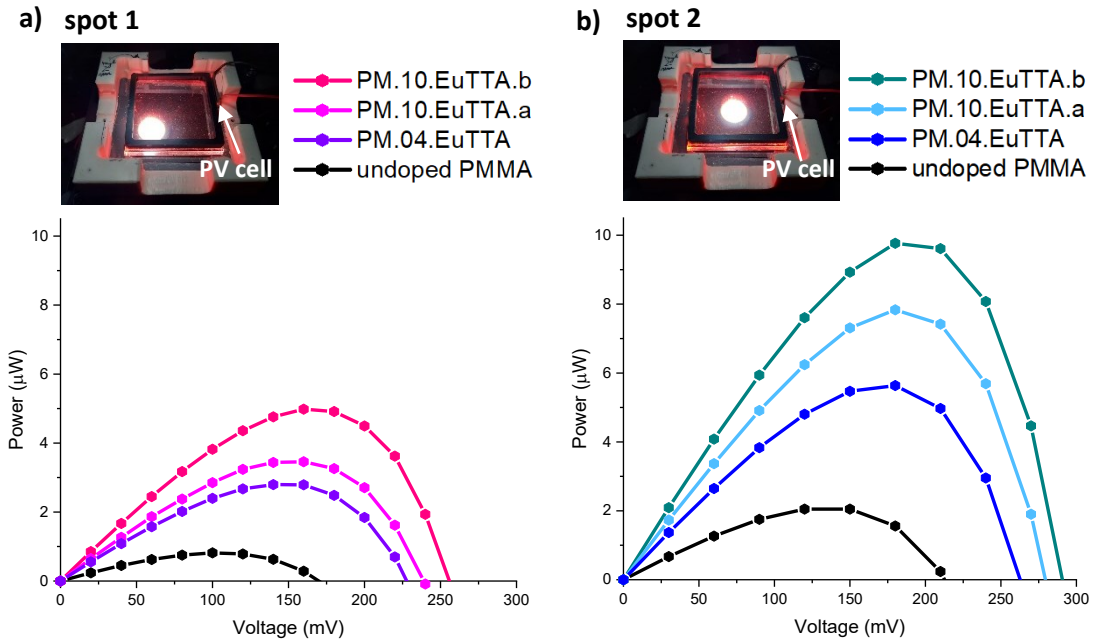


***Figure 4.6*** *Collected P-V characteristics for a series of 5.0 × 5.0 cm² PMMA films containing [Eu(tta)₃phen] at different concentrations, with the light source placed over a) spot 1 and b) spot 2.*

Good repeatability between different sets of acquisitions was achieved for both tested spots, while the same has not been found in the case of spot 3. First of all, no definite trend between the samples could be identified, as the sequence of the P-V curves varied from one set of acquisitions to the other and did not resemble that found for spots 1 and 2 (Fig. 4.7a). Secondly, several voltage sweeps carried out on the same samples after removing and placing them again in the sample holder along with the frame,

yielded significantly different outputs, affected by relative errors up to the 15% (Fig. 4.7b).

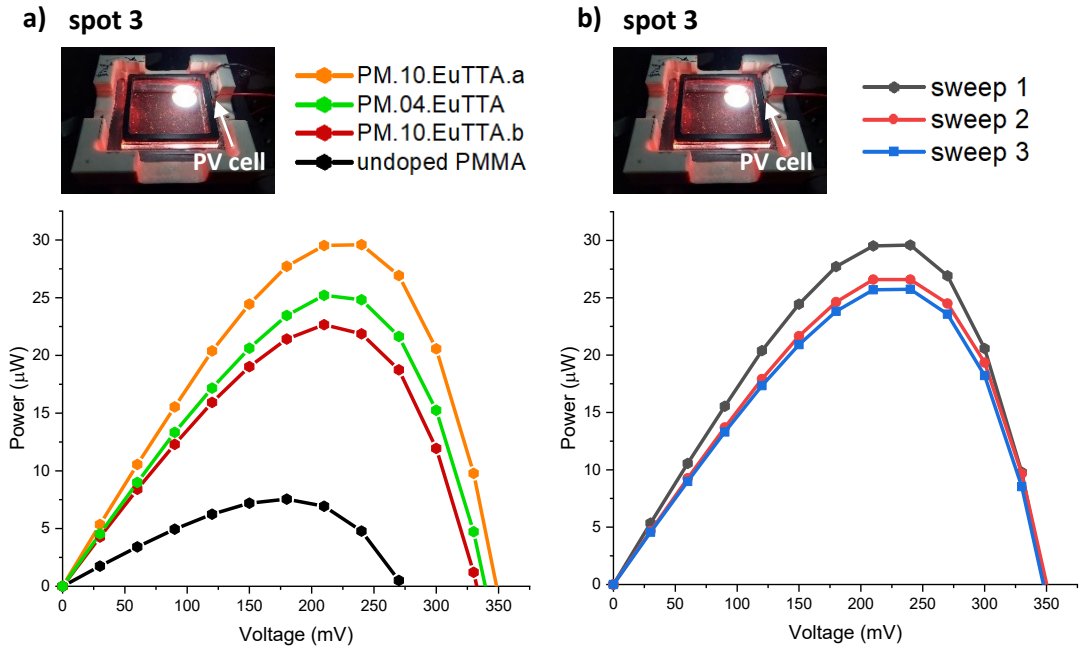


***Figure 4.7*** *Collected P-V characteristics, with light source placed over spot 3, for a) the whole series of tested 5.0 × 5.0 cm² PMMA films and b) PM.10.EuTTA.b over three different voltage sweeps, carried out after removing and replacing the sample in the holder.*

Such variability in the collected data was attributed to the poor accuracy in positioning the sample and the screening frame inside the holder always in the same configuration, which caused the cell to be shielded from direct illumination to different extents between different acquisitions.

In order to achieve an efficient and reliable coverage of the cell's exposed surface, a new sample holder of 5.0 × 5.0 cm$^2$ internal area was built, equipped with eight PV cells (two per side) and an appositely shaped upper shield (Fig. 4.8). Repeatability in the placement of the sample improved, due to the holder being tailored to the exact dimensions of the waveguides, while cells coverage presented again an issue, with measurements still affected by a 15% relative error. After testing several adjustments to the shield, a second version of it was crafted, which allowed full coverage of the sample holder's frame, including its corners. By employing this last shield, the quality of measurements greatly improved, with the relative error between different acquisitions on the same sample reduced to the 4%.

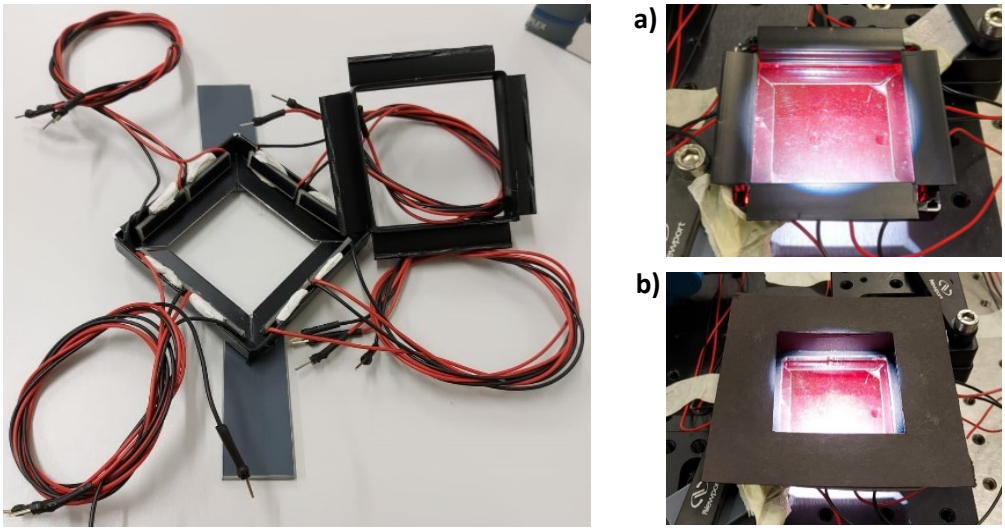


***Figure 4.8*** *New sample holder of 5.0 x 5.0 cm$^2$ internal area, mounted with eight photovoltaic cells and equipped with a tailored upper shield (left). On the right, pictures of a PMMA luminescent film placed in the holder and covered with the a) original and b) optimized version of the shield.*

## 4.3. LSC functional characterizations

With the optimized measurement setup, functional characterizations were conducted on the same samples previously characterized in photophysical terms in Chapter 3 (see Table 3.4). By the time the functional tests were performed, the PS films had undergone detachment from the substrate, so they were tested in two different configurations: either propped on top of a glass plate to act as a waveguide as was the case for supported films, or placed directly into the sample holder without any supporting material. However, both dispositions could not achieve an optimal stacking of the shield onto the sample, due to the bending assumed by the PS films upon detachment. The curvature of the films, in fact, caused them to remain partially lifted from the surface of the glass slide (or of the sample holder in the absence of the support), even when covered with the shield, as it was not heavy enough to flatten them. The portion of the cells between the slide and the shield thus remained exposed to direct illumination. On the other hand, the PMMA films retained good adherence to the glass, and were characterized as proper supported films.

All eight cells were connected in parallel and the light source height was adjusted to illuminate all the exposed sample surface, which corresponded to an area of 4.3 × 4.3 cm$^2$, since the shield took some space on the inner edges of the holder. The source

incident power reached 80 mW/cm$^2$ (~ 0.8 sun) in the central area of the sample, while decreasing to 40 mW/cm$^2$ (~ 0.4 sun) in going towards the edges.

Measured electrical characteristics for PMMA and PS samples are shown in Fig. 4.9 and 4.10, respectively.

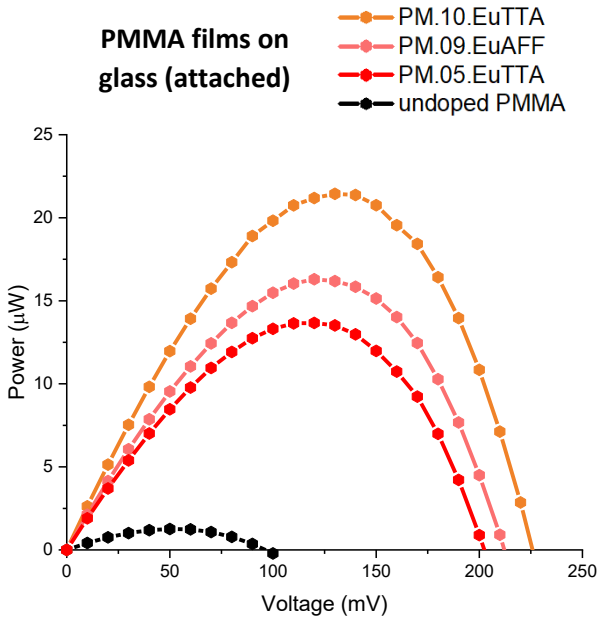


***Figure 4.9*** *Collected P-V characteristics for the PMMA supported films coupled to PV cells along the whole perimeter and under ~ 0.8 sun illumination.*

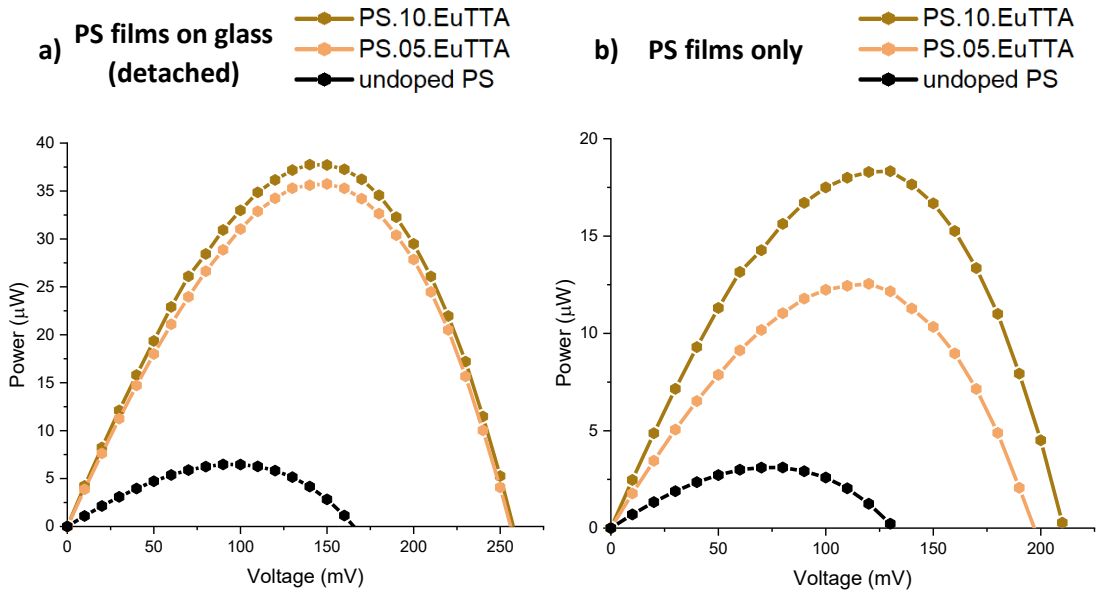


***Figure 4.10*** *Collected P-V characteristics for the PS films coupled to PV cells along the whole perimeter and under ~ 0.8 sun illumination. The films were characterized by placing them in the sample holder a) with a supporting glass slate and b) without it.*

All samples presented red luminescence under the employed lighting, apart from PM.09.EuAFF which exhibited pink luminescence, as already observed under UV illumination at 365 nm.

As previously noted, films with the highest concentration of luminophore produce the greatest outputs. A substantial increase in the maximum peak power is observed for the PS films on glass, detached, with respect to the PMMA ones, with the $P_{max}$ value of PS.10.EuTTA being one and a half times that of PM.10.EuTTA (see Table 4.2). Furthermore, the $P_{max}$ values registered for the PS films without the supporting glass slate are comparable to those of the supported PMMA films, meaning that an emitting waveguide edge of ~ 200 μm would roughly produce the same outputs of one of ~ 3 mm, given the same luminophore at the same doping concentration. The unlikelihood of these data suggests that the issue of direct illumination reaching the cells due to the non-ideal placement and coverage of the PS films in the sample holder causes a substantial overestimation of the current readings, and consequently of the P-V characteristics.

On the other hand, an optimal suppression of any direct illumination source can be appreciated for the PMMA films, which also show a decreased contribution from the matrix waveguiding with respect to the unoptimized experimental setup. In this case, the total power outputs show a 5% to 9% contribution of the sole PMMA matrix, in going from the most to the less concentrated films. This is further proof that an accurate shielding of the exposed PV surface is essential to achieve reliable measurements.

Electrical parameters derived for all characterized samples are listed in Table 4.2.

***Table 4.2*** *Short-circuit current ($I_{LSC}$), short-circuit current density ($J_{LSC}$), open-circuit voltage ($V_{OC}$), maximum power ($P_{max}$) and fill factor (FF) for characterized 5.0 × 5.0 cm² PMMA and PS films.*

| ***Sample name*** | $I_{LSC}$ *(mA)* | $J_{LSC}$ *(mA/cm²)* | $V_{OC}$ *(mV)* | $P_{max}$ *(μW)* | *FF (%)* |
|---|---|---|---|---|---|
| ***PMMA films on glass (attached)*** | | | | | |
| **PM.10.EuTTA** | 0.265 | 0.041 | 225.70 | 21.44 | 36 |
| **PM.09.EuAFF** | 0.213 | 0.033 | 212.27 | 16.30 | 36 |
| **PM.05.EuTTA** | 0.190 | 0.030 | 202.16 | 13.67 | 36 |
| **PMMA matrix** | 0.043 | 0.007 | 96.70 | 1.26 | 30 |

*continued next page*

| *PS films on glass (detached)* | | | | | |
|---|---|---|---|---|---|
| **PS.10.EuTTA** | 0.418 | 0.065 | 257.2 | 37.75 | 35 |
| **PS.05.EuTTA** | 0.389 | 0.060 | 255.6 | 35.73 | 36 |
| **PS matrix** | 0.110 | 0.017 | 164.6 | 6.48 | 36 |
| *PS films only* | | | | | |
| **PS.10.EuTTA** | 0.248 | 0.039 | 210.2 | 18.33 | 35 |
| **PS.05.EuTTA** | 0.179 | 0.028 | 196.4 | 12.55 | 36 |
| **PS matrix** | 0.071 | 0.011 | 131.9 | 3.11 | 33 |

Regarding LSC figures of merit, the calculated optical efficiency ($\eta_{opt}$), overall power conversion efficiency (PCE) and concentration factor (C) are provided in Table 4.3 for PMMA samples only, since reliable data are not available for the PS films.
The expressions for mentioned parameters defined in Chapter 1 are recalled below[3,4].

$$C = \eta_{opt} \cdot G \tag{4.1}$$

$$\eta_{opt} = \frac{I_{LSC}}{I_{SC} \cdot G} \tag{4.2}$$

$$PCE = \frac{J_{LSC} \cdot V_{OC} \cdot FF}{P_{in}} \tag{4.3}$$

***Table 4.3*** *Figures of merit for the characterized PMMA luminescent films.*

| ***Sample name*** | *G* | *C* | $\eta_{opt}$ *(%)* | *PCE (%)* |
|---|---|---|---|---|
| **PM.10.EuTTA** | 3.90 | 0.0016 | 0.042 | 0.0042 |
| **PM.09.EuAFF** | 3.90 | 0.0013 | 0.034 | 0.0031 |
| **PM.05.EuTTA** | 3.90 | 0.0012 | 0.030 | 0.0027 |

Obtained efficiency values for [Eu(tta)$_3$phen]-doped films result significantly lower than those found in literature for analogous LSCs[5,6], reaching discrepancies up to two orders of magnitude. Although evaluating the competitivity of the fabricated LSCs was not the primary objective of the functional characterizations carried out in this study, improvement of performance will require future investigations into the loss factors affecting the waveguides. Moreover, the shading of almost half of the PV cells area, although unavoidable for the specific experimental setup here designed, surely has a detrimental effect on their efficiency. While the design of the measurement setup still offers room for improvement, the high repeatability of measurements and the assessed proper functioning of the fabricated LSCs are remarkable results achieved within this thesis.

## 4.4. References


1. Yang, C., Liu, D. & Lunt, R. R. How to Accurately Report Transparent Luminescent Solar Concentrators. *Joule* **3**, 2871–2876 (2019).
2. Meinardi, F. *et al.* Highly efficient large-area colourless luminescent solar concentrators using heavy-metal-free colloidal quantum dots. *Nat. Nanotechnol.* **10**, 878–885 (2015).
3. Mazzaro, R. & Vomiero, A. The Renaissance of Luminescent Solar Concentrators: The Role of Inorganic Nanomaterials. *Advanced Energy Materials* **8**, 1801903 (2018).
4. Roncali, J. Luminescent Solar Collectors: Quo Vadis? *Advanced Energy Materials* **10**, 2001907 (2020).
5. Tonezzer, M. *et al.* Luminescent solar concentrators employing new Eu (TTA)3phen-containing parylene film. *Prog. Photovoltaics Res. Appl.* **20**, 6–11 (2015).
6. Wang, X. *et al.* Europium complex doped luminescent solar concentrators with extended absorption range from UV to visible region. *Sol. Energy* **85**, 2179–2184 (2011).

# Chapter 5

# Conclusions and perspectives

In this study, a variety of luminescent solar concentrators has been developed employing two different $Eu^{3+}$ antenna complexes as luminophores. The work has covered all aspects of LSC design, from the synthesis of the emitter to fabrication of the material and up to the device assembly and characterization. The emitting molecules comprised $[Eu(tta)_3phen]$, a β-diketone frequently found in LSC literature and here taken as benchmark compound in all stages of the study, and a di-nuclear quadruple-stranded LOC of the family $[Ln_2L_4]^{2-}$, where the lanthanide centres are $Eu^{3+}$ ions and the L ligand is a newly synthetized bis-β-diketone. The polymers employed to fabricate the LSC waveguides were PDMS, PMMA and PS. Through elaboration of already existing procedures, the fabrication of bulk-doped PDMS tiles with variable size and of luminescent PMMA and PS films of 5.0 x 5.0 $cm^2$ area and thickness of ~ 200 μm, both free-standing and supported on glass, was achieved.

The absorption and emission properties of the luminophores have been first assessed in solution, and later in the solid matrix by characterization of the PMMA and PS films. Both hosts show optimal transparency over the wavelengths relevant to the luminophores absorption, meaning that the spectral features showed by the waveguides are ascribable for the most part to the luminophores. No significant change has been observed for $[Eu(tta)_3phen]$ upon embedding, while the LOC presented evident modifications of its absorption and emission spectra when embedded in PMMA, accompanied by a decrease in the intensity of the emitted light. Defined as a spectroscopic structural probe, the $Eu^{3+}$ ion is sensitive to modifications in its chemical surroundings, reflecting such changes in the shape of its luminescence spectrum. This

insight has led to the conclusion that incorporation of the LOC into PMMA induces a structural change in the europium coordination site, most likely associated to the loss of one ligand, which is the reason of the significant alteration in the photophysical properties of the complex.

The effects of materials processing on the final obtained waveguides have been investigated through structural and thermal characterizations. It was assessed that, within the employed experimental conditions, the matrices retain their original amorphous structure without showing sign of crystalline regions. The residual solvent content of the PMMA and PS waveguides reached the 15% by weight for the former and the 10% for the latter. The flexibility showed by the free-standing films is ascribable to such large portions of trapped solvent.

Finally, the fabricated LSCs have been functionally characterized by harvesting the I-V and P-V curves of edge-coupled Si PV cells with simulation of solar illumination. After building the experimental setup, the same has been validated through preliminary measurements and repeatedly modified to reach the desired data reliability. Shielding the PV cells from direct illumination has proved to be a critical aspect in the optimization of the setup, necessary to avoid overestimation of the electrical outputs. Data collected from such characterizations denote the proper functioning of the developed LSCs, in that the absorption and re-emission of the incident light enacted by the luminophore account for the 90% – 95% of the total extracted electrical power.

Future works will be oriented towards a more detailed study of the effects of embedding on the luminophores' structure and how detrimental outcomes can be prevented. The kinetics of solvent evaporation and release from the polymeric matrices after processing will also be the matter of further investigations, with the aim to establish a correlation between residual solvent content and flexibility of the final obtained material. Flexible waveguides could also offer the possibility to study LSCs in non-planar configurations. Moreover, expanding the range of available materials and procedures, as in testing different LOCs, developing new ligands and complexes and achieving higher control on the waveguides fabrication and geometry, will be one of the goals for forthcoming research.

# Chapter 6

# Experimental

## 6.1. $Eu^{3+}$ complexes synthesis

The reagents were purchased from Sigma-Aldrich and used as received. The AFF ligand has been prepared following an already refined procedure[1].

**– [Eu(tta)$_3$phen]**

In a 250 mL 3 necks round bottom flask, thenoyltrifluoroacetone (1.72 g, 7.7 mmol) and 1,10-phenathroline (0.46 g, 2.6 mmol) have been dissolved in 40.0 mL of ethanol at 60 °C. Under magnetic stirring, 50 mL of an ethanolic solution of NaOH (0.32 g, 8.0 mmol) have been added to the ligand mixture, reaching a pH of 7. A solution of $EuCl_3 \cdot 6H_2O$ (0.96 g, 2.6 mmol) in 70 mL of ethanol has been added dropwise to the ligand and base solution, observing immediate formation of a white solid, and the mixture has been left to react at reflux for 4 hours. After that, the reaction flask has been removed from heating and left to cool until reaching room temperature, then placed at 0 °C for the night. Next, the precipitate has been isolated from the mixture by filtration on paper (porosity: 6 μm) and washed with cold ethanol. After drying on $P_2O_5$ under vacuum, the product has been purified by dissolving it into 60 mL of THF at 50 °C and filtering by gravity solution on a gooch filter (porosity: 3) while still hot. The solvent has then been removed under reduced pressure, and the solid left drying under vacuum. The final product has been obtained as 1.96 g of yellowish white powder, with a yield of 75%.

**– AFF precursor**

In a 250 mL 3 necks round bottom flask, p-bromoacetophenone (7.20 g, 36.2 mmol), *tert*-butylcarbamate (1.45 g, 12.4 mmol), $K_3PO_4$ (15.73 g, 74,0 mmol), and CuI (0,70 g, 3.7 mmol) have been dissolved in 60 mL of anhydrous toluene under Ar atmosphere. N,N-dimethylethylenediamine (1.2 mL, 11.1 mmol) has been added to the solution, which immediately turned blue. The formation of a white precipitate has been observed, and the reaction mixture has been stirred at 110 °C for 48 hours. After 24 hours, the mixture appeared red and presented dark yellow precipitate, and after 48 hours the solution had turned to brown. The reaction has been quenched by the addition of water (150 mL) and ethyl acetate (160 mL). After transferring the mixture in a separating funnel, the blue aqueous phase has been washed with ethyl acetate (2x50 mL) and then removed. The brown organic phase has been washed with water (3x100 mL), dried over $MgSO_4$ and the solvent has been removed under reduced pressure resulting in a dark orange dense oil. The product has been purified by $SiO_2$ column chromatography (n-hexane/ethyl acetate 6:4) to give 4.09 g of a yellow dense oil. $^1$H-NMR (25 °C, 300 MHz, $CDCl_3$): δ [ppm] = 7,92 (4H, m), 7,26 (4H, m), 2,59 (6H, s), 1,46 (9H, s).

**– AFF ligand**

In a 250 mL 3 necks round bottom flask, metallic Na (0.94 g, 40.9 mmol) has been dissolved in ethanol (40 mL) under Ar atmosphere, keeping the flask in an ice and water bath. After complete dissolution of Na (~ 1 hour), ethyl pentafluoropropionate (4.2 mL, 30.6 mmol) and 10 mL of AFF precursor (4.09 g, 11.6 mmol) in ethanol have been added under magnetic stirring, giving a yellow solution that turned dark red over time. The reaction mixture has been stirred at room temperature for the night. Next, the solvent has been removed under reduced pressure, and a dark orange oil was obtained. After addition of water (100 mL) and HCl 10% aqueous solution (15 mL), the formation of a yellow precipitate occurred. The solution has been extracted (100 mL) and then washed (2x40 mL) with $CH_2Cl_2$. The organic phase has been dried over $MgSO_4$ and the solvent has been removed under reduced pressure, resulting in a dense dark orange oil. The product has been purified by recrystallization from acetonitrile/water (1:4) and isolated through centrifugation cycles of 3 minutes at 6000 rpm. After supernatant removal, the obtained fine solid has been dried on $P_2O_5$ under vacuum. The final product has been obtained as 5.75 g of yellow coarse solid.

Yield: 72%. $^{1}$H-NMR (25 °C, 300 MHz, $CDCl_3$): δ [ppm] = 7,93 (4H, m), 7,32 (4H, m), 6,56 (2H, s), 1,48 (9H, s).

**– $[Eu_2(AFF)_4](NEt_4)_2$**

In a 4 mL screw cap vial, the AFF ligand (80.1 mg, 0.12 mmol) has been dissolved in 2 mL of ethanol at 50 °C. A ~ 1.5 M methanolic solution of tetraethylammonium hydroxide (167 μL, 0.25 mmol) has been added to the ligand solution, followed by addition of $EuCl_3 \cdot 6H_2O$ (18.4 mg, 0.05 mmol), previously dissolved in 1 mL of ethanol. The formation of a suspension of fine white solid has been immediately observed, and the reaction mixture has been stirred at room temperature for 4 hours. Next, the precipitate has been isolated from the mixture through centrifugation cycles of 3 minutes at 6000 rpm and dried on $P_2O_5$ under vacuum. The final product has been obtained as 46.3 mg of white powder. Yield: 30%.

## 6.2. Substrates preparation

All surfaces used for the casting of polymer blends were pre-emptively cleaned with soap and rinsed with deionized water, acetone, and 2-propanol, in this sequence. The eventual acid pre-treatment of the glass slates employed for the supported PMMA and PS films was carried out after the first cleaning and rinsing with deionized water. The slates were immersed in HCl 6 M and kept in the bath for ~ 15 hours, then removed and rinsed with de-ionized water, acetone, and 2-propanol, in this sequence.

## 6.3. Mass spectrometry

ESI-MS analyses were performed with a trap mass spectrometer LCQ Fleet (Thermo Scientific), equipped with a HESI source. The mass spectra were obtained in negative ion detection mode by analysing sample solutions at a concentration of $10^{-5}$ M in acetonitrile via direct infusion with syringe pump (8 μL/min). The instrumental conditions were the following: $T_{HESI}$ = 35 °C; $T_{transfer\ capillary}$ = 275 °C; HESI voltage = 4 kV; gas flow of nebulization (nitrogen): 10 a.u.; auxiliary gas flow (nitrogen): 5 a.u.

## 6.4. Photophysical characterizations

Absorption spectra were recorded on a CARY5000 double-beam spectrophotometer in the 300 − 800 nm range, with a spectral bandwidth of 2 nm. The contribution due to the solvent was subtracted for measurements carried out on the luminophores in solution. The supported luminescent films were characterized by placing the glass slates perpendicularly to the incident beam, the side with the film facing the light source; in this case the contribution of a bare glass slate with same thickness of the supporting ones was subtracted.

Photoluminescence spectra were recorded with a Horiba JobinYvon Fluorolog-3 spectrofluorimeter equipped with double-grating monochromator in both the excitation and emission sides coupled to a R928P Hamamatsu photomultiplier and a 450 W Xe arc lamp as the excitation source. The measurements were performed using the usual 90° geometry for the solutions and for the films, with the latter facing the direction of the incident beam. Emission spectra were corrected for detection and optical spectral response of the spectrofluorimeter supplied by the manufacturer.

The luminescence lifetimes in the microsecond – millisecond scales were measured by a pulsed Xe lamp with variable repetition rate and elaborated with standard software fitting procedures.

Absolute photoluminescence quantum yields (PLQY) were calculated by corrected emission spectra obtained with an apparatus consisting of a Spectralon coated Integrating Sphere accessory (4”, F-3018, Horiba Jobin Yvon), fitted in the fluorimeter sample chamber.

## 6.5. Powder X-ray diffraction

XRD measurements were recorded on a Bruker D8 advance powder diffractometer, equipped with a LYNXEYE XE-T detector and a TWIST-TUBE (Cu) X-ray source. The samples were prepared by cutting small pieces of polymeric film and placing them on Si low background sample holders. The acquisitions were run in Bragg-Brentano geometry, on non-rotating samples, and with an anti-scatter screen. Diffractograms have been collected within a 5° − 60° angular range, with an acquisition rate of 3°/min.

## 6.6. Thermal analyses

TGA measurements were performed on a TA Instruments SDT 2960 simultaneous TG/DSC system. The scans were recorded at a heating rate of 10 °C $min^{-1}$ in a temperature range of 20 – 650 °C. Experiments were carried out in $N_2$ atmosphere.
DSC measurements were performed on a TA Instruments 2920 calorimeter in endothermic mode. The samples were prepared by weighing ~ 5 mg of polymeric film and closing it in an aluminium pan. The scans were recorded at a heating rate of 10 °C $min^{-1}$ in a temperature range of 20 – 200 °C. Experiments were carried out in $N_2$ atmosphere.

## 6.7. Functional characterizations

The simulation of solar irradiation was achieved using a Edinburgh Instruments Xe900 450 W ozone-free Xe arc lamp, and a Thorlabs liquid light guide of 5 mm core diameter. The spectral irradiance of the lamp and the transmission curve of the optical fibre are reported in Fig. 6.1. The I-V and P-V curves provided by the supplier for the employed IXOLAR™ SolarBITs (IXYS) photovoltaic cells are reproduced in Fig. 6.2, among the nominal electrical parameters. An Analog Devices ADALM1000 module and an Agilent 34405A 5.5-Digit Multimeter were used as voltage source and ammeter, respectively.

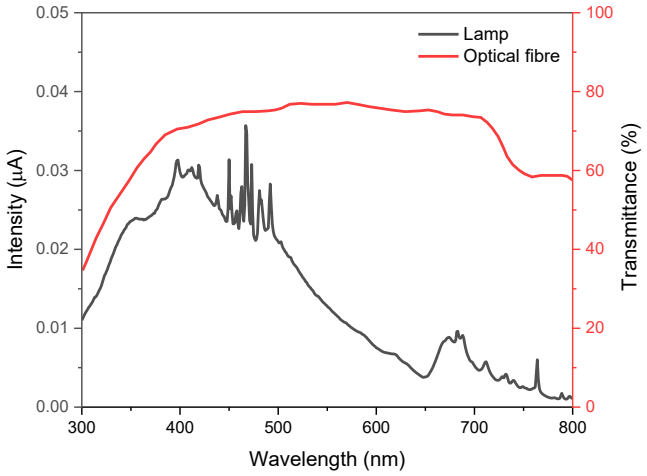


***Figure 6.1*** *Spectral irradiance profile for the employed light source (grey line) and transmission curve for the employed optical fibre (red line).*

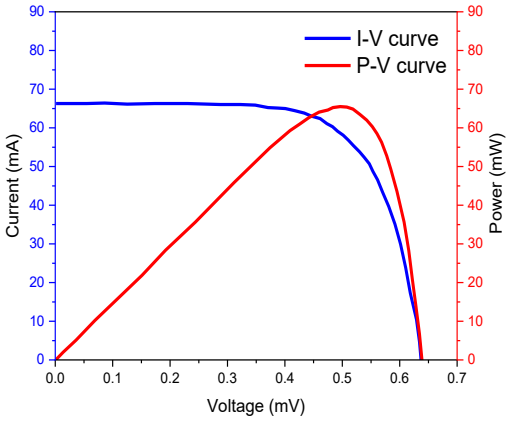


**Electrical Characteristics**

| Symbol | Cell Parameter | Typical Ratings * | Units |
|---|---|---|---|
| $V_{oc}$ | open circuit voltage | 630 | mV |
| $J_{sc}$ | short circuit current density (wafer Level) | 42.4 | $mA/cm^2$ |
| $V_{mpp}$ | voltage at max. power point | 501 | mV |
| $J_{mpp}$ | current density at max. power point (wafer Level) | 37.2 | $mA/cm^2$ |
| $P_{mpp}$ | maximum peak power (wafer Level) | 18.6 | $mW/cm^2$ |
| FF | fill factor | > 70 | % |
| η | solar cell efficiency (wafer Level) | 22 | % |

***Figure 6.2*** *Nominal electrical characteristics for the employed PV cells.*

## 6.8. References

1. Carlotto, A. Tesi di Dottorato. (Università degli Studi di Padova, 2021).

# Appendix A

## • Solar irradiance and the AM1.5G spectrum

The energy of a light source is usually reported as an irradiance, namely as power per unit area ($W/m^2$ in SI units). The *spectral* irradiance takes into consideration also the dependence on the wavelength ($W/m^2nm$ in SI units). Considering the Sun as the light source of interest, the amount of solar energy incident on a given location on Earth's surface is not a constant, as it varies with the time of day, weather conditions and latitude[1]. In order to standardize data and measurements for applications related to solar energy, as photovoltaics, reference solar irradiance spectra have been defined, among which the most widely used is the AM1.5G solar spectrum (Fig. A.1.a). The AM abbreviation indicates the air mass coefficient, which is defined as the ratio of the direct optical path length of solar irradiance through the Earth's atmosphere to the zenith optical path length[1]. Therefore, the air mass coefficient describes the atmosphere thickness that the radiation has to cross to reach the terrestrial surface, depending on the sun's position (Fig. A.1.b). Standard test conditions for photovoltaic modules include the use of AM1.5G illumination and a working cell temperature of 25 °C. The total incident solar power of the AM1.5G spectrum corresponds to 1000 $W/m^2$, or "1 sun", by definition[2].

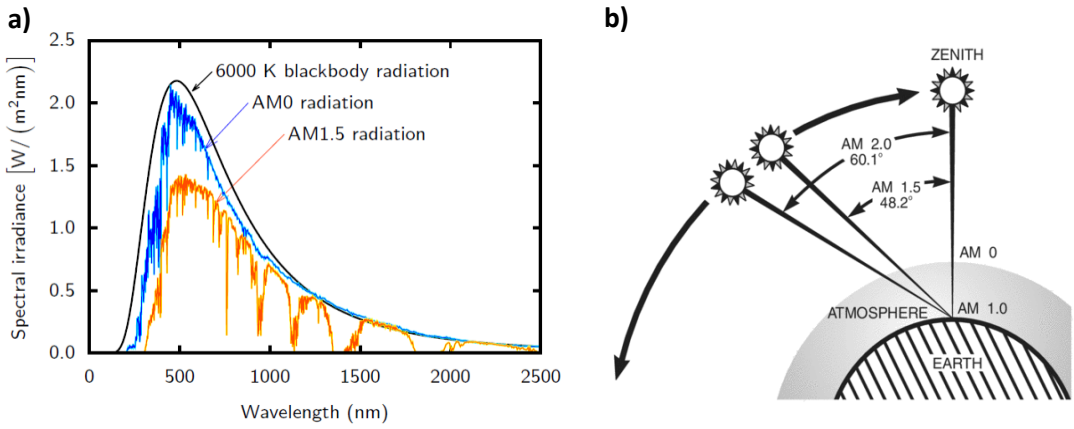


***Figure A.1*** *a) Spectral irradiance spectra for the blackbody radiation at 6000 K (black line) and for the AM0 (blue line) and the AM1.5 (red line) radiations in standard temperature conditions. b) Depiction of several solar incidence geometries with the corresponding air mass coefficients (adapted from ref. 2).*

Among the light sources employed to simulate solar irradiation, Xe arc lamps have historically been the most employed, and are still the most common choice in PV testing[3]. Fig. A.2 shows the irradiation spectrum of a Xe arc lamp superimposed to the AM1.5G spectrum, where the good spectral match can be appreciated up to 700 nm. The Xe irradiance spikes interesting the NIR region can be suppressed for the most part by employing apposite optical filters.

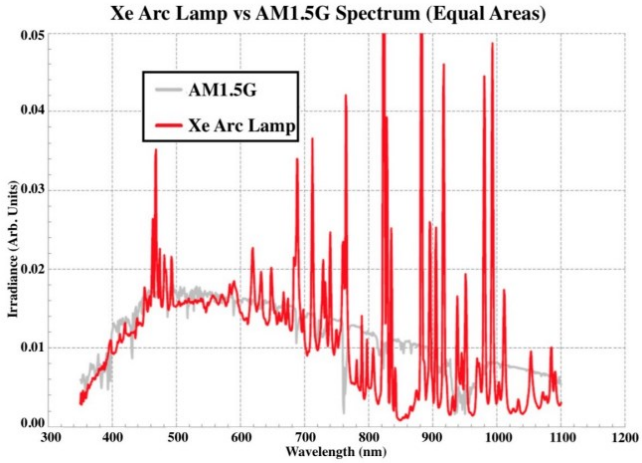


***Figure A.2*** *Overlap between the irradiance spectrum of a Xe arc lamp and the AM1.5G solar spectrum*[3].

- # Working principle of a photovoltaic cell

A photovoltaic cell is an electronic device capable of converting incoming solar energy into electrical current through a semiconductor layer, which consists of a *p*-*n* junction[4]. When incident photons of sufficient energy strike the semiconductor material, they promote electrons from its valence to its conduction band, generating electron-hole pairs (EHPs). The built-in electric field of the junction forces the generated electrons to move towards the *n* region, and the corresponding holes to move towards the *p* region, thus producing an ordered flow of charge carriers. Electric terminals made of conducting material can then be applied to both sides of the junction to extract direct electrical current. A potential difference between such terminals is necessary for the collection of the photocurrent.

The fraction of incident light effectively useful to generate EHPs depends on the band gap ($E_g$) of the semiconductor, which is defined as the energy gap between the valence and conduction bands of the material and is typically expressed in electron volts (eV)[5]. Photons with energy equal to or higher than the band gap will be able to generate

EHPs, while photons with energy below the band gap will not be absorbed by the material. For silicon, $E_g$ = 1.12 eV, which corresponds to a wavelength of about 1100 nm. Fig. A.3 shows the spectral response (or responsivity) of a silicon PV cell, defined as the ratio of the current generated by the illuminated cell to the incident solar power as a function of the light source wavelength[6]. Examining the curve from right to left, the cell starts to produce current roughly at the band gap wavelength, then the responsivity reaches a maximum between 950 nm and 850 nm. Proceeding towards higher energy photons, the responsivity decreases due to thermalization effects: the excess energy provided by short wavelengths photons is not used by the cell, but instead dissipated as heat.

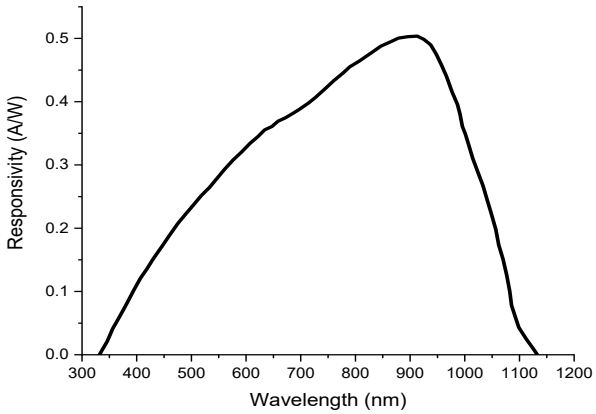


***Figure A.3*** *Spectral response curve for a monocrystalline silicon PV cell (adapted from ref. 6).*

A photovoltaic cell is described by its current-voltage (I-V) characteristic curve, which is a plot of its working points. A working point is defined as a combination of photocurrent and photovoltage values at which the cell can be operated[5]. The typical shape for the I-V curve of an illuminated PV cell is shown in Fig. A.4.a, along with the derived power-voltage (P-V) characteristic curve, where the electrical power is obtained as the product between voltage and current.

$$P = V \cdot I \tag{A.1}$$

Particular working points of the I-V curve are conventionally identified as the electrical parameters of the PV cell and are provided in all standard characterizations. By defining a load resistance as for Ohm's law (Eq. A.2), we identify the short-circuit current ($I_{SC}$) and the open-circuit voltage ($V_{OC}$) as the working points where $R_L$ is equal to zero or is infinitely high, respectively[5]. These parameters correspond, in the I-V

curve, to the current generated when no voltage is applied and to the voltage at which no current is detected. Both operation conditions yield zero electrical power.

$$R_L = \frac{V}{I} \tag{A.2}$$

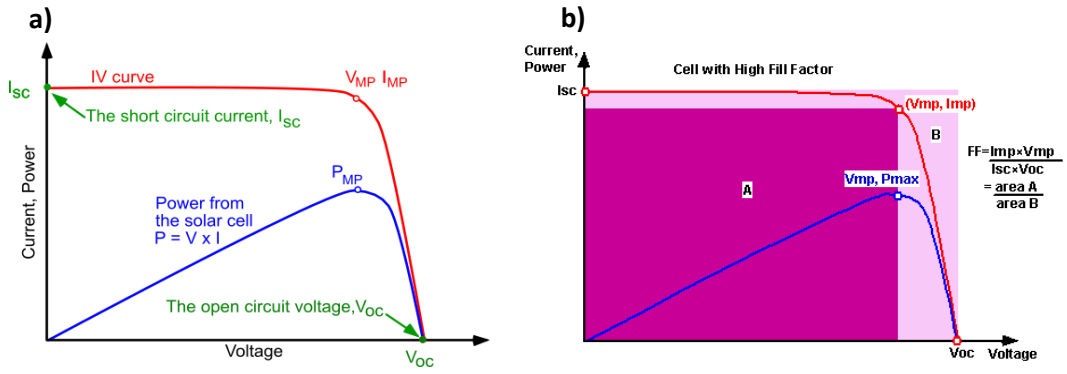


***Figure A.3*** *a) I-V (red line) and P-V (blue line) characteristics for a generic photovoltaic cell under illumination with marked electrical parameters, and b) graphical representation of the fill factor for the same I-V characteristic (adapted from ref. 2).*

The power reaches a peak ($P_{MP}$) at a specific working point named the maximum power point (mpp). The combination of current and voltage values at maximum power ($I_{MP}$ and $V_{MP}$) can be related to the product of $I_{SC}$ and $V_{OC}$ by defining a further parameter called the fill factor (FF), which accounts for the "squareness" of the I-V curve (Fig. A.3.b)[4]. High FF values denote overall good performance of the PV cell; factors that influence the fill factor by lowering its value can be large charge recombination effects or the presence of parasitic resistances in the circuit, which cause dissipation of the generated photocurrent.

$$FF = \frac{I_{MP} \cdot V_{MP}}{I_{SC} \cdot V_{OC}} = \frac{P_{MP}}{I_{SC} \cdot V_{OC}} \tag{A.3}$$

A final relevant electrical parameter provided for PV cells is the overall power conversion efficiency (PCE), defined as the ratio of the peak power extracted from the cell to the incident light power ($P_{in}$)[3]. In other words, the PCE accounts for the fraction of incident power effectively converted into electricity by the cell.

$$PCE = \frac{P_{MP}}{P_{in}} \tag{A.4}$$

By normalizing the output power for the area of the PV cell ($P_{in}$ is typically expressed as an irradiance, in $W/m^2$) and substituting Eq. A.3 in Eq. A4, we obtain the experimental expression for the PCE reported in Eq. 1.5 of Chapter 1.

$$PCE = \frac{J_{LSC} \cdot V_{OC} \cdot FF}{P_{in}} \quad \text{(A.5)}$$

# References


1. Reinders, A., Verliden, P., van Sark, W. & Freundlich, A. *Photovoltaic Solar Energy: From Fundamentals to Applications*. (John Wiley & Sons, Ltd, 2017).
2. https://www.pveducation.org (last accessed: August 2022).
3. Schembri, M. An Introduction To Solar Simulator Devices. *McMaster J. Eng. Phys.* **2**, 1−4 (2017).
4. Altermatt, P. P. *Silicon solar cells*. *Optoelectronic Devices: Advanced Simulation and Analysis* (The Royal Society of Chemistry, 2005). doi:10.1007/0-387-27256-9_11.
5. Dittrich, T. Basic Characteristics and Characterization of Solar Cells. in *Materials Concepts for Solar Cells* 3–43 (2018).
6. Hariharan, P. Detectors. in *Basics of Interferometry* 57–65 (Academic Press, 1992).

# Appendix B

- ## Additional figures: I-V characteristics

The I-V characteristic curves relative to all P-V curves presented in Chapter 4 are given below.

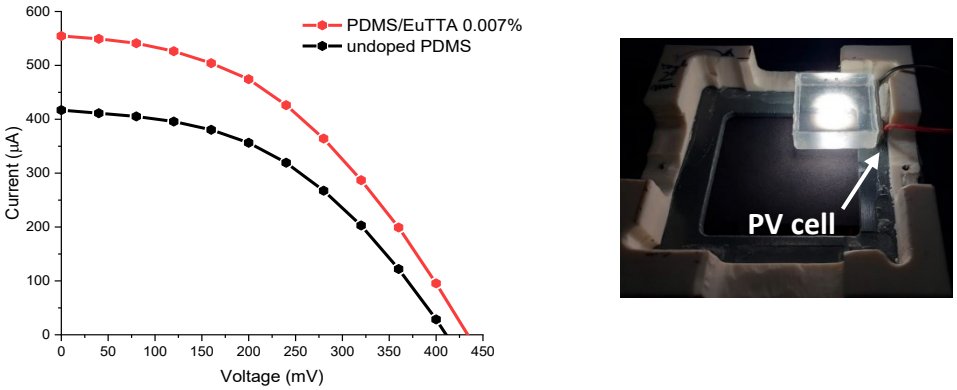


***Figure B.1*** *Collected I-V characteristics associated to the P-V curves of Fig. 4.4. Samples: a 2.5 × 2.5 × 0.8 cm³ PDMS tile containing [Eu(tta)₃phen] at the 0.007% by weight and an analogous blank tile.*

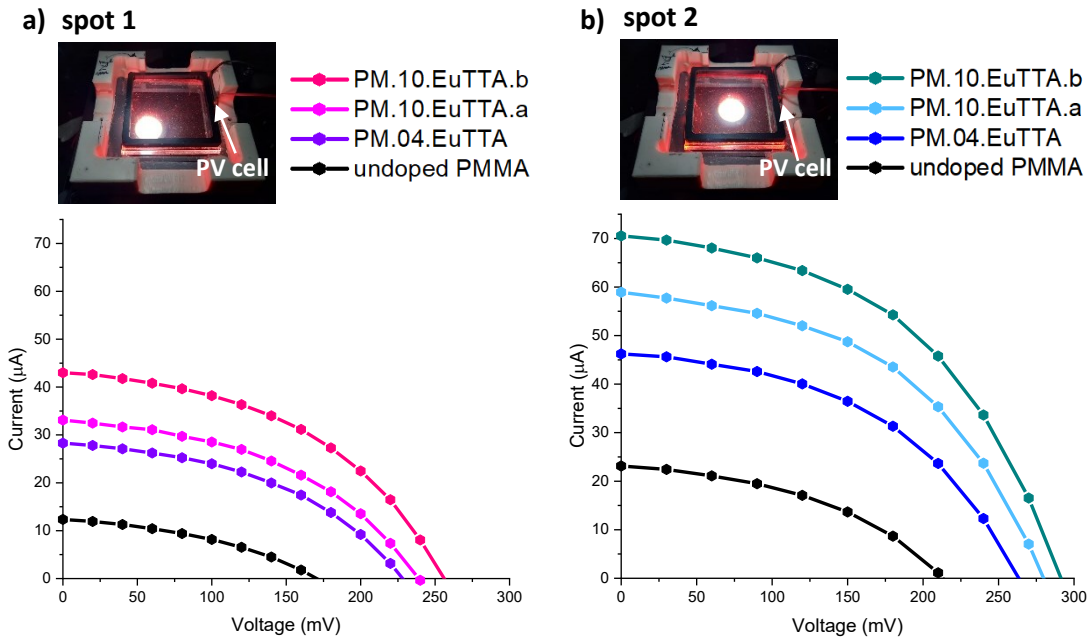


***Figure B.2*** *Collected I-V characteristics associated to the P-V curves of Fig. 4.6. Samples: a series of supported 5.0 × 5.0 cm² PMMA films containing [Eu(tta)₃phen] at different concentrations (see Table 4.1).*

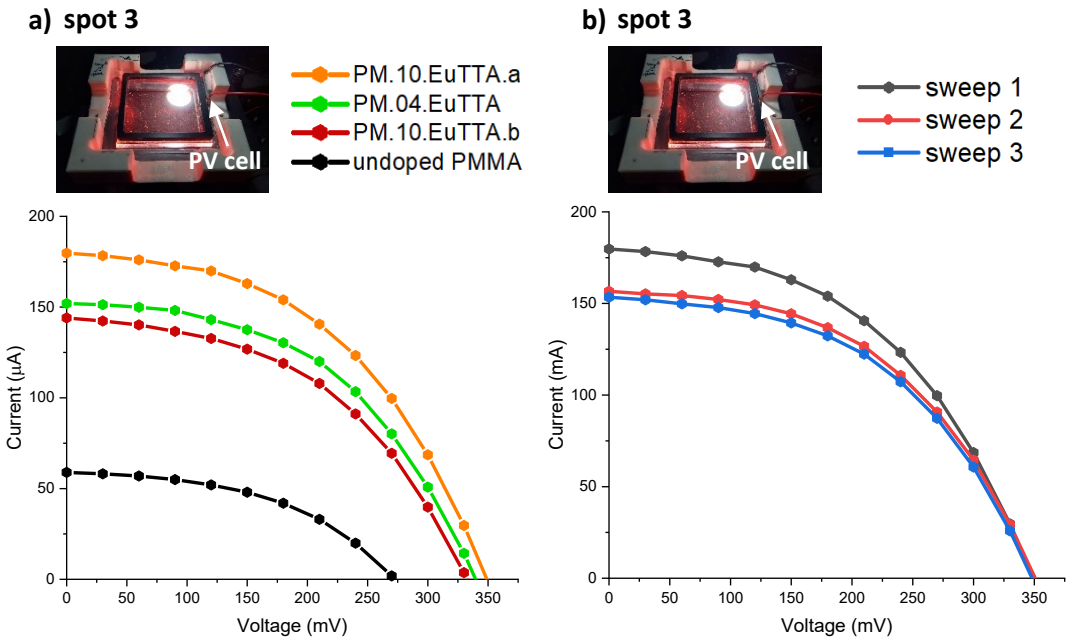


***Figure B.3*** *Collected I-V characteristics associated to the P-V curves of Fig. 4.7. Samples: a series of supported 5.0 × 5.0 cm² PMMA films containing [Eu(tta)₃phen] at different concentrations (see Table 4.1).*

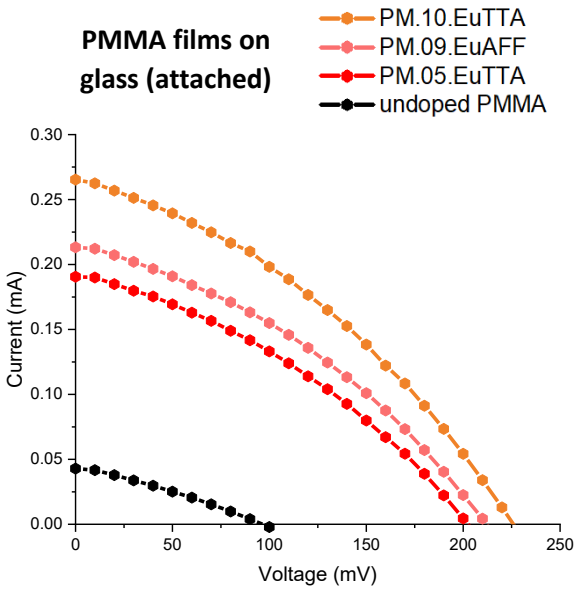


***Figure B.4*** *Collected I-V characteristics associated to the P-V curves of Fig. 4.9. Samples: a series of supported 5.0 × 5.0 cm² PMMA films containing [Eu(tta)₃phen] at different concentrations and a supported 5.0 × 5.0 cm² PMMA film containing [Eu₂(AFF)₄](NEt₄)₂ at the 0.9% by weight (see Table 3.4).*

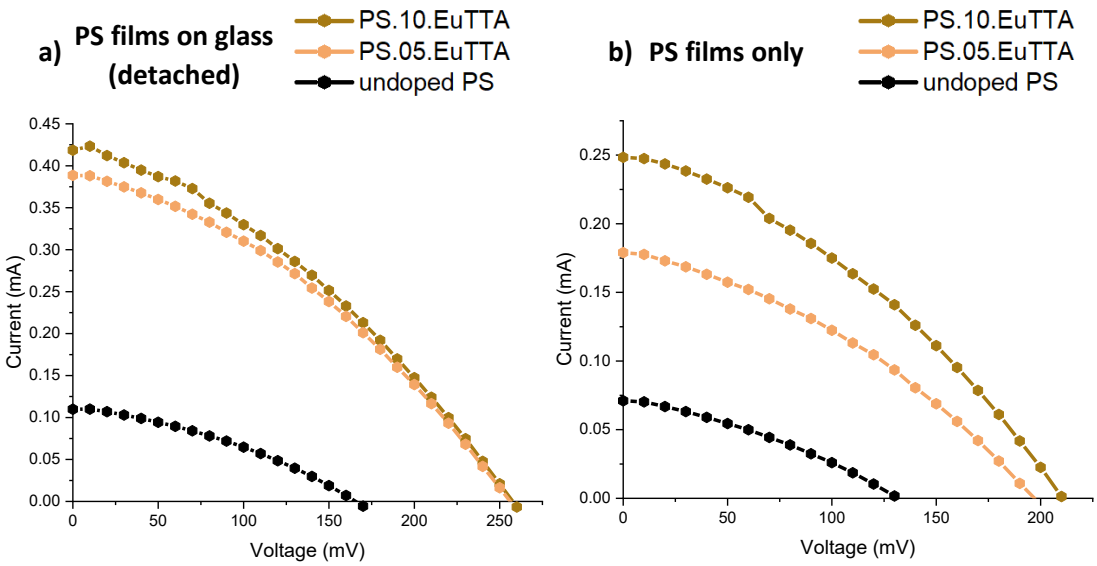


***Figure B.5*** *Collected I-V characteristics associated to the P-V curves of Fig. 4.10. Samples: a series of 5.0 × 5.0 cm² PS films containing [Eu(tta)₃phen] at different concentrations (see Table 3.4), a) propped on a supporting glass slate and b) without the slate.*

# Ringraziamenti

Raggiungere la fine di questo percorso universitario non mi sarebbe stato possibile senza le meravigliose persone che mi sono state vicino e che mi hanno aiutata in ogni momento di questi intensissimi ultimi due anni.

Doverosi ringraziamenti vanno al gruppo di ricerca che mi ha accompagnata durante il lavoro di tesi. Ringrazio la Professoressa Lidia Armelao, per avermi dato l'opportunità di lavorare in un ambito che mi appassiona e per la disponibilità mostratami durante questa esperienza. Ringrazio il Dott. Marzio Rancan e il Dott. Gregorio Bottaro, per avermi seguito con infinita pazienza e disponibilità e per le preziose spiegazioni. Ringrazio inoltre la Professoressa Carla Marega per l'aiuto con le analisi termiche e la Dott. Roberta Seraglia per le analisi di massa.

Ringrazio Maria Rando, somma intenditrice di tubini luminescenti e ormai mia "NMRista" di fiducia, per l'immenso aiuto con gli esperimenti e per aver condiviso con me momenti di comicità epica sia dentro che fuori il laboratorio. Ringrazio Mario Monaco, compagno di corso fin dagli albori della laurea triennale e divenuto compagno di tesi magistrale, per le conversazioni più o meno serie (queste ultime spesso condite da svariate "JoJo pose"), ma mai scontate.

Un enorme ringraziamento va poi alla mia famiglia, in primis ai miei genitori per avermi sempre sostenuta e spronata ad inseguire le mie ambizioni e per avermi permesso di farlo; sapervi fieri di me è la gratificazione più grande che possa ricevere. Grazie a mia sorella Isabella per saper sempre alleggerire anche i momenti più stressanti, e che aspetta un ringraziamento ufficiale ormai da due anni.

Ringrazio i miei coinquilini Chiara e Francesco per una delle convivenze più divertenti e imprevedibili mai affrontate e per la carica di autostima che sanno trasmettermi.

Un ringraziamento speciale va a Michela, Rebecca, Mara, Petra, Milena e alle mie adorate Mujeres Divinas, amiche insostituibili senza le quali non sarei qui a scrivere questi ringraziamenti. Ringrazio anche gli amici chimici conosciuti a Padova, che hanno reso più facili e molto felici questi anni di università (lo stimato collega Luca Morgan potrebbe addirittura dire gli "anni" della tesi!).

Infine ringrazio Giorgio, per essermi stato vicino durante gli inevitabili momenti di sconforto e per aver gioito con me di ogni piccolo e grande traguardo raggiunto. Se sono arrivata ai miei obiettivi è soprattutto merito tuo, grazie.